UNIVERSIDAD DE CHILE
FACULTAD DE CIENCIAS FÍSICAS Y MATEMÁTICAS
DEPARTAMENTO DE INGENIERÍA MECÁNICA

EXERGO-PARAMETRIC ANALYSIS AND OFF-DESIGN YEARLY MODELLING OF A SOLAR DRIVEN RCBC WITH S-CO_2 AS WORKING FLUID

MEMORIA PARA OPTAR AL TÍTULO DE INGENIERO CIVIL MECÁNICO

CARLOS FEDERICO KLEIN BÓRQUEZ

PROFESOR GUÍA:
JOSÉ MIGUEL CARDEMIL IGLESIAS

MIEMBROS DE LA COMISIÓN:
ÁLVARO ALEJANDRO VALENCIA MUSALEM
RODRIGO SEBASTIÁN BARRAZA VICENCIO

SANTIAGO DE CHILE
2020

RESUMEN DE LA MEMORIA PARA OPTAR
AL TÍTULO DE INGENIERO CIVIL MECÁNICO
POR: CARLOS FEDERICO KLEIN BÓRQUEZ
FECHA: 2/1/2020
PROF. GUÍA: JOSÉ MIGUEL CARDEMIL IGLESIAS

EXERGO-PARAMETRIC ANALYSIS AND OFF-DESIGN YEARLY MODELLING OF A SOLAR DRIVEN RCBC WITH S-CO_2 AS WORKING FLUID

Given the increasing demand for energy and the challenges posed by climate change, the need for a clean, renewable and dispatchable source of energy is greater than ever. Chile has an outstanding solar potential and conditions in the northern region are apt for Concentrated Solar Power, among other solar technologies. Renewable sources of energy such as Solar and Wind have grown considerably worldwide and particularly in Chile. The effects of a high degree of penetration of such technologies on the energy matrix make the turn down capabilities of a power central one of its most important assets moving forward, in order to cancel out the consequence of the high variability that the aforementioned sources present.

The present work proposes a yearly based, off-design model that describes the operation of two solar-driven Recompressed Closed Brayton cycles with supercritical carbon dioxide as working fluid. Solar irradiation and meteorological conditions from northern Chile are considered along with dispatch curves to assess the seasonal performance of the aforementioned solar driven cycles. The modelling approach for the power cycle and the yearly simulation are carried out using the Engineering Equation Solver software which considers the cycle's heat input from the modelling of the solar field through the System Advisor Model software. The power cycle under design conditions delivers a net power output of 25 [MW] with a first law efficiency of 48.3%.

The exergetic analysis finds the high temperature recuperator to be the component responsible for the greatest amount of exergy destruction under design point operation. The yearly simulation shows how this shifts to the Cooler under high ambient temperature and the turbine. The explanation behind this lies in how an increase in ambient temperature shifts the T-s diagram of the cycle resulting in greater temperature at the Cooler's inlet, the increase in exergy destruction in the turbine corresponds to a decrease in isoentropic efficiency due to off-design operational conditions.

The limited operational range for the cycle proposed in literature is determined and contrasted with the extended operational range for a new proposed configuration. Comparisons in cycle efficiency quantify the higher flexibility achieved by the proposed cycle and the synergistic turn-down strategy of throttling mass flow and high pressure. The seasonal efficiency for the literature cycle is 29% and for the proposed cycle it is 39%. The plant factor for the literature cycle assuming sufficient heat storage is 76.45% whilst for the proposed cycle it is 93.45%.

RESUMEN DE LA MEMORIA PARA OPTAR
AL TÍTULO DE INGENIERO CIVIL MECÁNICO
POR: CARLOS FEDERICO KLEIN BÓRQUEZ
FECHA: 2/1/2020
PROF. GUÍA: JOSÉ MIGUEL CARDEMIL IGLESIAS

ANÁLISIS EXERGO-PARAMÉTRICO Y MODELAMIENTO ANUAL EN CONDICIONES FUERA DE DISEÑO DE UN RCBC IMPULSADO POR ENERGÍA SOLAR CON S-CO_2 COMO FLUIDO DE TRABAJO

Dada la creciente demanda energética y los desafios presentados por el cambio climático, la necesidad de una fuente limpia, renovable y despachable de energía es mayor que nunca. Chile tiene un potencial solar excepcional y las condiciones en la región norte son aptas para la energía termosolar de concentración, entre otras tecnologías solares. Fuentes renovables de energía como la solar y la eólica han crecido considerablemente alrededor del mundo y particularmente en Chile. Los efectos de una alta penetración de dichas tecnologías en la matriz energética hacen de la capacidad de modulación de despacho de una central de potencia una de sus más importante cualidades en el futuro, en pos de compensar las consecuencias de la alta variablididad que presentan las tecnologias antes mencionadas.

El presente trabajo propone un modelo anual que contempla operación en condiciones fuera de diseño y describe la operación de dos ciclos Brayton cerrados de recompresión alimentados por energía solar con dióxido de carbono supercrítico como fluido de trabajo. Se considera la irradiación solar y las condiciones meteorológicas del norte de Chile junto a curvas de despacho para evaluar el rendimiento estacional de los ciclos previamente mencionados. El modelamiento del ciclo de potencia y la simulación anual se llevan a cabo utilizando el software Engineering Equation Solver que considera la entrada de calor al ciclo a partir del modelamiento del campo solar a través del software System Advisor Model. El ciclo de potencia en condiciones de diseño entrega una potencia neta de 25 [MW] con una eficiencia de primera ley del 48.3 %.

El análisis exergético identifica al recuperador de alta temperatura como el equipo responsable de la mayor cantidad de destrucción de exergía bajo condiciones de diseño. El modelamiento anual muestra como esto cambia al enfriador bajo condiciones de alta temperatura ambiente y la turbina. La explicacion se debe a como cambia el diagrama T-s del ciclo resultando en una mayor temperatura a la entrada del enfriador, el aumento en destrucción de exergía en la turbina se debe a una menor eficiencia isoentrópica debido a operación en condiciones fuera de diseño.

El acotado rango operacional del ciclo presentado en la literatura es determinado y contrastado con el rango operacional extendido de una nueva configuración propuesta. La comparación de eficiencias entre los ciclos cuantifica la mayor flexibilidad lograda por la configuración propuesta y la sinergia entre la reducción de flujo másico y alta presión del ciclo como estrategia de modulación. La eficiencia estacional para el ciclo de la literatura es 29% y para el ciclo propuesto es de 39%. El factor de planta para el ciclo de la literatura, asumiendo suficiente almacenamiento térmico es 76.45%, mientras que para el ciclo propuesto es de 93.45%.

Dedication

Quiero agradecer a todos quienes me han apoyado y han compartido conmigo estos años. En primer lugar quiero agradecerle a mi profesor guía, el Dr. José Miguel Cardemil Iglesias su apoyo, paciencia e ideas para lograr el presente trabajo.

A mi familia por las oportunidades que me dieron y su cariño incondicional. A mi padre Gastón, quien me llevó a incontables visitas de obra de pequeño y siempre fomentó mi interés tanto en las ciencias como en la música. A mi madre Carolina por su sacrificio y su forma única de querer a sus hijos, si bien sigo dudando de tu cocina nunca dudé de tu cariño. A mi hermana Isabel por el apoyo, compañía y peleas. A mis abuelos, nunca pude hacérselos saber pero siempre estaré agradecido por la familia que formaron y su esfuerzo ha y seguirá impulsándome para dar gracias de la única forma que conozco.

A mis mejores amigos, Thomas, Adolfo y Carlos. Dicen que los amigos son la familia que elegimos, no podría pedir una mejor.

A mis amigos de plan común y de mecánica, gracias por hacer de la U mucho más que un lugar de estudio. A los chicos de Diablos de Ingeniería por las enseñanzas tanto dentro como fuera de la cancha, por los buenos y los malos ratos que pasamos juntos. Al equipo de difusión por permitirme compartir mi pasión por la ingeniería con las nuevas generaciones.

Quiero agradecer a quienes me acompañaron esas largas noches mientras todos dormían y nunca supieron que estaba haciendo, muchas gracias Otto y Siegfried.

Por último, quiero agradecer desde el fondo de mi corazón a Mariana. Las palabras no bastan para agradecer todo lo que has hecho, espero que mis acciones si.

Good things come to those who wait, thanks for your wait.

Table of Contents

List of Tables

List of Figures

Chapter 1

Introduction

1.1 Context

Considering the growing awareness of climate change, the need for sustainable and non-fossil-fuelled sources of energy is more important than ever before. Particularly in Chile, the energy matrix is heavily based on fossil fuels as seen in Fig. 1.1. Fossil fuels account for approximately 59.4 % of the total 24 [GW] of installed capacity whilst non-conventional renewables contribute less than a quarter of the total.

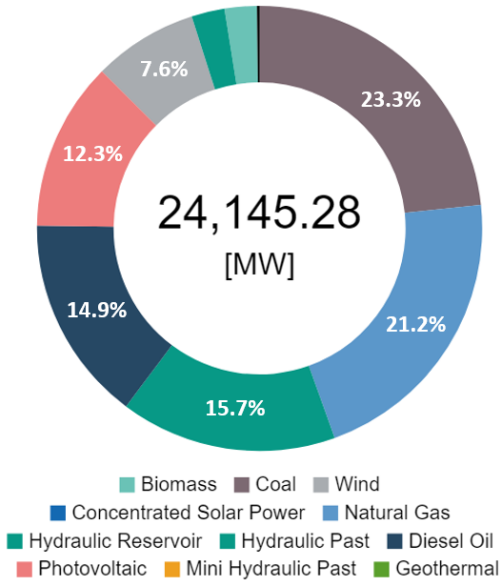

Figure 1.1: Current Chilean energy matrix composition [1]

Technologies such as solar photo-voltaic (henceforth PV) and wind turbines provide clean sustainable energy, yet due to the high degree of variability they are unable to deliver the required energy outputs throughout the day consistently.

Such challenges can be surmounted if energy storage is incorporated. To date the best candidate is lithium batteries technology, whose high price renders it an economically unfeasible pathway in many scenarios. Current demand for lithium metal sets a price per metric

tonne of lithium carbonate close to 10000 [USD] [2] (16500 [USD] for metallic lithium [3]). As a comparison, the price for a metric tonne of copper metal is close to 5777 [USD] [4].

In addition to that, there is high uncertainty regarding how the price of lithium salts will vary in the short and mid term, some speculate the advent of electric cars will only worsen the price problem.

High degrees of Wind and PV penetration on an energy grid such as those observed in California bring about new challenges in the electric utilities sector. California possesses an hourly electric load that resembles the silhouette of a duck when PV and Wind energy production are subtracted from the total load, as observed in Fig. 1.2. This uncommon shape can be explained due to the fact that PV technology can only generate power during daytime, thus the amount of power required from sources other than PV decreases rapidly with sunrises, and it increases at a higher pace when the sun sets in places with high PV penetration. As with many energy markets, California's demand peaks occur after sunset. The result is the need for a source of dispatchable energy to help even the fluctuations inherent with variable energy sources such as Wind and PV during the day, a source that can ramp-up and ramp-down power output quickly at sunrise-sunset and a source that can produce during after-sun hours. Natural gas power plants and hydroelectric power plants are a good match for these criteria, yet the availability of hydric resources is limited and natural gas power plants defeat the purpose of transitioning away from fossil-fuelled energy sources.

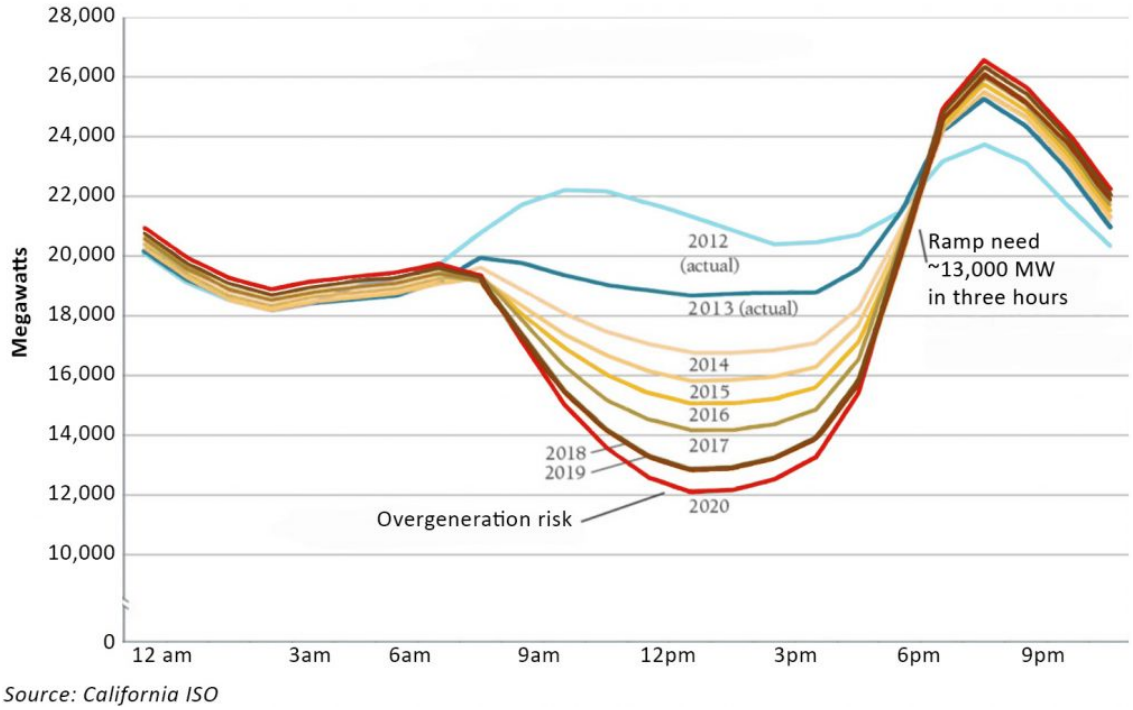

Figure 1.2: California net load curve, March 31 [5]

A large presence of PV energy on an energy grid can lead to an installed generation capacity higher than demand (typically around noon) and in order to safeguard the integrity of the grid said excess energy must be curtailed. Thereupon as variable sources of energy expand to a larger share of the energy matrix, the other components are subjected to more demanding dispatch conditions (larger and faster power output increases-decreases). The

hidden effect of an increase in variable sources of energy is a true incompatibility with power sources unable to cope with the challenges associated with coexisting with variability.

Concentrated Solar Power (henceforth CSP) systems generate power through the concentration of solar radiation to provide heat to a power cycle (a steam powered Rankine cycle for example). Fig. 1.3 presents a CSP power plant diagram. On the left side is the solar field, composed by heliostats that focus solar irradiation into the receiver atop the power tower. The thermal storage system with its hot and cold salt tanks occupies the bottom section of the diagram. This system stockpiles the energy collected by the solar field by using the concentrated solar irradiation to heat salts from the cold salt tank and storing them in the hot salt tank. These hot salts then supply the power block with heat when it needs it through the primary heat exchanger. The power block on the right side of the diagram showcases standard components, a turbine, a cooling system, a pump/compressor and a generator. This simplified power block representation applies if the power block's cycle is a Rankine cycle or a Brayton cycle.

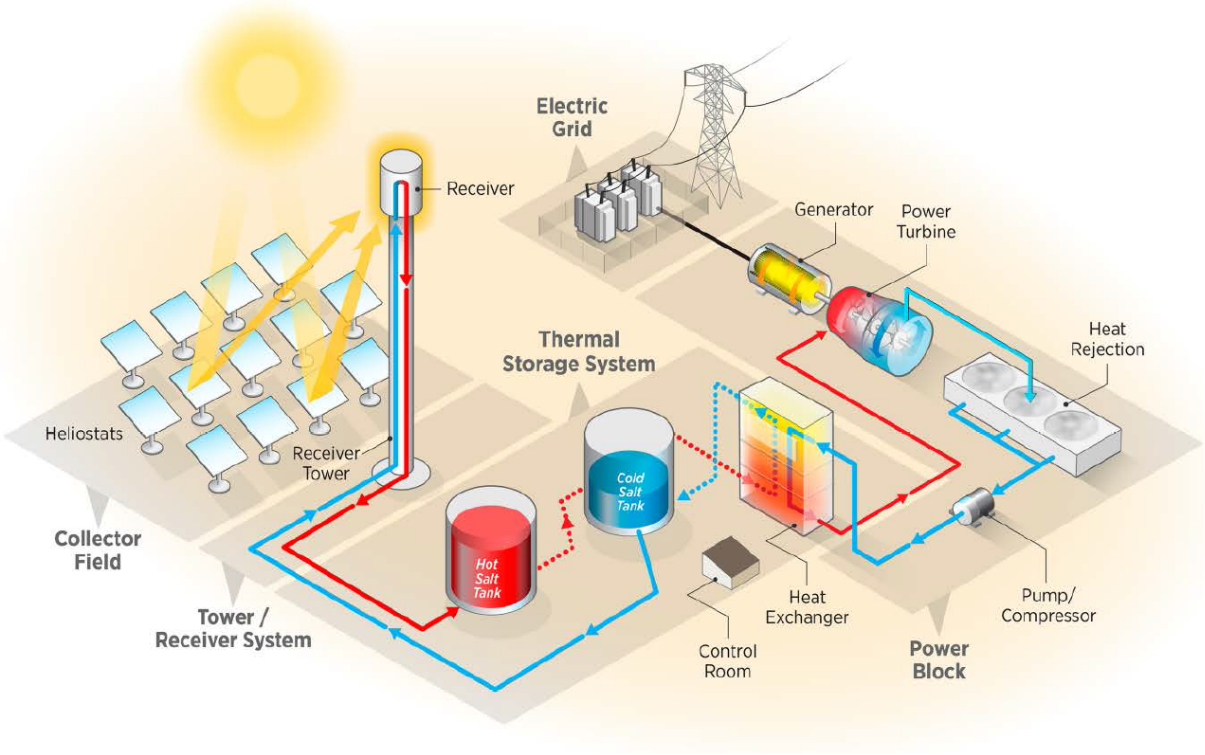

Figure 1.3: Illustrative CSP plant diagram with hot and cold salt tanks [6]

When comparing CSP and PV technology an important difference is that PV can operate during cloudy days whilst CSP can't due to the impossibility of concentrating diffuse radiation. In addition to this shortcoming of CSP, PV has a lower CAPEX than CSP, on a per unit energy dispatched basis. Utility scale PV plants averaged a CAPEX close to 1693 US dollars per kilowatt [7] between the years 2010 and 2018 whilst for CSP plants this indicator averaged 5204 US dollars per kilowatt [8].

The advantage that CSP has over PV lies on the easiness to couple thermal storage. Whilst PV requires batteries to store excess energy, CSP can use a thermal storage media to

stock-up excess thermal energy. The cost for thermal storage on a CSP cycle is considerable and it is an important contribution to the project's CAPEX, yet it is significantly lower than the equivalent cost for the batteries required by a PV plant. Thereupon, despite the aforementioned investment costs associated with the Thermal Energy Storage (henceforth TES), CSP coupled with TES results in a technology that provides clean, renewable and dispatchable energy 24/7.

These CSP-TES power plants have long been in operation in countries like Spain (Andalucía) and the USA (south-west) [9]. Fig. 1.4 shows how Spain and the USA eclipsed the rest of the world regarding CSP installed capacity. Recently China has invested heavily into CSP-TES power plants in its effort to reduce greenhouse gas emissions [10]. On the other hand, countries where the solar resource is higher like Namibia, Mexico, and South Africa have yet to see the same level of irruption from CSP-TES power plants into their energy matrices. The comparatively high investment costs of CSP-TES power plants have played an important role regarding this issue.

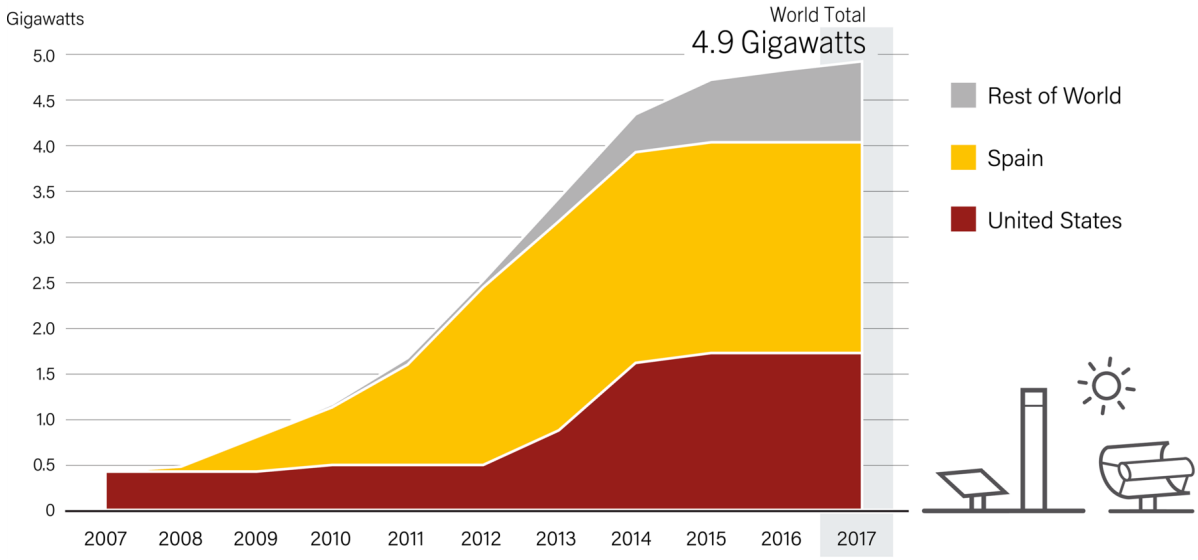

Figure 1.4: Growth of concentrating solar thermal power global capacity, by country and region, 2007-2017 [9]

Sunshot [6] is an initiative from the US Department of Energy whose main objective is to mature solar technologies (PV & CSP-TES) enough to allow them to compete on a cost-to-cost basis with traditional energy sources on the different segments of the utilities market by 2020. On the CSP-TES front, Recompressed Closed Brayton Cycles (henceforth RCBC) with supercritical carbon dioxide (henceforth s-CO_2) as the working fluid appears to be the path to follow. Angelino [11] demonstrated on 1968 that a s-CO_2 RCBC can achieve thermal conversion efficiencies in excess of 50% when operating under medium to high temperatures (650 [°C]). The potential of the s-CO_2 RCBC has sparked the interest of many and is currently being studied for deployment in areas as varied as nuclear energy and marine propulsion.

Given the high degree of variability on the solar resource, it is not only important that the RCBC achieve a high cycle efficiency when operating under design conditions, but that it can maintain high thermal conversion efficiencies during off-design conditions. For a power block

this translates to operating under a wide range of ambient temperatures and outputting the amount of net power requested by the grid operator. Going back to the CAISO duck curve, it seems clear that in the near future the power output range and the time needed to modulate power output is perhaps the most pressing quality a RCBC must have in order to coexist and synergize with the ever-growing presence of PV plants and Wind farms.

Another factor to consider when assessing the implementation of CSP-TES is the availability of water. Most power cycles are water cooled, the alternative to water cooling is to use ambient temperature air in places with high water scarcity. Using water allows the cycle low temperature to be much lower than if air is used to do the cooling (dry-bulb temperature is the limit for air cooling whilst wet-bulb temperature is the limit using water). This translates to a greater theoretical cycle efficiency (Carnot's theorem). Unfortunately, places with high potential for CSP are typically arid and the additional costs required to supply the power plant with fresh water can easily outweigh the benefits of water cooling. Therefore, the design and analysis of how an air-cooled RCBC performs under variable demand and environmental conditions is of high interest, in transitioning away from fossil-fuelled energy.

1.2 Motivation

Chile has a wide range of climatic conditions given its peculiar size and shape. Northern Chile houses the Atacama desert, the driest in the world. The lack of moisture in the region results in the clearest skies, or analogously, those with the least cloud coverage. This in turn explains why this geographic region possesses the highest levels of normal irradiation worldwide. As seen in Fig. 1.5, northern Chile has the highest DNI yearly sum, towering over places like the Kalahari, Tibet and the Australian outback. Whilst the strength of the Sun in Atacama is outstanding, it is not without peers. The Sahara and Saudi Arabia know days as sunny as Atacama does. The difference that crowns Atacama as number one when it comes to DNI is the nearly nonexistent cloud cover. The presence of many astronomical observatories in Atacama bear witness to how unlikely it is to get a cloudy night, or day.

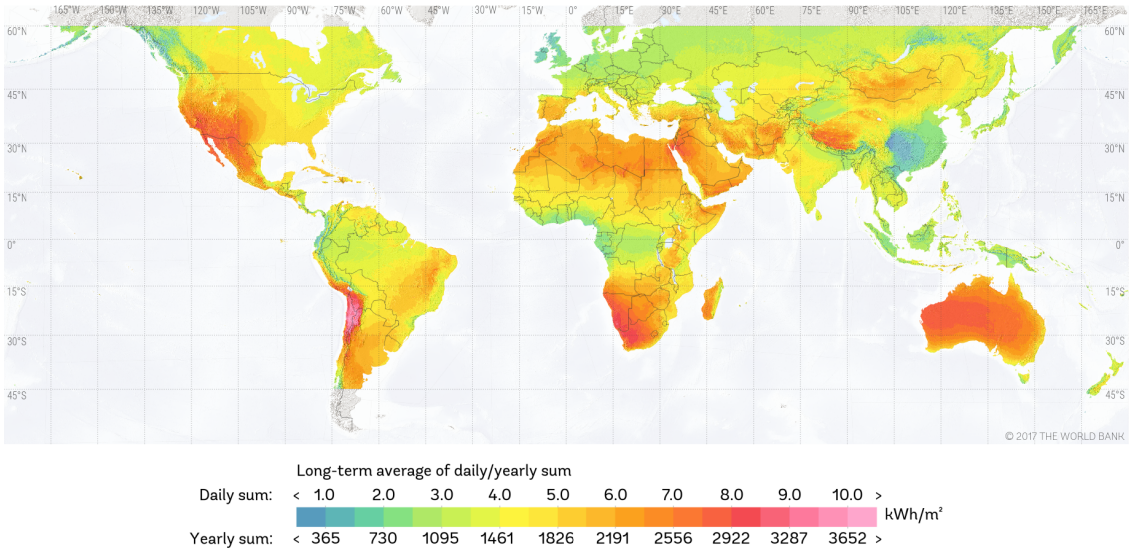

Figure 1.5: Direct normal irradiation world map [12]

Despite the previous points, to date there are no operational CSP plants in Chile. High investment costs, the lack of experience regarding CSP in Chile and current CSP cycles conversion efficiencies configure a scenario where CSP plants are not an alluring option for investors and the utility sector when compared to conventional power plants. Investment costs are expected to fall as the technology matures and plenty of work is being carried out in hopes of raising the CSP conversion efficiencies. A RCBC that uses supercritical carbon dioxide as working fluid can achieve those high efficiencies required to compensate the investment costs needed to phase out conventional fossil-fuel sources of energy. Cerro Dominador will be the first CSP plant to come online in Chile. Unlike the aforementioned cycles that use supercritical carbon dioxide, Cerro Dominador will use water as its working fluid. Therefore Cerro Dominador will suffer the same shortcomings that have stifled the growth of CSP-TES power plants in countries with solar potential like Namibia. In order to steer Chile away from its fossil fuel dependence it is imperative to model and assess the off-design performance of CSP-TES power plants running advanced cycles using radiation levels, meteorological data and dispatch curves from Chile.

1.3 s-CO_2 RCBC for CSP

The potential showed by s-CO_2 RCBC motivated large amounts of research set on making solar-driven s-CO_2 RCBC power plants a reality. Some work was aimed at theoretical optimisation of the cycle under stipulated constraints, other efforts deliberated on the challenges posed by the uncommon characteristics of this novel working fluid. To date research has matured and at large it has left the theoretical days in favour of experimental studies. The Sandia National Laboratories s-CO_2 test loop is one of the early experimental s-CO_2 power cycle test rigs [13]. Subsequently experimental data was available in the literature and soon thereafter empirical models ensued, convection heat transfer coefficients being among the most common.

Traditionally power plants where designed to operate only at the design power output and design conditions, with measures taken in order to mitigate any source of disturbances. The variable nature of the solar resource resulted in systems that could store thermal energy in an effort to decouple power plant power production from the aforementioned variability. Changes in the energy market have long transformed such paradigms and nowadays the capacity of a power plant to increase and decrease it's power output, as dictated by the grid controller have meant that operating with high conversion efficiencies under design conditions but low conversion efficiencies under off-design conditions is not sufficient. Operation in places like high-altitude deserts purport maintaining a low cycle low temperature consistently throughout the day is economically unfeasible. Whether to engineer systems that could isolate the power block from changes in ambient temperature or to design power blocks that could handle the effect a shifting cycle low temperature entails, advances where required by the aforementioned conditions.

Variable energy supply, shifting ambient conditions and demanding dispatch regimes construct a reality where the study of off-design operation is not only paramount, but an important component of the future of the energy market. Therefore work was put into describing and modelling the off-design operation of power cycles and in the interest of this work, the s-CO_2 RCBC. Models emerged, varied in their complexity and the assumptions upon which

they are based. To date (to the author's knowledge) there is gap for a holistic model that compiles the various more detailed methodologies present in the literature and revises those that rely on conditions unrepresentative to real world operation. Heat exchangers are modelled through methodologies that do not take pressure drop into account leading to alternate considerations like the 1% pressure drop model. The non-linear relationship between turbine conditions and mass flow is described as a fixed area nozzle. The probability that unknown phenomena is being overlooked by using simplified modelling methodologies is substantial and something that needs to be revised.

The present work builds upon the previous methodologies, beginning with a detailed physics based model for heat exchangers that accounts for pressure drop. A more complete surge routine describing and predicting operational ranges. The turbine is modelled through a hybrid of empirical data and a physical model. Solar irradiation, ambient temperature and grid demand determine the cycle's operation point and the power block model assesses the corresponding first law cycle efficiency allowing for a yearly simulation that considers meteorological conditions quantifying the yearly performance of an air cooled s-CO_2 RCBC.

1.4 Objectives

The main objective is to evaluate the performance of a s-CO_2 air-cooled RCBC operating under the meteorological conditions of northern Chile, assessing its seasonal cycle first and second law efficiencies under two turn-down strategies.

1.4.1 Specific objectives

- Model and compare SNL data for the experimental loop with cycle code results.
- Size and design a nominal cycle given yearly data from the Crucero substation.
- Propose an alternative cycle composition (N-M system) and turn-down strategy.
- Construct thermodynamic and engineering models to describe off-design operation for cycle components.
- Simulate on a quasi-stationary basis the yearly performance of both cycles.
- Quantify the performance of both cycles and the benefits of one over the other.

1.5 Scope

The scope for the present thesis work is as follows:

- The thermodynamic models for both cycles and the yearly quasi-static simulations are carried out in Engineering Equation Solver (EES).
- Calibration of the base model is carried out by comparison with data provided by the SNL test loop.
- Solar field modelling is carried out through Solar Advisor Model (SAM). The results are used as input for the yearly quasi-static simulation code.
- There is no direct accounting for heat losses on the cycle modelling.

- Pressure drop due to piping elements is not considered.
- Primary Heat Exchanger and Cooler are modelled through a simplified (pinch point) approach.
- Low temperature recuperator and high temperature recuperator are modelled through a discretized, physics based methodology.
- Turbomachinery is described by a mixture of dimensionless curves stemming from performance maps and physical engineering models.
- Cycle power output, mass flow rate and cycle high pressure are restricted to values equal to or lower than design.
- Recompression fraction is constant.
- No optimisation is considered for off-design operation.

Chapter 2

Background

2.1 s-CO_2

Besides the 3 common states of matter; solid, liquid and gas, there are other exceptional states of matter. A supercritical fluid is in one of those unusual states of matter. Carbon dioxide transitions into a supercritical fluid once its pressure and temperature exceed those of the critical point. The critical point of carbon dioxide is at a pressure of 73.9 [bar] and a temperature of 31.10 [°C]. This is graphically summarised in the Pressure-Temperature phase diagram in Fig. 2.1.

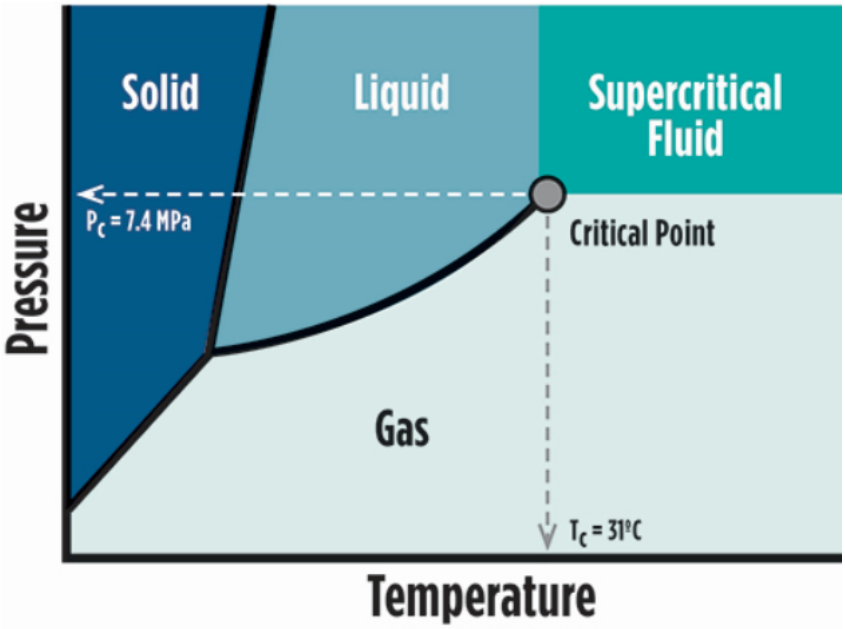

Figure 2.1: CO_2 P-T phase diagram [14]

That pressure is comparatively high (atmospheric pressure is approx. 1 [bar]) and the temperature is comparatively low (critical temperature for water is 374 [°C]). Once carbon dioxide approaches, and crosses the supercritical point, the physical frontier between the liquid and gas phase fades away. The fluid transitions into something that can be described as a gas with the density of a liquid, or a liquid that resembles and behaves like a gas.

Normally the transition from liquid to gas is accompanied by a phase change process where a certain amount of heat known as the latent heat must be supplied to (or expelled by) the fluid, with no change in temperature during said phase change process. Close to the critical point this phase change process varies significantly. Underneath the saturation bell, approaching the critical point (from below) the latent heat decreases until it becomes zero at the critical point. On the other hand, when above the saturation bell the phase change process is in no moment isothermal. There is no latent heat for phase change, only sensible heat. This means the latent heat translates into a significant spike in sensible heat close to the critical point.

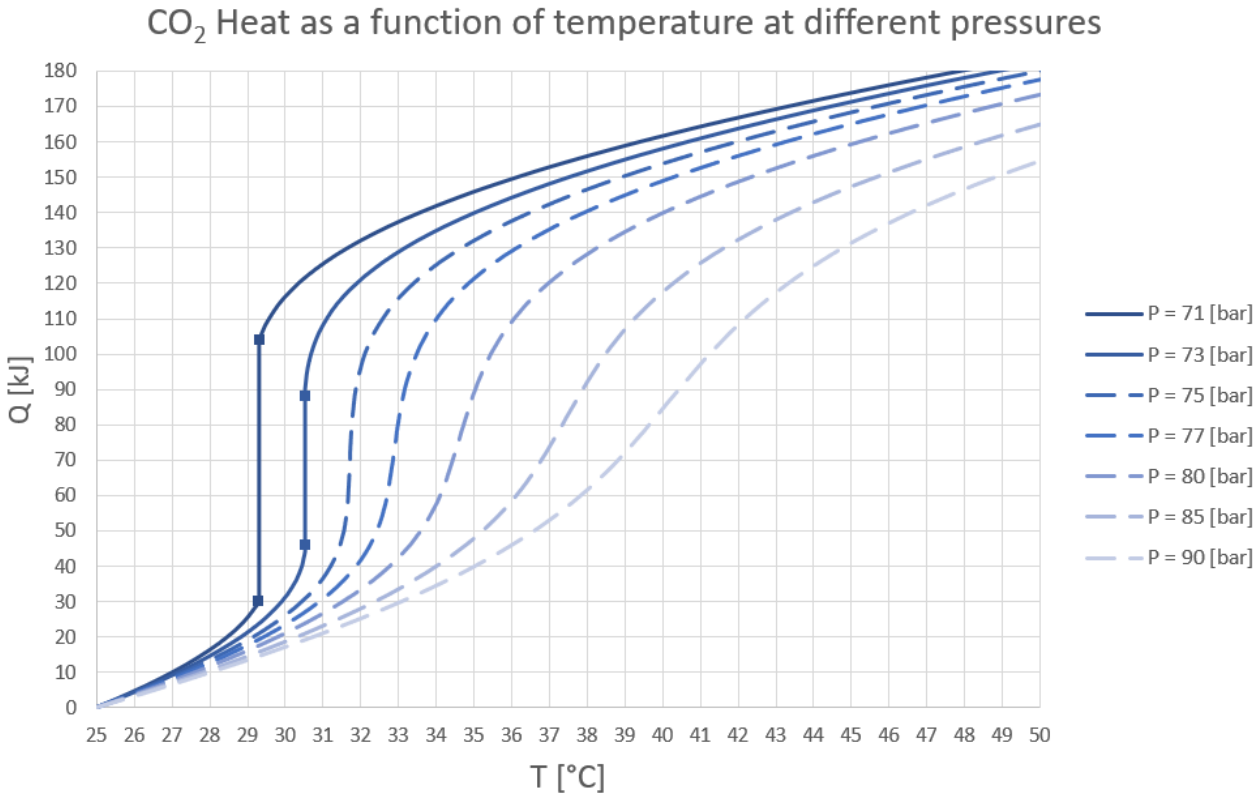

Figure 2.2: Heating curves for CO_2 near critical point

A graphic portrayal is presented in Fig. 2.2. A normal phase change process involves two slopes separated by a vertical cliff (first two curves, P = 71 [bar] & P = 73 [bar]) where the slopes represent sensible heat in liquid and gas phase, and the cliff the difference in energy between saturated liquid and saturated gas. The process for phase change in the case of a supercritical fluid looks like a slope that turns into a very steep slope and then returns to a more moderate slope (dotted curves). Near the critical point the slope of the curve approximates infinity, as in the limiting case the specific heat is the slope of a vertical line.

Figure 2.3 displays how the specific heat c_p peaks close to the supercritical point, it reaches a maximum value close to 390 [kJkg^{-1}K^{-1}] at a temperature of 31 [°C]. This phenomenon has important engineering design ramifications and it is the source of advantages as well as disadvantages.

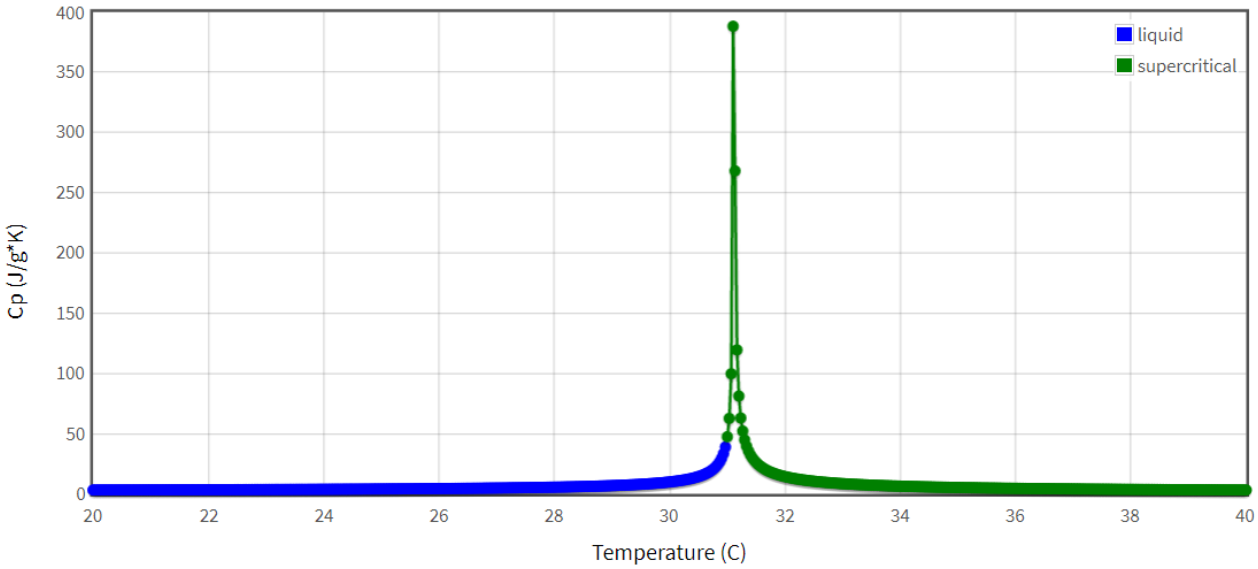

Figure 2.3: Specific heat of CO_2 as a function of temperature at 74 [bar] [15]

Other properties of s-CO_2 that set it apart from other working fluids are that it is thermally stable, non-flammable, non-toxic, inexpensive, less corrosive than water vapour and it has a comparatively high energy density (compared to steam).

2.2 RCBC

Fig. 2.4 presents a recuperated Brayton cycle (henceforth RBC) and a two-shaft RCBC. A RBC is a closed Brayton cycle with a recuperator that transports heat from the turbine outlet stream to the compressor's outlet stream with the aim of reducing the heat load of the primary heat exchanger (henceforth PHX), therefore increasing the cycle's first law efficiency. Like the Brayton cycle, the compressor and the turbine share a shaft in the RBC. The power required by the compressor is transmitted from the turbine directly. A RCBC is more complex and depending on the configuration it can have one, two or three shafts. The RCBC adds a separate compressor known as the recompressor to the RBC along with the separation of the recuperator into a high temperature recuperator (henceforth HTR) and a low temperature recuperator (henceforth LTR).

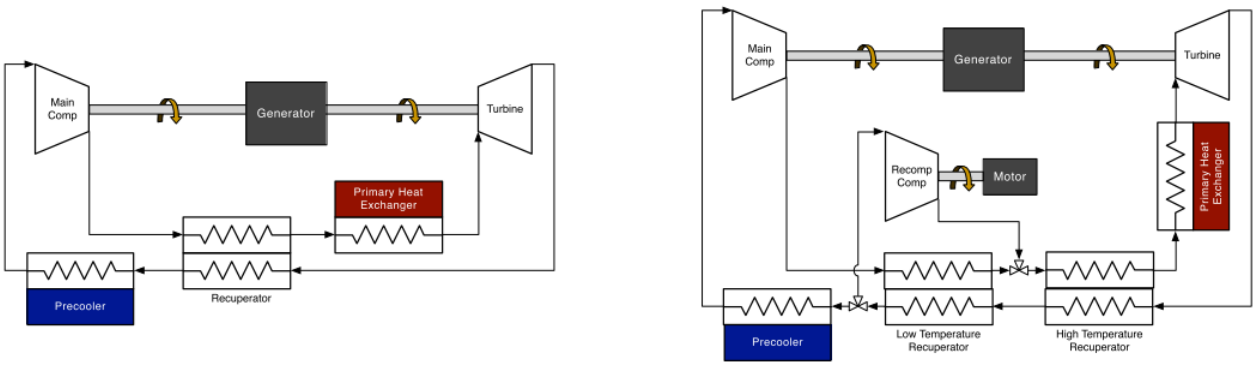

Figure 2.4: RBC (left) and two-shaft RCBC (right) diagrams [16]

Cycle efficiency in a RCBC as in any Brayton cycle is highly dependent on the BWR (back work ratio), an indicator of how much of the turbines power output is used to drive the working fluid's compression.

$$BWR = \frac{\dot{W}_{comp}}{\dot{W}_{turb}} \tag{2.1}$$

where $\dot{W}_{comp}$ is the compression power consumption and $\dot{W}_{turb}$ is the power generated by the turbine. The BWR in a conventional gas Brayton cycle ranges from 40 to 80%. A conventional steam Rankine cycle's BWR on the other hand is in the 1 to 2% range. Such a drastic difference is explained by recalling the formula for compression work:

$$W_{comp} = P\Delta V \tag{2.2}$$

where P is the pressure and ΔV the change in volume, water in a steam Rankine cycle enters the pump as an incompressible fluid, the change in volume is negligible when compared to the change of volume air undergoes in the compressor of a gas Brayton cycle, thus explaining the disparity between compression work. By virtue of the low temperature of the CO_2 critical point, given sufficient cycle cooling it is possible to compress the s-CO_2 in a RCBC at a state similar to that of a liquid (low specific volume and compressibility). The result is a smaller compression work which in turn implies a greater cycle first law efficiency. How close carbon dioxide is to its saturation bell at temperatures near 30 [°C] can be seen in Figure 2.5.

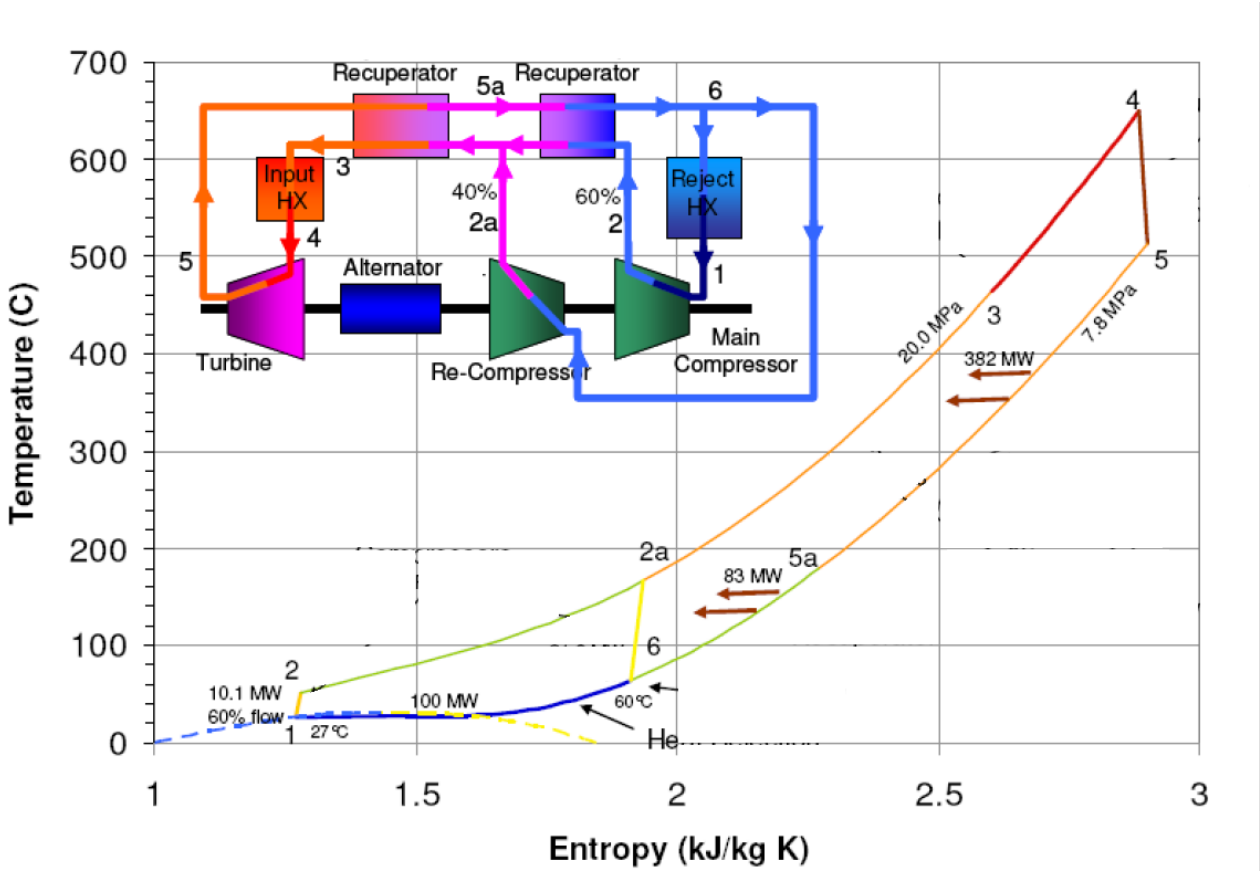

Figure 2.5: RCBC layout and T-s diagram [17]

In the RBC recuperator the low pressure s-CO_2 stream approaches the critical point and it's specific heat increases. This causes the low pressure stream's capacitance to increase. The mismatch between the high and low pressure stream capacitances at the cold end of the recuperator give rise to a large pinch point, or temperature difference between the hot and cold streams, reducing the cycle's efficiency. Even though the RCBC compresses a fraction of the mass flow at a higher temperature resulting in greater compression work, the splitting of the low pressure stream before the LTR is done to match the stream capacitances. Therefore, temperature differences in the LTR are reduced, improving the cycle's efficiency.

The T-s diagram in Fig.2.5 corresponds to a s-CO_2 RCBC. The cycle has a cycle high pressure of 200 [bar] and a cycle low pressure of 78 [bar]. The cycle high temperature is 650 [°C] and the cycle low temperature is 27 [°C]. The ratio between the mass flow that goes to the recompressor and the total mass flow is known as the recompression fraction φ. As a RCBC has two recuperators, care must be taken to ensure the outlet from the recompressor and the high pressure stream exiting the LTR are at the same pressure and temperature. In a RCBC the heat load of the recuperators is larger than the heat supplied to the cycle.

As mentioned in the previous section, s-CO_2 has a comparatively high energy density. This entails that for a given power output, s-CO_2 turbomachinery is smaller than steam turbomachinery. Figure 2.6 shows how for an output of 300 [MW] s-CO_2 turbomachinery is a tenth the size of a conventional steam turbine. This implies less material is required to fabricate the turbomachinery which in turn could translate into substantial capital savings. On the other hand, due to the high heat loads and high cycle pressures the LTR and HTR require large heat exchange areas and robust construction. Among the candidates for recuperator technology Printed circuit heat exchangers stand out. The heat load of the LTR is a fraction of the heat load of the high temperature recuperator (henceforth HTR). The HTR can see a heat transfer of four times the magnitude that of the LTR [13]. The heat exchange area for the HTR is close to two times that of the LTR [18].

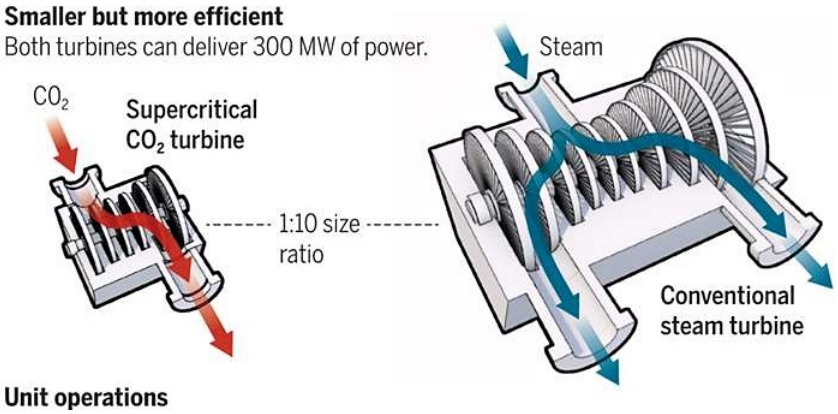

Figure 2.6: s-CO_2 and steam turbomachinery size comparison [19]

The Brayton cycle has the compressor and the turbine on the same shaft, thus transmitting the power required by the compressor from the turbine directly. When off-design operation is not an exception but the norm, a single shaft layout lacks the flexibility required to compete on a price basis with other sources of energy [16][20]. A two-shaft layout where the recompressor is on the independent shaft has been proposed and extensively studied. As

described in the literature, it has higher flexibility than the single-shaft configuration yet not as much as a three-shaft layout. The obvious shortcoming in increasing the number of shafts is the rise in capital expenditure associated with the purchase and operation of new shafts and the motors required to power the compressors.

As the turbine shaft is commonly connected to the generator, and power generation requires the generator to be synchronised, turbine speed should not vary continuously as would be the case if the power block where used for propulsion purposes. Therefore, turbine shaft speed can vary as a control variable but care must be taken to synchronise with the power grid.

A RCBC can be water-cooled, air-cooled or cooled by a mixture of water and air cooling systems (hybrid cooling) [21]. Water cooling allows for higher cycle efficiencies but sourcing water tends to be a challenge in places with high solar potential (deserts). On the other hand, air-cooling means lower cycle efficiencies, yet the increased cycle low temperature also entails operating further away from the critical point. This can be advantageous for off-design performance.

2.3 PCHE

Printed circuit heat exchangers (henceforth PCHE), also known as diffusion bonded microchannel heat exchangers are highly compact heat exchangers that can be up to 85% lighter and smaller than conventional heat exchangers [22]. This is thanks to the heat exchange area to volume ratio achieved due to the construction method, Fig. 2.7 shows the scale of the channels in a PCHE cutaway.

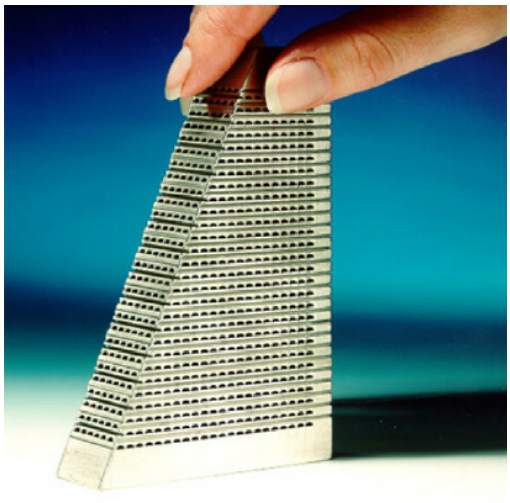

Figure 2.7: PCHE cutaway[22]

The heat exchange area to volume ratio is in the order of 1500 [m^{-1}] [18]. PCHE dimensions are in the order of 1 [mm] for channel width and 0.5 [mm] for channel depth. PCHE are built by stacking etched plates atop each other which are then bonded through atomic diffusion at high temperature high pressure conditions. The result is a heat exchanger that is able to withstand high pressures and high temperatures, with a characteristic channel shape

due to the etching process. The channel shape can be described as a half ellipse, and thus the hydraulic diameter can be estimated through the following expressions in terms of a and b as shown in Fig. 2.8.

$$D_h = \frac{4 \cdot A}{P} \tag{2.3}$$

where D_h is the hydraulic diameter, A is the cross sectional are of the channel and P is the perimeter of the cross section. The area of the channel, described as a half ellipse is given by:

$$A = \frac{\pi ab}{2} \tag{2.4}$$

where a is half the width of the channel and b is the depth. The perimeter of the channel section can be described as the top length plus half an ellipse. The length of this half ellipse in turn can be described with increased accuracy by the following expressions: a half circle with a radius the average of a and b, through the second half of approximation 2.6, or through the second half of approximation 2.7, Ramanujan's approximation for the perimeter of a half ellipse.

$$P = 2a + \frac{\pi}{2}\left(\frac{a+b}{2}\right) \tag{2.5}$$

$$P = 2a + \pi\sqrt{\frac{a^2+b^2}{2}} \tag{2.6}$$

$$P = 2a + \frac{\pi}{2}\left(3(a+b) - \sqrt{(3a+b)(a+3b)}\right) \tag{2.7}$$

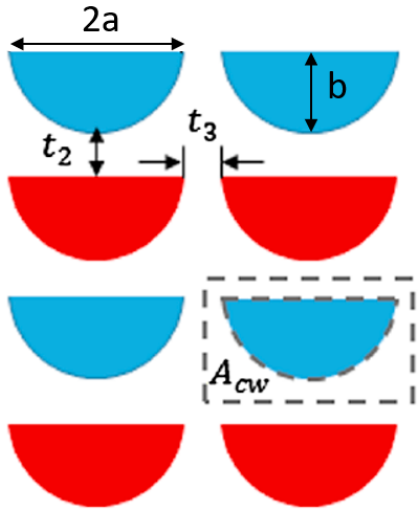

Figure 2.8: PCHE channel section diagram

2.4 TES

A TES system is a system that enables the stockpiling of excess thermal energy. Molten salt TES technology allows for the storage of surplus solar energy through the molten salt's sensible heat. Said TES systems grant CSP power plants the ability to store excess heat that is not used to generate electricity during the day in an insulated molten salts tank. After sunset, the thermal energy of the salts can be used to produce steam and generate electricity. TES systems can also be used to smooth electricity production and mitigate the variability associated with solar energy.

Molten salt TES systems have hot and cold insulated tanks as shown in Fig. 2.9. Molten salts from the cold tank are pumped to the power tower where they are heated. Then the hot salts are pumped into the hot tank, where they are stored for later use. When the power block needs heat input, molten salts from the hot tank transfer their heat to the power block's working fluid through a heat exchanger (steam generator in Fig. 2.9). The now cooled molten salts are pumped into the cold tank, completing the cycle. Molten salts are solid at room temperature and atmospheric pressure, thus if their temperature drops enough they can solidify, causing great damage to piping and rendering the TES system useless. On the other hand, the thermal stability of each salt mixture also sets a constraint on the TES cycle's temperatures.

The common use of molten salt in TES systems in CSP power plants is due to how cost-competitive they are. On a per unit energy stored basis, molten salts can be as much as 33 times cheaper than lithium-ion batteries [23].

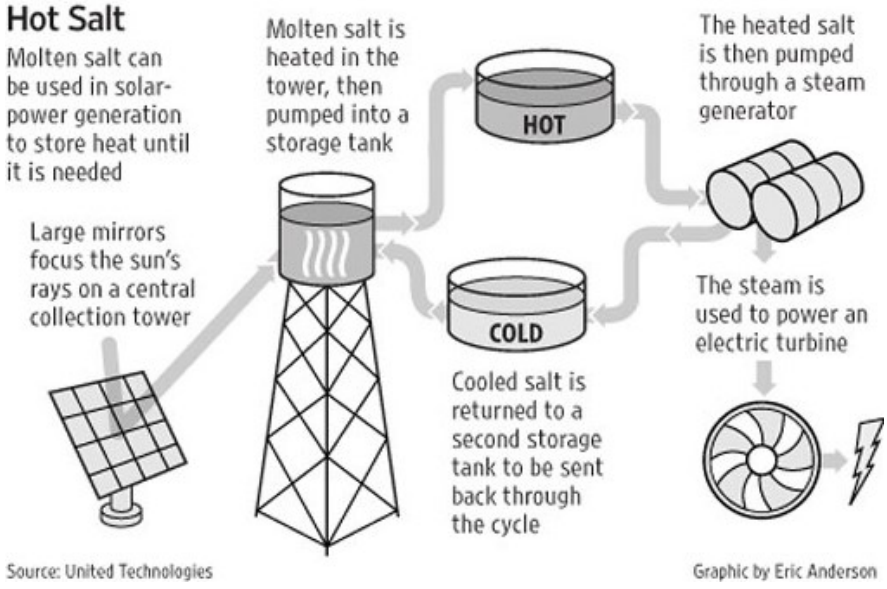

Figure 2.9: Molten salts TES system [24]

A common salt mixture used as thermal storage media for CSP is 60% $NaNO_3$ - 40% KNO_3. This mixture is also known as Solar Salt. It presents a melting point of 221 [°C] and it is stable up to 600 [°C], approximately.

In state-of-the-art TES systems, the salt mixture accounts for approximately 50% of total

capital costs. Mohan [25] proposed a new eutectic mixture of salts capable of operating under high temperatures that is also low-cost when compared to other salt mixtures that include lithium salts in their composition. It is a Sodium-Magnesium-Potassium chloride mixture with the following composition: 24.5% NaCl - 20.5% KCl - 55% $MgCl_2$. This mixture presents a melting point of 387 [°C] and was shown to be stable at temperatures above 600 [°C].

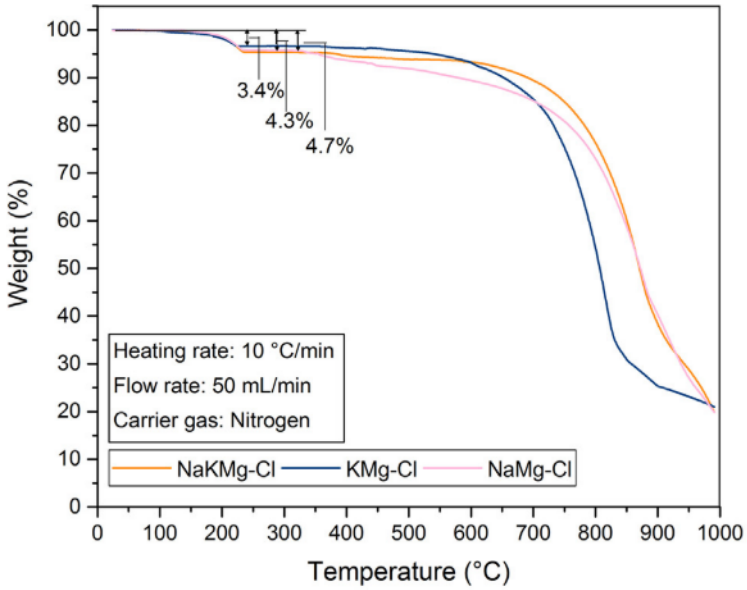

Figure 2.10: Mass loss of chloride mixtures in nitrogen atmosphere [25]

Figure 2.10 shows mass loss after thermal cycles. There is an initial dip corresponding to the saturation of the nitrogen atmosphere with salt vapour. As temperature increases mass continues to decrease. The reason behind the decrease is the testing methodology. In Mohan's experiment the sample had to be removed from the nitrogen atmosphere in order to measure it's weight, thus the chlorides that vaporised and saturated the nitrogen atmosphere were lost every time the sample's weight was measured leading to new chlorides vaporising in the nitrogen atmosphere and contributing with every measurement to mass loss.

2.5 Exergy & efficiencies

Exergy is defined as the maximum amount of useful work that can be extracted by bringing a system into equilibrium with the environment [26]. Unlike energy, exergy is not conserved. As a tool, it allows us to quantify and gauge inefficiencies in processes which in the interest of this work translates to power cycles. A brief summary of how and why an exergetic analysis brings new insight into process performance is given in the following statement: A first law analysis concerns itself withe energy losses, whilst an exergetic analysis concerns itself with useful energy losses.

Exergy is a property that depends both on the state of the system, and the environment. The Dead State is the state whereby a system has come into thermodynamic equilibrium with the environment. Physical exergy can be assessed through the following expression

(disregarding kinetic energy and potential energy effects):

$$\psi = (h - h_0) - T_0(s - s_0) \tag{2.8}$$

where ψ is the specific physical exergy, h is the specific enthalpy of the system, h_0 the enthalpy at the Dead State, T_0 is the temperature at the Dead State in [K], s the specific entropy of the system and s_0 the specific entropy at the Dead State. The present work considers the Dead State to be set at ambient temperature (dry-bulb temperature) and standard atmospheric pressure (1 [bar]).

There is no difference between work and exergy. Heat transfer however must be adjusted in order to be expressed in terms of exergy.

$$\Psi = Q \cdot \left(1 - \frac{T_c}{T_h}\right) \tag{2.9}$$

$$\Psi = Q \cdot \left(1 - \frac{T_0}{T_{source}}\right) \tag{2.10}$$

where Ψ is physical exergy, Q is the heat transferred, T_c is the cold temperature in [K], T_h is the hot temperature in [K], and T_{source} is the temperature at the interface at which the heat is transferred, in [K]. From equation 2.9 we can see the resemblance to Carnot theorem. It corrects heat flow to the maximum theoretical work that could be obtained from such heat flow.

2.5.1 First and second law efficiency

The cycle's first law and second law efficiencies are given by:

$$\eta_{cycle} = \frac{\dot{W}_{net}}{\dot{Q}_{in}} \tag{2.11}$$

$$\eta_{ex,cycle} = \frac{\dot{W}_{net}}{\dot{\Psi}_{in}} \tag{2.12}$$

where η_{cycle} is the cycle's first law efficiency, $\eta_{ex,cycle}$ is the second law efficiency, $\dot{W}_{net}$ is the net power output, $\dot{Q}_{in}$ is the heat intake and $\dot{\Psi}_{in}$ is the exergy supplied to the power cycle.

The assessment of $\dot{\Psi}_{in}$ depends on where the control boundary for the power cycle is set. The irradiance on the solar field can be used as the supplied exergy, as can be the exergy the molten salts provide to the s-CO_2 in the PHX or the exergy gained by the s-CO_2 in the PHX. These three options yield different values for the cycle's second law efficiency. As the solar field modelling is no the main focus of the present work, the second boundary is chosen. Expanding cycle net power output and expressing exergy supplied to the power cycle as a function of molten salts exergy change the second law efficiency can be rewritten as:

$$\eta_{ex,cycle} = \frac{\dot{W}_{turb} - \dot{W}_{comp} - \dot{W}_{recomp}}{\dot{\Psi}_{salt,in} - \dot{\Psi}_{salt,out}} \tag{2.13}$$

where $\dot{W}_{turb}$ is the turbine power output, $\dot{W}_{comp}$ is the compressor's power consumption, $\dot{W}_{recomp}$ is the recompressor's power consumption and $\dot{\Psi}_{salt,in}$ and $\dot{\Psi}_{salt,out}$ represent the physical exergy of the molten salt as it enters and leaves the PHX.

Chapter 3

Literature review

Gianfranco Angelino [11] in 1968 compared the theoretical efficiencies of power cycles using s-CO_2 as working fluid. The efficiencies that s-CO_2 power cycles can achieve surpass reheated steam and perfect gas cycles as seen in Fig. 3.1 with cycle high temperatures above 550 [°C]. A RCBC can achieve efficiencies on excess of 50% (CYCLE A in Fig. 3.1) whilst maintaining a relatively simple thermodynamic cycle. Greater conversion efficiencies can be achieved if reheating is added to the RCBC (A REHEAT in Fig. 3.1) but the increase in complexity outweighs the benefits. Angelino evaluated the theoretical conversion efficiencies of these cycles and even though his work was aimed towards water cooled nuclear energy, it sparked interest in s-CO_2 cycles, in particular the potential of the RCBC. His analysis considers design-point operation and thus further work on the off-design performance followed.

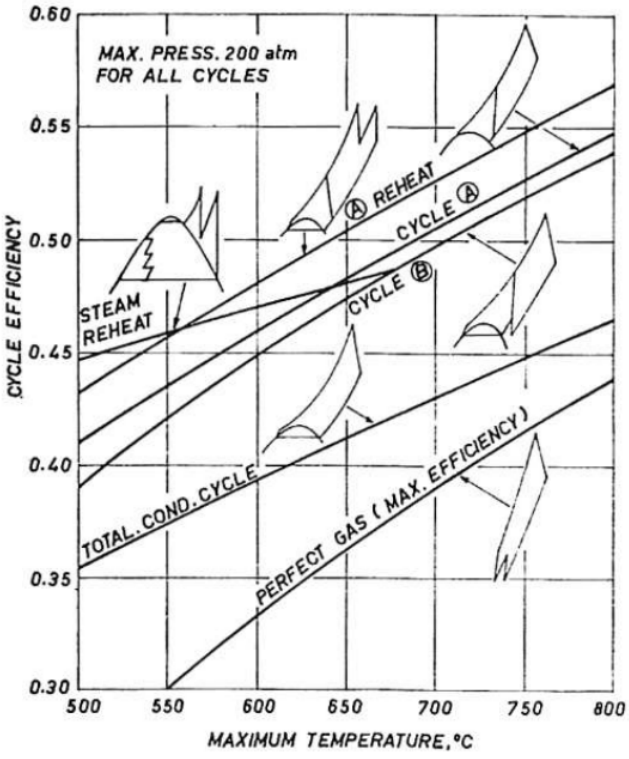

Figure 3.1: Efficiency of CO_2 condensation cycles compared with steam and perfect-gas [11]

Nathan Carstens [27] in 2007 described s-CO_2 RCBC transients. His work is among the earliest on RCBC transient modelling methodologies. Three cycle control strategies were implemented and studied: a high-low temperature control, turbine bypass and inventory control. The high-low temperature control refers to compressor's inlet temperature and turbine's inlet temperature respectively. Turbine bypass is a bypass somewhere in the cycle that reduces the mass flow to the turbine. Inventory control refers to increasing or decreasing the amount of working fluid in the power block in order to increase or decrease the cycles pressure. High temperature control was shown to be an inefficient strategy, turbine bypass on the other hand is a viable and fast strategy yet not as efficient as inventory control. Nonetheless, inventory control is not as fast as turbine bypass. Inventory control coupled with low temperature control where found to be the best strategy. Carstens model describes a single-shaft, constant speed system. The cycle recompression fraction φ is varied in order to avoid choke or stalling in the compressors. The side-effect of such measure is a mismatch in compressor-recompressor outlet pressures. Therefore, a throttling valve is implemented after the recompressor to match the compressor outlet pressure. System mass flow rate is not constant in his model and both cycle high and low temperature are non constant with the objective of assessing the efficiency of said control strategies. Likewise, cycle low pressure is also a modelling variable subject to changing cycle income heat.

William Seidel [21] in 2010 assessed the suitability of s-CO_2 Brayton cycles for use as the power block in CSP power plants. Seidel's work evaluated the performance of the cycles using a simplified methodology. He analysed parametrically how the cycle's first law efficiency varied in accordance to parameters such as pressure ratio and heat exchanger area. He modelled the annual performance of the cycles and found them to outperform the Rankine cycle. Seidel studied the RCBC under three cooling schemes, water, hybrid and air cooled. The seasonal first law efficiency for a water-cooled cycle was 41.6%, hybrid cooling (mixture of water and air cooling) resulted in a seasonal first law efficiency of 41.4% and finally, the seasonal first law efficiency for the air-cooled cycle was 39.7%. Seidel used a more detailed modelling methodology for the heat exchangers in the cycle. He used the Gnielinski [28] correlation to determine the size required for the recuperators and the Petukhov [29] correlation to estimate the pressure drop through the recuperators. Turbomachinery was solved using constant design isoentropic efficiencies and design inlet-outlet pressures. Seidel's model does not include turn-up or turn-down modelling. It does account for changes in environmental conditions through changes in the parasitic fan load required to cool the work fluid to design temperature as ambient temperature varies through the year. This control strategy completely annuls the negative side effects associated with changes in compressor and recompressor inlet. The shortcoming of this control strategy lies on the requirement of ambient temperatures low enough to achieve the desired low cycle's temperatures. No matter how high the parasitic fan power is, it is not possible to cool the cycle to a temperature cooler than ambient temperature. Therefore Seidel's strategy is not feasible in locations like deserts where ambient temperature regularly surpass 30 [°C] (see Fig. 4.2). Seidel's model estimates the power output and efficiency given ambient temperature and cooling scheme, power output is a result rather than an input. Seidel's model describes a cycle with a single shaft layout. Turbomachinery speed along with recompression fraction, Mass flow rate and cycle high and low pressures are constant.

John Dyreby [16] in 2014 identified the need for a model capable of describing the perfor-

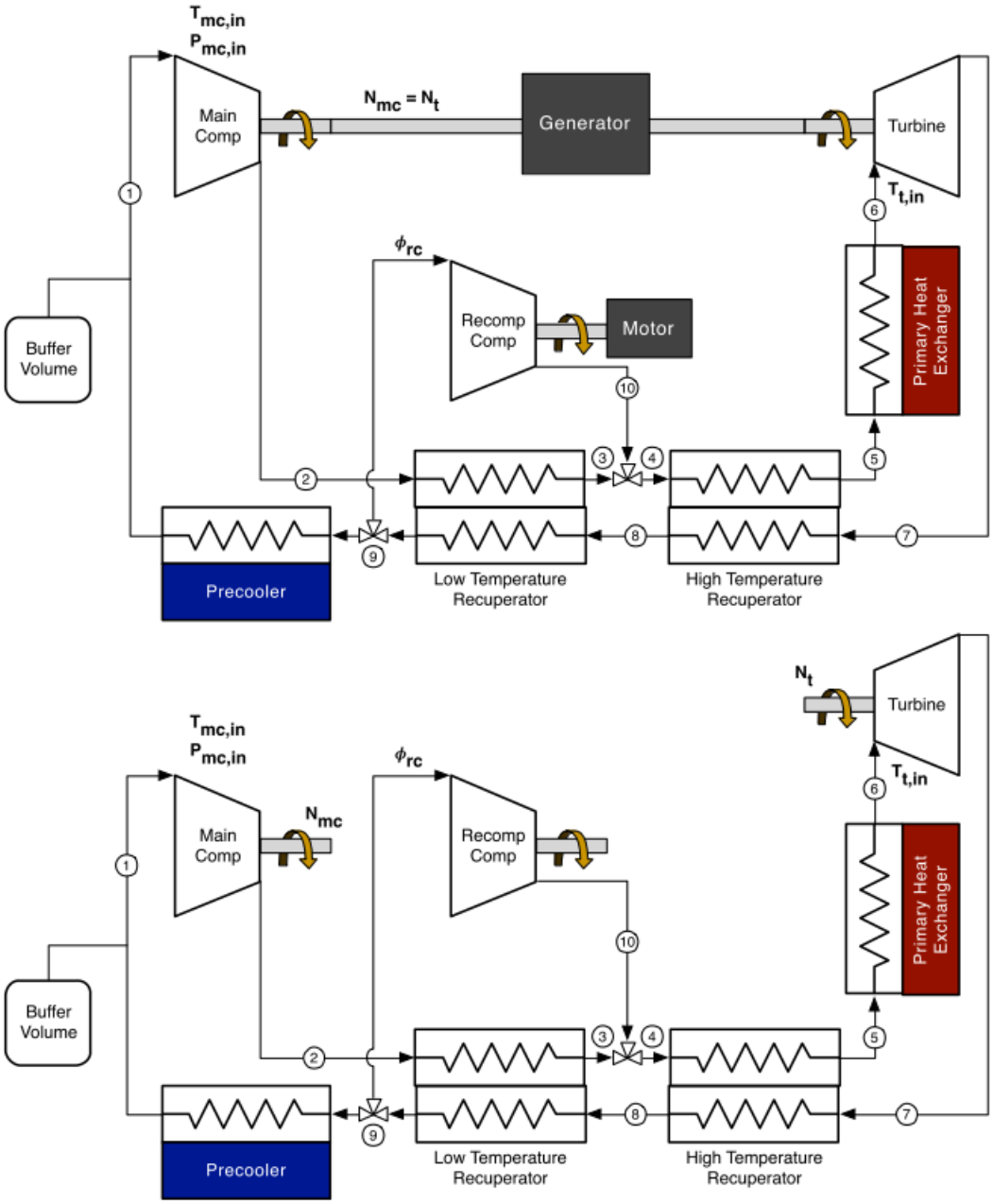

Figure 3.2: Diagrams of two-shaft and three-shaft RCBC [16]

mance of s-CO_2 cycles under off-design and part-load operational conditions. He considered turbomachinery models based on the performance maps of the compressor and turbine on the Sandia National Laboratories (henceforth SNL) test loop [30] [18]. His model has the turbine and the main compressor sharing a shaft whilst the recompressor spins on a different one. This two-shaft configuration is presented in Fig. 3.2. A highly simplified check for surge in turbomachinery is implemented for the compressor and recompressor. The ε-NTU methodology is employed for the heat exchangers in the cycle, assuming constant conductance (UA) the recuperators (low and high temperature recuperators) are discretized into sub-heat exchangers. A pressure drop of 1% is assumed for all heat exchangers in the cycle. The turbine is considered as a fixed section nozzle. Dyreby's work marked a before and after

in the off-design performance description of s-CO_2 RCBC. However, plenty of the strong modelling assumptions made by Dyreby still remain in current literature. The working fluid mass flow rate is determined by intersecting the head-flow curve of the compressor with the flow resistance curve characteristic of the turbine as shown in Fig. 3.3. This problem is solved subject to: compressor inlet temperature, compressor inlet pressure, turbine inlet temperature, recompression fraction, compressor shaft speed and turbine shaft speed. This last two inputs are independent in a three-shaft layout but identical in a two-shaft cycle layout. Dyreby analyses the operation of the cycle under different discrete values of cycle low temperatures. There is no strategy implemented to mitigate the negative effects of off-design low temperature operation, or to modulate the cycle's power output.

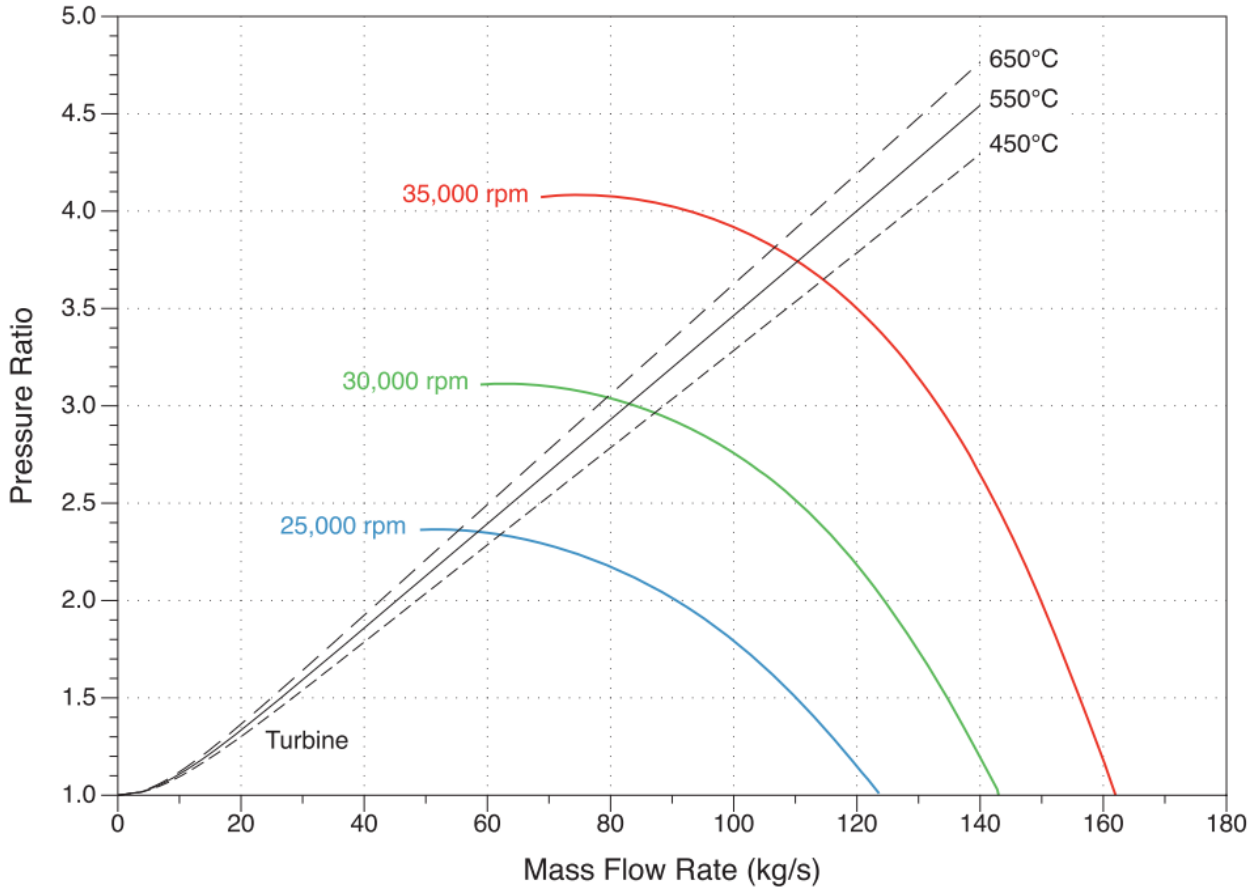

Figure 3.3: Head-flow and flow resistance curves for different shaft speeds and turbine inlet temperature [16]

Dyrbey's model is able to describe both a single and a two-shaft cycle layout. In either case shaft speed is variable. Mass flow and recompression fraction are also cycle input variables. Cycle low pressure is a cycle input but the high pressure is calculated. No limitation for the cycle high pressure is implemented into the model.

Ingo Jahn [31] in 2017 made further advances in the modelling of off-design performance by applying empiric curves that describe the behaviour of the turbine in off-design conditions (Mass Flow Parameter as seen in Fig. 3.4 a). He found decreasing turbine inlet temperature to be a detrimental strategy to reduce cycle net power output. Jahn proposes the reduction in specific speed of the turbine-compressor shaft as a viable turn-down strategy. Like

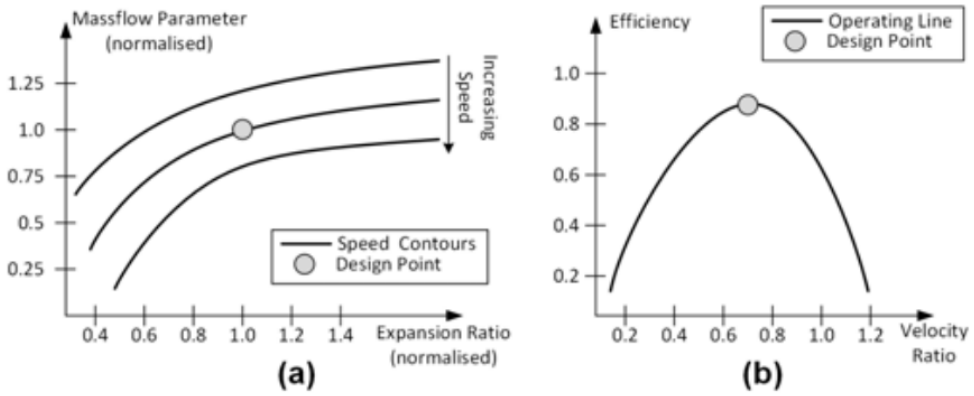

Figure 3.4: Maps of mass flow parameter (a) and efficiency (b) for radial inflow turbines [31]

aforementioned authors, Jahn did not consider a physical pressure drop model in his cycle modelling methodology. Like Dyreby, he also made use of the ε-NTU and constant conductance methodology to describe the off-design performance of heat exchangers. The effect pressure drop has in a RCBC shouldn't be underestimated. Although compression work is comparatively small in a RCBC, pressure drop in the heat exchanger reduces the differential pressure the turbine perceives. Enthalpy drop through the turbine depends heavily on this pressure differential and thus the failure to properly account for the pressure drop in a cycle can lead to gross overestimation of the cycle's performance. Jahn analyses the operation of the cycle under different discrete values of cycle high temperature and compressor and recompressor shaft speeds. His results are in agreement with Carsten's, high-temperature control is a detrimental control strategy. On the other hand, reducing compressor (and recompressor) shaft speed as a control strategy yields better results. As the compressors spin slower, the pressure rise through them decreases, therefore there is a decrease in cycle high pressure. This lower cycle high pressure translates into a smaller enthalpy drop through the turbine. This high cycle pressure change has a small effect on turbine's spouting velocity, and consequently cycle efficiency is not heavily degraded. This strategy requires appropriate inventory control in order to reduce the mass flow rate and maintain compressor (and recompressor) inlet pressures. Jahn's model can be better described as a three shaft cycle layout, where all shafts spin at different yet constant rotational speeds. The off-design operation is studied under constant turbine speed and reduced speeds for the compressor and recompressor. Recompression fraction is also a variable used in the study of off-design performance.

Correa [20] in 2019 optimised the recompression fraction under off-design conditions subject to ambient temperature and heat supplied maximising cycle efficiency . This allowed him to assess cycle performance under varying ambient temperature and net power output (obtained thanks to heat supplied and cycle efficiency). Correa's model operates under a single shaft, variable speed cycle layout. His cycle optimises the recompression fraction as a function of cycle low temperature and cycle income heat.

The previous paragraphs provide insight into some off the many different cycle control strategies. The time constant for these control strategies varies significantly and the applicability of the control strategies depends on the cycle's constraints. A first-rate control strategy for a power plant in a dispatch mode following the demand is one that enables an extensive range of power output whilst ensuring high cycle efficiency, fast turn-up, turn-down

and safeguard long-term equipment integrity and grid stability.

Different studies have been devoted to the s-CO_2 RCBC under different modelling constraints aiming to represent actual operational conditions. The most evident example for such constraints is the relationship between turbomachinery rotational speed. On a single shaft cycle layout all turbomachinery operate at the same rotational speed, whether it be fixed or variable. When a second shaft is incorporated to the cycle layout which turbomachines share the first shaft and which is on the new separate shaft becomes a new variable. Additional to this, whether the first or second shaft spin at constant or variable speed is independent of the others condition. This also applies when a third shaft is considered, it soon becomes apparent how different authors models behave differently in view of their constraints.

Table 3.1: Shaft modelling summary

Author	one-shaft	two-shaft	three-shaft
Carstens [27]	✓	x	x
Seidel [21]	✓	x	x
Dyreby [16]	✓	✓	x
Correa [20]	✓	x	x
Jahn et al. [31]	x	x	✓

The table above summarises the best description for how the presented models describe cycle operation. Through the studies described in this section important progress is observed regarding the off-design modelling s-CO_2 RCBC. Compressors are modelled through dimensionless coefficients, adjusted to fit experimental performance maps. Simplified routines are used to account for surge in the compressors. Heat exchangers are modelled through the constant conductance ε-NTU methodology, a methodology that does not contemplate pressure drop leading to alternate considerations like the 1% model. The non linear relationship between turbine conditions and mass flow is described through empirical Mass flow parameter - Expansion ratio curves. Different turn-down strategies are proposed and according to the constraints each work subjects it's model to. The probability that unknown phenomena is being overlooked by choosing simplified modelling methodologies is substantial and something that ought to be revised when dealing with novel cycles such.

The present work builds on the aforementioned methodologies, beginning with a detailed physics based model for heat exchangers that accounts for pressure drop. A more complete surge routine describes and predicts operational ranges, as well as monitoring when a turbomachine falls into a supersonic flow regime. The turbine is modelled through a hybrid of empirical data (performance map, Mass flow parameter curves) and a physical model (Ellipse law). Exergy is incorporated as an analysis tool to better diagnose, describe and explain operational phenomena. Solar irradiation, ambient temperature and grid demand determine the operation point, and the power block model determines the corresponding first law cycle efficiency allowing a simulation that consider meteorological conditions through a TMY file, quantifying the yearly performance of an air cooled s-CO_2 RCBC.

3.1 Compressor & Recompressor

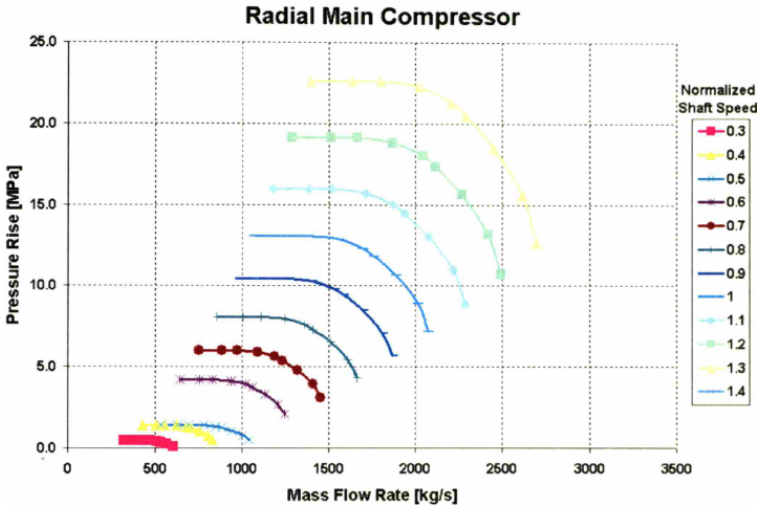

Figure 3.5: Radial Main Compressor Pressure Ratio Map [27]

Carstens [27] modelled the compressor and recompressor through GASS-PASS/CO_2 performance maps. This performance maps (Fig. 3.5) are used through normalised mass flow rates and normalised shaft speeds. Seidel [21] models the compressors operation through a simplified methodology where isoentropic efficiency is constant. Dyreby [16] as Carstens models his compressors through performance maps. His are based on the performance maps of the Barber-Nicholls s-CO_2 compressors in the SNL test loop [32]. Fig. 3.6 corresponds to the compressor performance map of the compressor found in the SNL test loop. There is a predicted surge line to the left side of the compressor map, yet this surge lines is conservative as can be seen by the operational data points that lie to it's left. The performance map is implemented through non dimensional coefficients. This coefficients are the flow coefficient ϕ and the ideal head coefficient Ψ.

$$\phi = \frac{\dot{m}}{\rho U D^2} \tag{3.1}$$

$$\Psi = \frac{\Delta h}{U^2} \tag{3.2}$$

where $\dot{m}$ is the mass flow in [kgs^{-1}], ρ the inlet density in [kgm^{-3}], U is the rotor tip speed in [ms^{-1}], D is the rotor diameter in [m] and Δh is the isoentropic specific enthalpy rise through the compressor. The rotor tip speed is related to shaft speed through:

$$U = \frac{DN}{2} \tag{3.3}$$

where N is the shaft rotational speed in [rads^{-1}].

These coefficients, as well as the expression for isoentropic efficiency are adjusted by a

term to account for changes in shaft speed. The adjusted forms are as follow:

$$\phi^* = \phi\left(\frac{N}{N_{design}}\right)^{\frac{1}{5}} \tag{3.4}$$

$$\Psi^* = \Psi\left(\frac{N_{design}}{N}\right)^{(20\phi^*)^3} \tag{3.5}$$

$$\eta^* = \eta\left(\frac{N_{design}}{N}\right)^{(20\phi^*)^5} \tag{3.6}$$

where ϕ^* is the modified flow coefficient, Ψ^* is the modified ideal head coefficient, η^* is the modified efficiency and N_{design} is the design shaft speed in [rads^{-1}].

These modified coefficients converse through the following polynomials:

$$\eta^* = -0.7069 + 168.6\phi^* - 8089\phi^{*2} + 182725\phi^{*3} - 1638000\phi^{*4} \tag{3.7}$$

$$\Psi^* = 0.04049 + 54.7\phi^* - 2505\phi^{*2} + 53224\phi^{*3} - 498626\phi^{*4} \tag{3.8}$$

The maximum efficiency is achieved at a modified flow coefficient of $\phi = 0.297035$. In order to assess whether the compressor undergoes surge a simple check is implemented into the model. If the flow coefficient is larger than 0.02, then it is sufficient to write off surge.

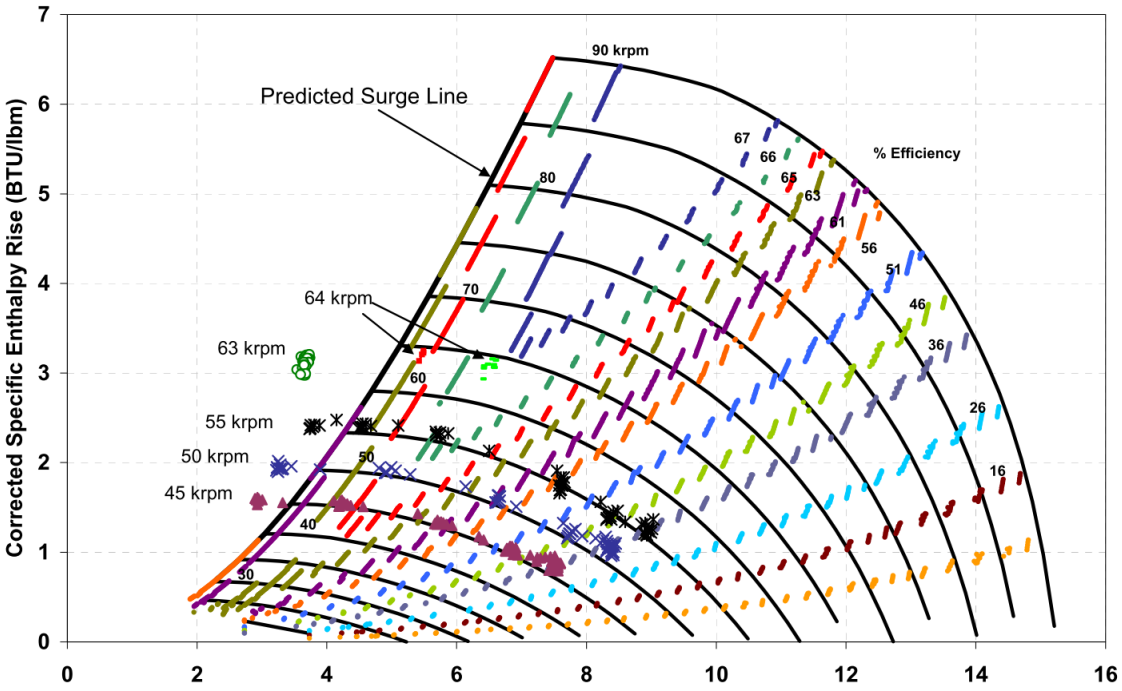

Figure 3.6: SNL Compressor performance map [18]

Jahn [31] models the compressors through performance maps. In order to account for operation at off-design conditions, mass flow rate, speed and enthalpy rise are adjusted using Glassman's relationships [33].

3.2 Turbine

Carstens [27] models the turbine considering the GAS-PASS/CO_2, such as the curve shown in Fig. 3.7. In Seidel's work the turbine is modelled by specifying the inlet fluid temperature and pressure, the outlet pressure, and the isoentropic efficiency of the turbine.

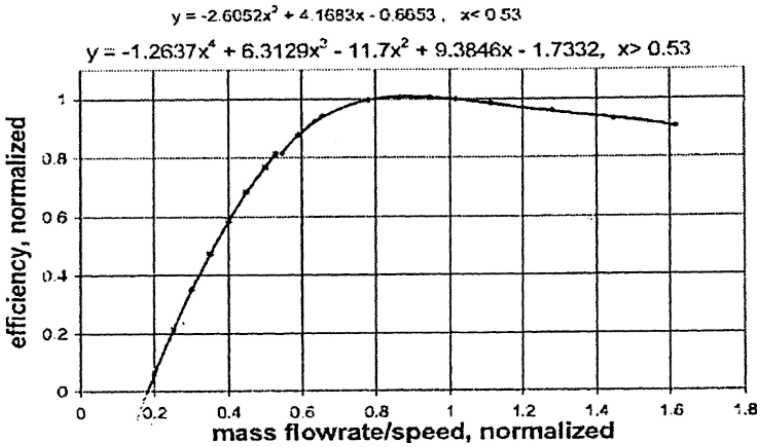

Figure 3.7: Original GAS-PASS/He Helium Axial Turbine Efficiency Performance Map [27]

Dyreby [16] models the turbine as a fixed section nozzle. According to this methodology mass flow through the turbine can be described through the following expression:

$$\dot{m} = \rho C_s A_{nozzle} \tag{3.9}$$

where ρ is the fluid density at turbine inlet, C_s is the spouting velocity and A_{nozzle} is the effective nozzle area. The spouting velocity is the velocity that would be achieved if the fluid expanded isoentropically from turbine inlet pressure to turbine outlet pressure. It is given by the following expression:

$$C_s = \sqrt{2\Delta h} \tag{3.10}$$

where Δh is the change in specific enthalpy corresponding to an isoentropic expansion between turbine inlet and outlet pressures. Turbine efficiency varies strongly as a function of the ratio between the tip speed U and the spouting velocity.

$$\nu = \frac{U}{C_s} \tag{3.11}$$

where ν is the ratio of tip speed to spouting velocity. Fig. 3.8 shows the variation of the turbine's efficiency as a function of ν. This relationship is summarised in the following polynomial:

$$\eta_\nu = 1.709\nu + 1.551\nu^2 - 3.706\nu^3 + 1.297\nu^4 \tag{3.12}$$

This expression has its maxima at $\nu = 0.74376$.

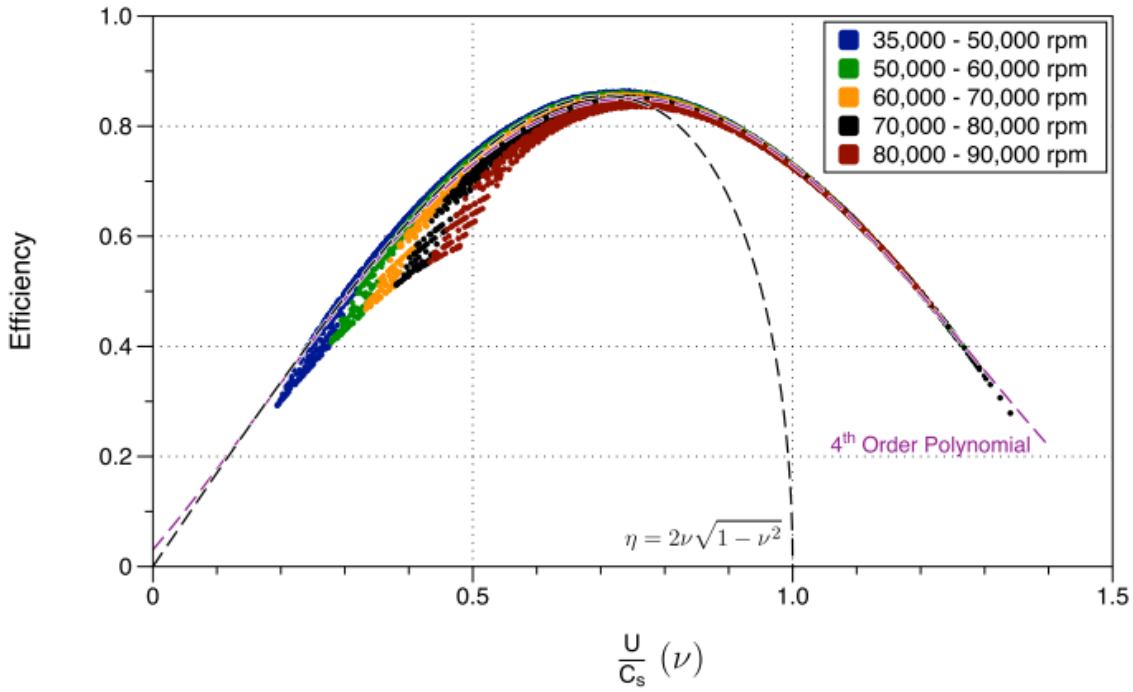

Figure 3.8: Efficiency predicted from performance map as a function of tip speed to spouting velocity ratio [16]

Jahn [31] models the non linear relationship between turbine mass flow and operation parameters through the mass flow parameter MFP and the equivalent speed N_{eq}. These expressions are given by:

$$MFP = \dot{m}\frac{\sqrt{T_{in}}}{P_{in}} \tag{3.13}$$

$$N_{eq} = N\sqrt{\frac{T_{in}}{T_{design}}} \tag{3.14}$$

where T_{in}, T_{design}, P_{in} and P_{design} stand for the temperature and pressure at the turbine inlet and at design conditions respectively. In particular, Jahn used the curves from the study by Hiett and Johnston [34].

The behaviour between mass flow and turbine operational conditions carried out by Glassman [33] on his 1972 paper shows how highly non linear the relationship is.

One of the earliest works on the description of said relationship belongs to Stodola [35]. Stodola's ellipse connects turbine inlet and outlet pressure to mass flow. It relates the MFP to the ratio between turbine inlet pressure to turbine outlet pressure .

$$\frac{MFP^2}{K^2} + \frac{1}{\Pi^2} = 1 \tag{3.15}$$

$$\Pi = \frac{P_{inlet}}{P_{outlet}} \tag{3.16}$$

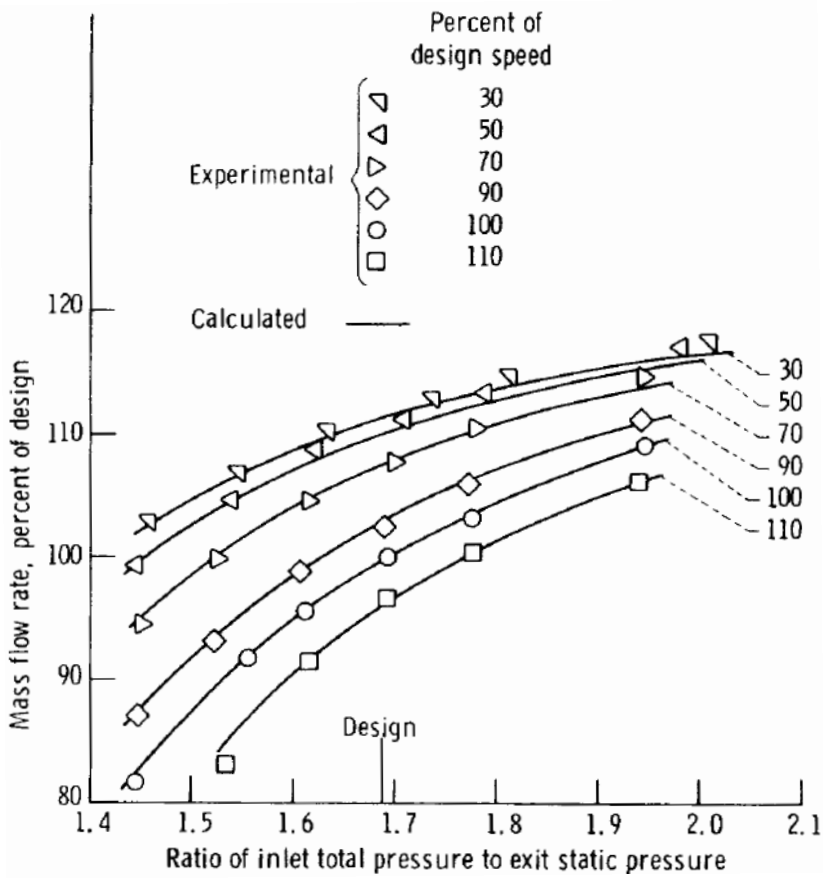

Figure 3.9: Comparison of calculated and experimental flow rates for odd-design operation [33]

where K is a constant and Π is the turbine pressure ratio. As an ellipse, there is a maximum mass flow parameter subject to the mathematical constraints of the ellipse formula. This bears resemblance to the physical phenomena of choked flow. There is a limit to the maximum mass flow through the turbine, no matter how much the ratio between pressures increases. This is observed on Fig. 3.9 as the curves flatten out towards the right of the graph.

3.3 Heat exchangers

Considering the abrupt change on the specific heat of s-CO_2 close to the critical point, the assumptions behind the $Q = UA\Delta T_{lm}$ model are not satisfied. As such different methodologies have been proposed to solve the heat transfer problem. Seidel [21] discretized the heat exchangers into small heat exchangers of unknown length, but with a known heat load. The length of each sub-section is calculated through the conductance associated with the heat load of each sub-exchanger.

$$\Delta Q = h \cdot \Delta A \cdot \Delta T \tag{3.17}$$

$$\Delta x_i = \frac{UA_i\left(\frac{1}{h_{H,i}} + \frac{1}{h_{C,i}} + ff\right)}{W_{ch}N_{ch}} \tag{3.18}$$

where ΔQ is the heat load for the sub-exchangers, h is the convection heat transfer coefficient, ΔT is the temperature difference between streams, Δx_i is the length of sub-exchanger, UA_i is the conductance of the sub-exchanger, $h_{H,i}$ and $h_{C,i}$ are the heat transfer coefficients on the hot and cold side respectively, ff is the fouling factor, W_{ch} is the channel width and N_{ch} is the number of channels. Once the conductance for each sub-heat exchanger is determined, heat transfer correlations are used to evaluate the global heat transfer coefficient U, and then the required area A is evaluated. With the dimensions of the recuperator channels, the area can be used to find the length of the sub-exchanger. This length can then be used to evaluate pressure drop through the heat exchanger. Regarding heat transfer, Seidel used the Gnielinski correlation [28]:

$$Nu_{D_h} = \frac{\left(\frac{f}{8}\right)\left(Re_{D_h} - 1000\right)Pr}{1 + 1.27\left(Pr^{\frac{2}{3}} - 1\right)\sqrt{\frac{f}{8}}} \tag{3.19}$$

Kruizenga [36] studied the validity of various heat transfer correlations for s-CO_2. He found the Jackson correlation to provide the best results, followed by Gnielinski's. This in part due to Jackson's having a term to account for proximity to the critical point.

A different approach for assessing heat transfer in the LTR and HTR is the ε-NTU method. The conductance of a stream is obtained through:

$$\dot{C} = \dot{m} \cdot c_p \tag{3.20}$$

where $\dot{C}$ is the stream conductance, the product of specific heat and mass flow. The maximum heat transfer depends on the lowest conductance:

$$\dot{Q}_{max} = \dot{C}_{min}(T_{hot,in} - T_{cold,in}) \tag{3.21}$$

where $\dot{Q}_{max}$ is the maximum heat transfer and $\dot{C}_{min}$ is the lowest conductance. Using the aforementioned values, heat transfer can be assessed through the Number of heat transfer

units NTU, the capacitance ratio and the efficiency of the heat exchanger:

$$NTU = \frac{UA}{\dot{C}_{min}} \tag{3.22}$$

$$C_r = \frac{\dot{C}_{min}}{\dot{C}_{max}} \tag{3.23}$$

$$\varepsilon = \frac{1 - exp(-NTU(1 - C_r))}{1 - C_r exp(-NTU(1 - C_r))} \tag{3.24}$$

where C_r is the capacitance ratio and ε is the efficiency of the heat exchanger. The heat transferred corresponds to:

$$\dot{Q} = \varepsilon \cdot \dot{Q}_{max} \tag{3.25}$$

Thus the heat transfer problem can be solved by fixing the value for the conductance UA and the efficiency ε. This methodology has been widely used in the literature as it abstracts the problem behind heat transfer using s-CO_2. It's shortcomings are that no pressure drop is considered in the formulation of the heat transfer problem and that constant conductance and constant efficiency are two strong assumptions.

3.3.1 Pressure drop

Seidel used the Petukhov (also known as Filinenko's) correlation for the form loss coefficient [29].

$$f = \frac{1}{(0.79ln(Re_{D_h}) - 1.64)^2} \tag{3.26}$$

where f is the friction form loss coefficient and Re_{D_h} is the Reynolds number with the hydraulic diameter as the characteristic length. Pressure drop is then evaluated through the following expression:

$$\Delta P = \frac{L}{D_h} f \rho \frac{v^2}{2} \tag{3.27}$$

where ΔP is the pressure drop, L is the length, D_h is the hydraulic diameter and v is the speed. There are also correlations for the pressure drop associated with the entrance and exit from the recuperators such as those described in Dostal's work:

$$\Delta P = C \rho \frac{v^2}{2} \tag{3.28}$$

where C equals 0.5 for the entrance manifold and 0.1 for the exit manifold.

Other correlations for the friction form loss coefficient involving s-CO_2 used in the literature are the following:

$$f = 0.3905 Re_{D_h}^{-0.0355} \tag{3.29}$$

$$f = 1.336 Re_{D_h}^{-0.1268} \tag{3.30}$$

$$f = 0.316 Re_{D_h}^{-0.25} \tag{3.31}$$

where the first and second correlations where empirically regressed from Heatric data [37], and the third correlation is the Blasius correlation [38].

3.4 SNL test loop

The SNL test loop is a split flow recompression test loop, as shown in Fig. 3.10. It is composed by: a compressor, a recompressor, two turbines, a LTR and HTR, a Cooler and Heaters that act like the PHX. Despite having two turbines, unlike the single turbine found in RCBC, the cycles are equivalent from a thermodynamic perspective.

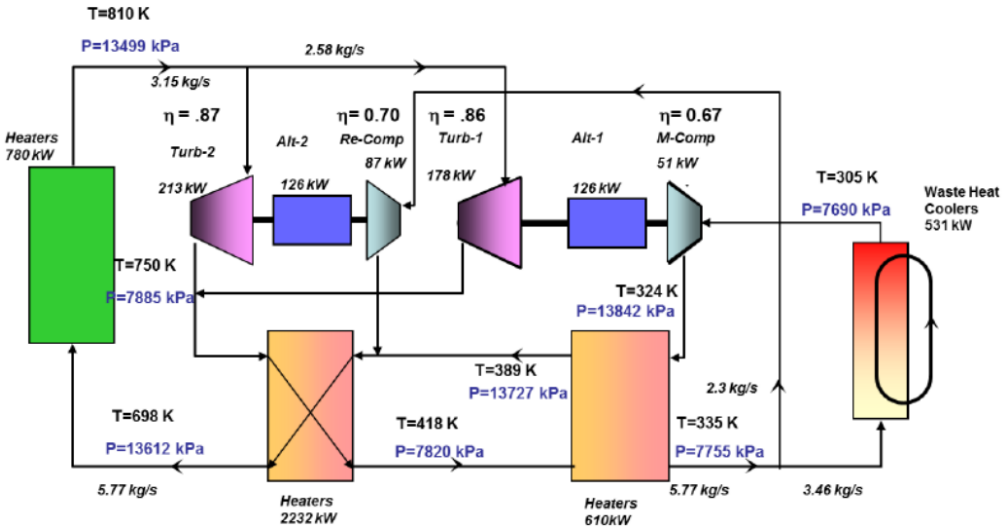

Figure 3.10: Schematic of Sandia's split flow recompression test cycle [13]

Table 3.2: SNL test loop information

Variable	Value
D_{comp} [mm]	37.36
N_{comp} [revmin^{-1}]	75000
η_{comp} [%]	67.3
$P_{in,}$ [bar]	76.9
$P_{out,comp}$ [bar]	141.12
$\dot{W}_{comp}$ [kW]	47.8
D_{recomp} [mm]	41.55
N_{recomp} [revmin^{-1}]	110130
η_{recomp} [%]	70.2
$P_{in,}$ [bar]	77.9
$P_{out,recomp}$ [bar]	140.08
$\dot{W}_{recomp}$ [kW]	85.1
D_{turb} [mm]	72.34
N_{turb} [revmin^{-1}]	75000
η_{turb} [%]	84.7
$P_{in,}$ [bar]	136
$P_{out,turb}$ [bar]	83.3
$\dot{W}_{turb}$ [kW]	331.1

Variable	Value
A_{LTR} [m^2]	18.0
a_{LTR} [mm]	0.48
b_{LTR} [mm]	0.66
L_{LTR} [m]	0.5842
$\dot{Q}_{LTR}$ [kW]	515
$\dot{Q}_{out}$ [kW]	455
A_{HTR} [m^2]	43.0
a_{HTR} [mm]	0.635
b_{HTR} [mm]	0.77
L_{HTR} [m]	0.996
$\dot{Q}_{HTR}$ [kW]	2202
$\dot{Q}_{in}$ [kW]	662
T_{low} [°C]	32.25
T_{high} [°C]	537.85
P_{low} [bar]	76.9
P_{high} [bar]	141.12
$\dot{m}$ [kgs^{-1}]	5.35
φ [-]	0.382

As showcased in Fig. 3.10, TIT is 810 [K] or 537.85 [°C], substantially lower than the TIT pursued in literature which is closer to 650 [°C]. Another important difference between the

test loop and the cycle studied in literature are the cycle pressures. The cycle low pressure is 76.9 [bar] and the cycle high pressure is 141.12 [bar] in the test loop, whilst in the literature cycle high pressure is close to 200 [bar]. These discrepancies are to be expected from a test loop as many operational challenges such as turbomachinery seals are still being worked on. This last point is reflected in the lack of mass conservation in the test loop, or rather the leaks along it. With a mass flow of 5.35 [kgs^{-1}] of s-CO_2 (before leaks), the test loop's net power output is 198.2 [kW].

Table 3.2 summarises the information presented in [18] and [13] regarding the test loop. The data for the turbine was obtained as the sum/average between the two turbines in the test loop when appropriate. It should be noted that whilst Fig. 3.10 presents many of the information presented in Table 3.2, information presented on [18] and [13] had precedence over that showcased in the schematic. When variables where not explicitly presented, as is the case for φ, they where estimated through available information ($\dot{m}_{comp}$ and $\dot{m}_{recomp}$).

3.5 Literature cycle

A scheme of the s-CO2 RCBC in accordance with the literature is used to benchmark the performance of the proposed cycle. This literature cycle has two shafts, with the compressor and the turbine sharing the main one. Both shaft's spin at variable speeds, with the recompressor's shaft spinning at such a speed as to match the pressure at the high pressure outlet of the LTR. The layout of this cycle is identical to the two-shaft layout shown in Fig. 3.2. The literature cycle is subject to the following constraints for off-design operation purposes:

- Cycle mass flow equal to or smaller than design mass flow.
- Cycle high pressure equal to or smaller than design cycle high pressure.
- Pressure at any point in the cycle must be equal to or smaller than design cycle high pressure.
- Fixed TIT.
- Fixed recompression fraction.

The first three constraints all stem from the intent to evaluate turn-down control strategies that do not severely deteriorate the components of the power block, minimising their life span reduction considering the everyday off-design operation. Cycle's net power output could be turned-up by increasing mass flow and cycle high pressure, but the damage equipment like the LTR, HTR, PHX and Cooler would endure due to creep and fatigue cycling would most probably imply a long term economical loss. The fourth constraint is chosen due to the literature showing high temperature control to be a poor turn-down control strategy. The final constraint reduces the complexity of the problem by foregoing the optimisation of off-design operation. In order to ensure that the design cycle high pressure is never surpassed, throttling valves are implemented into the model at the compressor's and the recompressor's outlets.

Chapter 4

Methodology

4.1 Meteorological conditions

The Crucero electrical substation is located in the Atacama Desert, 12 [km] north-east from Maria Elena. There is little to no urban settlements in the vicinity. It is representative of the large arid plains that dot the Atacama Desert. This together with the fact that electric utility companies want to be close to the substation make radiation and environmental measurements from here valuable for solar energy potential assessment in the region.

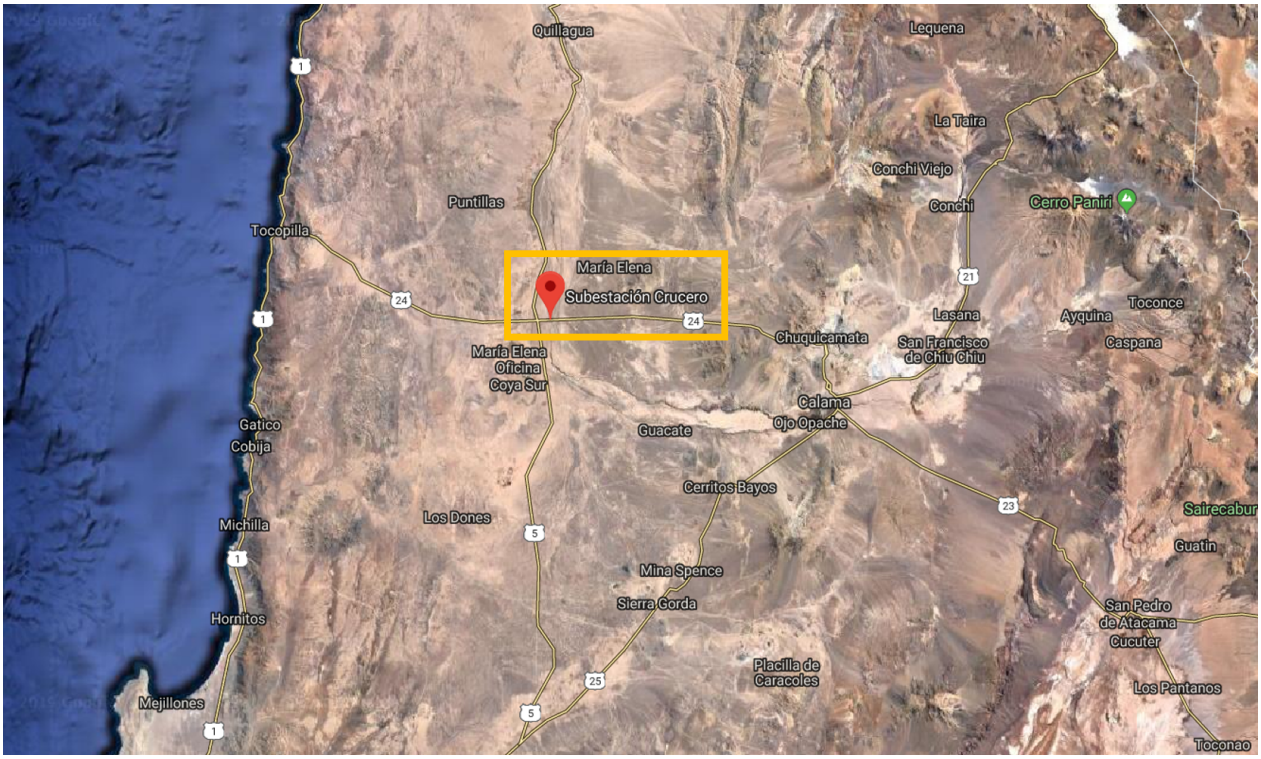

Figure 4.1: Crucero substation geographic location, *Google Maps* ®

The weather data used is a TMY file (typical meteorological year). TMYs are a set of meteorological data with data values for every hour in the year, for a specific geographical location. They are constructed by combining months from different years, where each selected

Table 4.1: Main characteristics of Crucero

Latitude	22.24 S
Longitude	69.51 W
Altitude	1146 [m.a.s.l.]
Annual DNI	3411 [kWhm^{-2}]
Design point DNI	1025 [Wm^{-2}]
Max. temperature	37.32 [°C]
Min. temperature	0.64 [°C]

month was the most "typical" of those registered. The TMY file used contains the following values for each of the 8760 hours in a year: Direct Normal Irradiance (DNI) as shown in Fig. 4.3, Direct Horizontal Irradiance (DHI), dry-bulb temperature as shown in Fig. 4.2, relative humidity, pressure, wind speed and wind bearing.

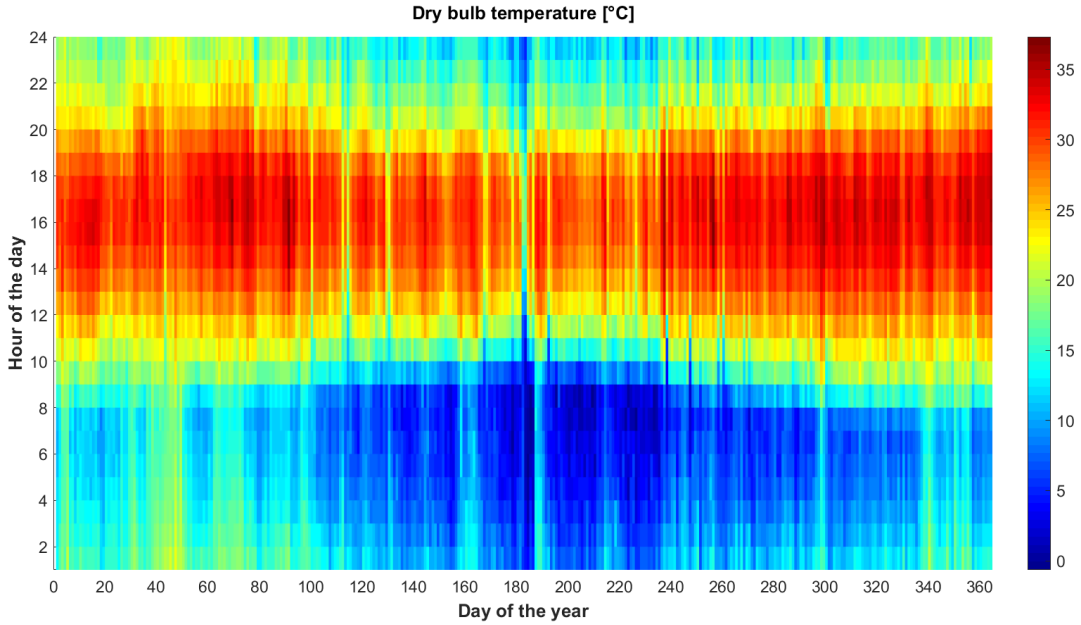

Figure 4.2: Dry bulb temperature in Crucero during the TMY

An important meteorological value is the design point of the direct normal irradiance. It is defined as the DNI at the 90% of the cumulative distribution function when disregarding the zero values. That is, the DNI is lower than the design point DNI 90% of the insolation time.

Fig. 4.3 exhibits a strong decrease in DNI during the month of February, this phenomenon is known as the Invierno altiplánico (or altiplanic winter, it's literal translation). It consists of orographic precipitation that stems from moist air masses coming out of the Amazon. It typically occurs between the months of January and March.

Throughout the year great changes occur both in ambient temperature and in DNI, the following table lists theses changes and the standard deviation of two metrics in order to quantify the spread in values. Table 4.2 lists, from left to right: average temperature, the standard deviation in temperature, average normal irradiation, the standard deviation in

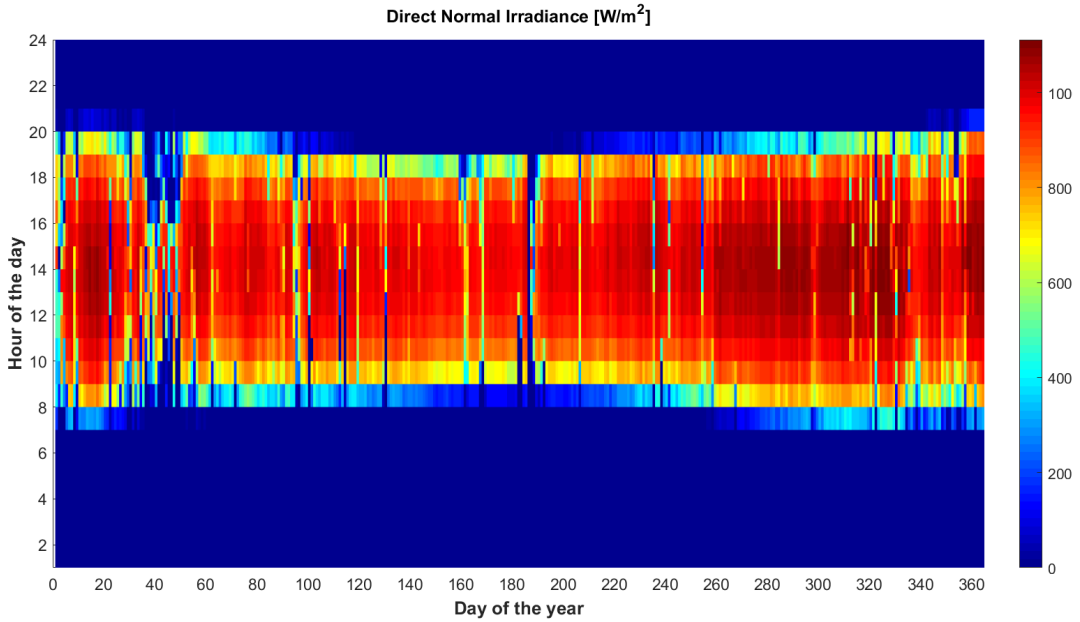

Figure 4.3: Direct Normal Irradiation in Crucero during the TMY

normal irradiation, the probability normal irradiation is greater than design point DNI and a value named MDPDNI (monthly design point DNI) which is the design point irradiation considering only that month's normal irradiation.

Table 4.2: Monthly Crucero data metrics

Month	$\overline{T}[°C]$	$\sigma\overline{T}[°C]$	$\overline{NI}[Wm^{-2}]$	$\sigma\overline{NI}[Wm^{-2}]$	P(NI>DPDNI)	MDPDNI [Wm^{-2}]
January	21.12	6.69	695.09	340.62	0.089	1020
February	22.19	6.28	542.02	381.23	0.036	981
March	22.21	7.41	732.58	299.86	0.007	986
April	19.06	8.00	703.19	328.79	0.020	1031
May	17.06	8.81	366.62	245.13	0.000	986
June	16.17	9.72	785.27	292.58	0.054	1014
July	14.98	9.48	696.21	348.04	0.000	987
August	16.17	9.72	785.27	292.58	0.054	1014
September	18.79	9.7	781.31	317.09	0.175	1041
October	19.74	9.56	864.05	253.91	0.326	1066
November	20.44	9.18	860.75	247.94	0.315	1075
December	21.77	8.11	761.82	310.93	0.124	1039

May had the lowest average DNI, with a value of 366.62 [Wm^{-2}]. An interesting trend is how the hotter months have a lower temperature standard deviation while the colder months have the highest. The MDPDNI does not vary significantly from month to month, on the other hand the probability normal irradiation is higher than the design point normal irradiation changes substantially. As a guideline, the probability should be close to 10%.

4.2 Cycle design

25 [MW] nears the limit for s-CO_2 radial turbine technology [31]. This net power output is the cornerstone of the cycle design. The second value established when designing the power cycle is the cycle high temperature, also known as Turbine Inlet Temperature (TIT henceforward) in Brayton power cycles. A reasonable yet slightly ambitious target, in accordance with the literature is 650 [°C]. The cycle's high and low pressure are 200 [bar] and 90 [bar] respectively. A low cycle pressure of 90 [bar] steers clear from the critical pressure of CO_2 at 73.8 [bar]. Although operating the cycle with a lower cycle low pressure would increase enthalpy drop through the turbine there are clear benefits in using a low cycle pressure higher than the critical pressure of CO_2. The adverse effects of operating near the critical point are mitigated by this increase in cycle low pressure. Cycle low temperature is defined by two modelling decisions. The first decision is to model the cooler with a fixed temperature pinch point, the second is to minimise the product of power output and deviation from design temperature. This can be stated as the following problem:

$$min \sum_{i \in I} M_i \cdot ((t_i + p) - t_{low,design})^2 \tag{4.1}$$

where M_i represents the demand multiplier in the dispatch matrix at instance i of the TMY, t_i represents the dry-bulb temperature at instance i of the TMY, and p represents the pinch point of the cooler. The intent behind this methodology is to find a cycle low temperature that considers the weather data from Crucero and minimises the discrepancy between design and operative conditions weighted by the power output dictated by the dispatch matrix.

Perhaps one of the most important parameters when it comes to RCBC design is the recompression fraction φ. This is set to 0.3, in accordance with the literature. The isoentropic efficiencies of the turbomachines are set to the same values used by Jahn [31]. Compressor outlet pressure, recompressor inlet and outlet pressure, turbine inlet and outlet pressure are chosen so as to achieve the cycle high pressure at turbine inlet and cycle low pressure at compressor inlet, whilst considering pressure drop through the cycle under design conditions. In an analogous manner, recompressor inlet design temperature is set in accordance with the temperature resulting of the conductances of the LTR and the HTR.

4.2.1 Component sizing

Once the cycles design point is set, it is necessary to size the components and parameters that define said components that make up the power block such that the values mentioned in the previous section are achieved.

Turbomachinery is sized for maximum efficiency at design point. This means a flow parameter $\phi = 0.297035$ for the compressors and the ratio of tip speed to spouting velocity $\nu = 0.74376$ for the turbine. For the compressors, this design mass flow parameter in conjunction with the design inlet pressure, temperature and design outlet pressure define the rotor diameter and design speed. Turbine diameter and turbine design speed are also set in order to achieve the determined ratio of tip speed to spouting velocity, where the spouting velocity depends on design turbine inlet temperature, temperature and design turbine outlet pressure. The inlet pressures, temperatures and outlet pressures of the compressor, recompressor and

the turbine are affected by heat transfer in the recuperators and pressure drop through the cycle. Therefore an iterative process is necessary to properly size the previously mentioned components.

Both the LTR and the HTR are modified, up-sized versions of those found in the SNL test loop [13]. Once the heat transfer problem and pressure drop is computed, the number of channels and recuperator length is varied until a cycle first-law efficiency near 50% is achieved.

Due to the modelling constrains used for both the Cooler and the PHX no sizing is required. Likewise, no sizing is considered for the mix chamber.

4.3 Literature vs. proposed cycle

The difference between the literature and the proposed cycle is the number of shafts, the cycle constraints and the turn-down strategy implemented. The literature cycle has the compressor and turbine sharing a shaft whilst in the proposed cycle there are three independent shafts. In the literature cycle, the compressor and the turbine, as seen in Fig. 4.4, spin at the same speed whilst the recompressor spins at a different speed. On the proposed cycle all the turbomachines spin at different speeds.

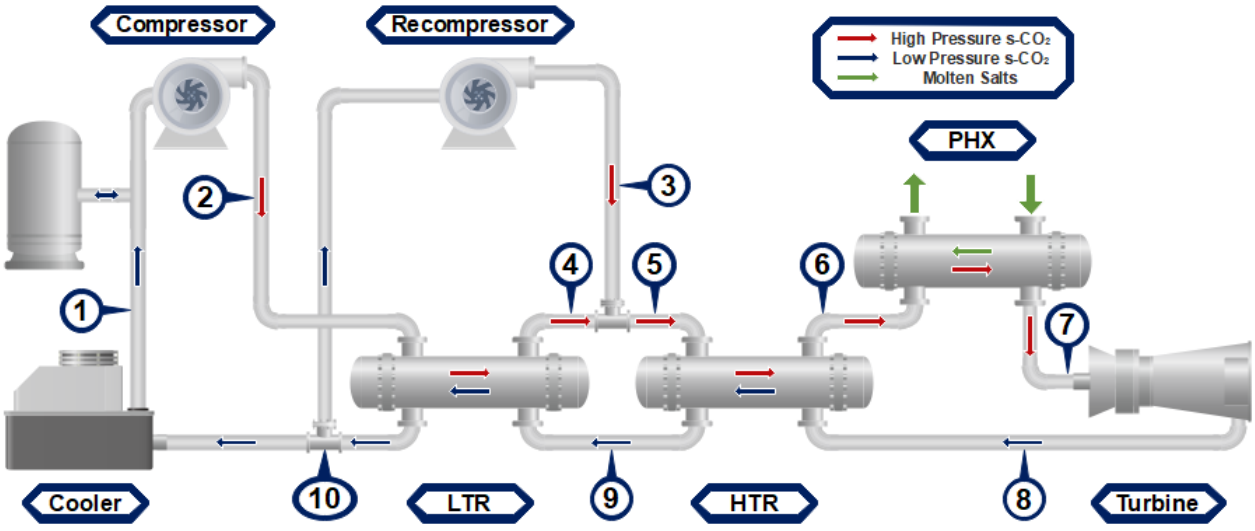

Figure 4.4: RCBC diagram with streams and numbering

Regarding control strategies, the literature cycle spins it's main shaft faster or slower, depending on the mass flow required to achieve the desired power output whilst the proposed cycle has the turbine spinning at a fixed speed. This takes away flexibility from the proposed cycle but it ensures there are no grid synchronisation issues. The proposed cycle, having three shafts can diminish the speed of both the compressor and recompressor shafts in order to modulate the cycle high pressure. This allows for less mass flow through the turbine, and the lower cycle high pressure also results in a decrease in turbine power output as well as a decrease in compression power consumption. On the other hand, the literature cycle can't adjust the compressor's speed independently from the turbine's and thus the pressure at the

outlet of the compressor can surpass the design cycle high pressure. In order to safeguard the integrity of the power block's components, the literature cycle has two throttling valves implemented into it's model in order to reduce the pressure at the exit of the compressors, in case cycle high pressure surpasses the design cycle high pressure.

The proposed cycle, for a given mass flow, spins the compressor and the recompressor at the speeds required to provide the pressure needed by the turbine to sustain said mass flow. The literature cycle solves for the compressor-turbine shaft speed necessary to achieve the desired mass flow (if it's feasible) and then solves for the recompressor speed needed to match pressures at the mix chamber, once the effect of the throttling valves is taken into consideration.

4.4 Turbine

The turbine model is based on Dyreby's, with the isoentropic efficiency function for the turbine retaining the form:

$$\eta_{turbine} = \eta_{turbine,design} \cdot \eta(\nu) \tag{4.2}$$

where $\eta_{turbine,design}$ is the turbine's isoentropic efficiency under design conditions.

4.4.1 MFP & Stodola

A novel hybrid methodology is coupled to the aforementioned turbine model in order to discard the constant nozzle area model and to replace it with one that takes into account the non-linear relationship between turbine operation parameters and mass flow. MFP curves for radial turbines such as the one presented in Glassman's [33] work are normalised and fitted. This fitting is then represented with Stodola's [35] Ellipse law model through two third degree polynomials, with the resulting fit presented in Fig. 4.5. The proposed model is a shaft-speed dependant Stodola ellipse fitted to experimental data.

The functional form of the model is as follows:

$$\frac{\overline{MFP}^2}{b(\overline{N})^2} + \frac{a(\overline{N})^2}{\overline{\Pi}^2} = 1 \tag{4.3}$$

where $\overline{MFP}$ is the normalised Mass flow parameter, b($\overline{N}$) is a third degree polynomial over normalised shaft speed, a($\overline{N}$) is another third degree polynomial over normalised shaft speed and $\overline{\Pi}$ is the normalised expansion ratio. The third degree polynomials are:

$$a(\overline{N}) = 0.1364104 \cdot \overline{N}^2 + 0.0166890 \cdot \overline{N} + 0.5190825 \tag{4.4}$$

$$b(\overline{N}) = -0.0264904 \cdot \overline{N}^2 + 0.0852502 \cdot \overline{N} + 1.2918869 \tag{4.5}$$

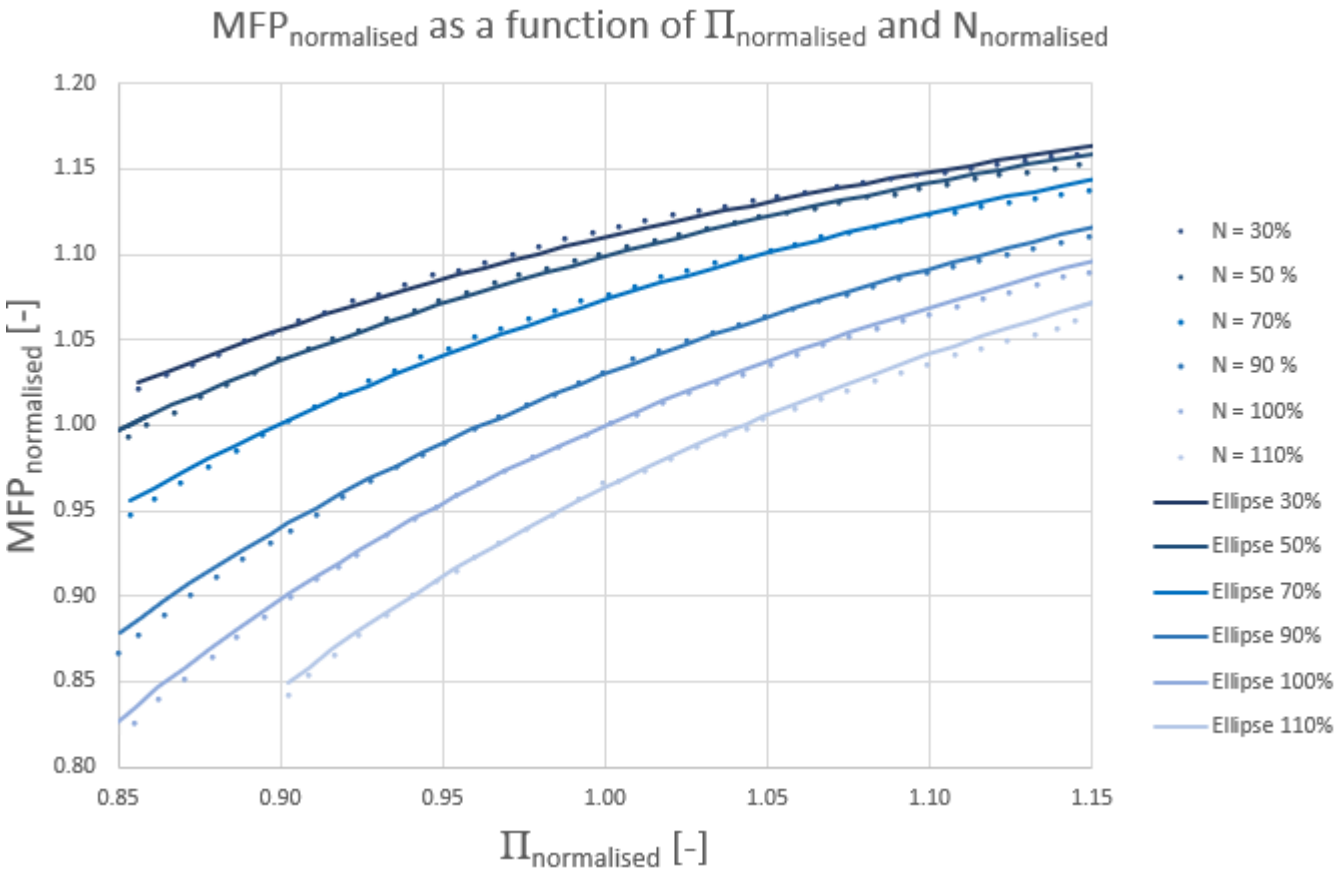

Figure 4.5: $\overline{MFP}$ as a function of $\overline{\Pi}$ and $\overline{N}$

The functional form of the implemented model can be further expanded and represented as:

$$\frac{\dot{m}\sqrt{T_{in}}P_{in,design}}{\dot{m}_{design}\sqrt{T_{in,design}}P_{in}} = b(\overline{N})\left(1-\left(\frac{a(\overline{N})P_{out}P_{in,design}}{P_{in}P_{out,design}}\right)^2\right)^{\frac{1}{2}} \tag{4.6}$$

$$\dot{m} = \frac{\dot{m}_{design}\sqrt{T_{in,design}}P_{in}}{\sqrt{T_{in}}P_{in,design}} \cdot b(\overline{N})\left(1-\left(\frac{a(\overline{N})P_{out}P_{in,design}}{P_{in}P_{out,design}}\right)^2\right)^{\frac{1}{2}} \tag{4.7}$$

$$\dot{m} = \frac{\dot{m}_{design}\sqrt{T_{7,design}}P_{7}}{\sqrt{T_{7}}P_{7,design}} \cdot b(\overline{N})\left(1-\left(\frac{a(\overline{N})P_{8}P_{7,design}}{P_{7}P_{8,design}}\right)^2\right)^{\frac{1}{2}} \tag{4.8}$$

TIT (T_7) is fixed in the present work, simplifying the previous expressions. The effective form of the model depends on the cycle constraints. The literature cycle operates with a variable turbine-compressor shaft speed, the expression for mass flow is therefore:

$$\dot{m} = \frac{\dot{m}_{design}P_{7}}{P_{7,design}} \cdot b(\overline{N})\left(1-\left(\frac{a(\overline{N})P_{8}P_{7,design}}{P_{7}P_{8,design}}\right)^2\right)^{\frac{1}{2}} \tag{4.9}$$

On the other hand, as the proposed cycle operates with a fixed turbine shaft speed the

effective form of the model is:

$$\dot{m} = \frac{\dot{m}_{design} P_7}{P_{7,design}} \cdot b(1) \left(1 - \left(\frac{a(1) P_8 P_{7,design}}{P_7 P_{8,design}} \right)^2 \right)^{\frac{1}{2}} \tag{4.10}$$

4.5 Compressors

Both the compressor and recompressor are modelled using the curves obtained by Dyreby [16], based on the performance curves (Fig.3.6) of the Barber-Nicholls compressor found in the SNL test loop [13]. The same dimensionless methodology is used whereby compressor performance is described as a function of: flow parameter ϕ, ideal head coefficient Ψ, and normalised shaft speed $\overline{N}$, through the modified versions of the first two parameters (ϕ^* Ψ^*).

4.5.1 Surge

The predicted surge line in Fig. 3.6 is used as the basis for the detailed surge prediction model implemented. The predicted surge line is fitted twice under different independent and dependant variables. The first fit, S_1 maps the predicted surge line as a function of normalised shaft speed to the flow parameter.

$$S_1(\overline{N}) \rightarrow \phi_{surge} \tag{4.11}$$

This first function returns for a given normalised shaft speed the flow parameter at which surge is predicted to occur, ϕ_{surge}. Thus, if the flow parameter is equal to or smaller than ϕ_{surge}, this function predicts the occurrence of surge.

The second fit, S_2 maps the predicted surge line as a function of ideal head coefficient and flow parameter.

$$S_2(\Psi) \rightarrow \phi_{surge} \tag{4.12}$$

If for a given ideal head coefficient the flow parameter is smaller than ϕ_{surge}, then said function predicts the occurrence of surge.

Both these functions are used in conjunction to determine if and when either the compressor or recompressor undergoes surge. The criteria used is both functions, S_1 and S_2 must predict surge for the model to treat it as such. Using only one of them yields unrealistic surge regions.

4.5.2 Supersonic flow

On a similar vein to the surge check functions, a simple check is implemented to assess if a compressor or recompressor is operating under supersonic regime. The local Mach number is computed at turbomachinery outlets according to the following expression:

$$M = \frac{\frac{DN}{2}}{c} \tag{4.13}$$

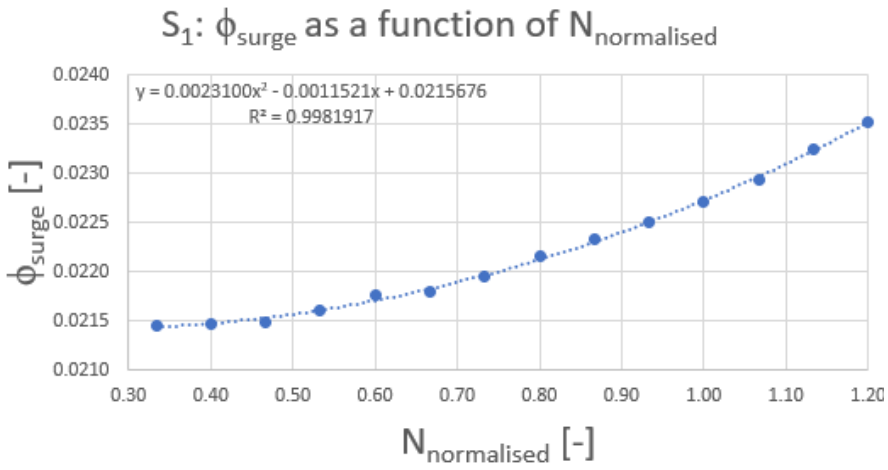

Figure 4.6: ϕ_{surge} as a function of $\overline{N}$

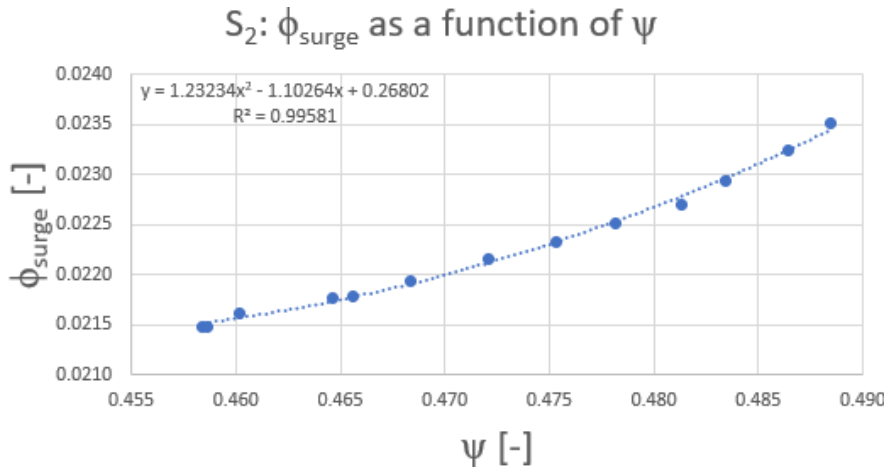

Figure 4.7: ϕ_{surge} as a function of ψ

where M is the local Mach number and c is the speed of sound. If M is equal to or greater than one then the compressor is operating at a supersonic flow regime.

4.5.3 M out of N systems

The proposed model contemplates a system where instead of a single compressor and recompressor, there are three smaller compressors and recompressors, as shown in Fig. 4.8. These smaller compressors would be sized in accordance to their proportional mass flow. The aim of this measure is to introduce additional control variables that grant flexibility to the power block for off-design operation purposes.

When some of the compressors are turned off, the mass flow is divided equally between the remaining compressors. This enables the power block to deal with smaller mass flows without the compressors undergoing surge (to certain extent). A simplified modelling assumption is used in the EES code, the mass flow parameter is adjusted by the number of on-compressors.

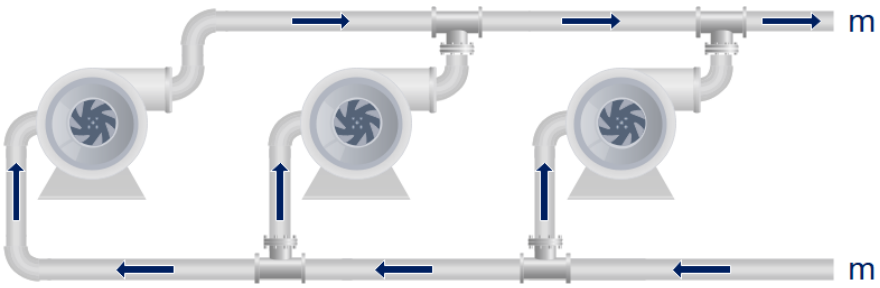

Figure 4.8: Proposed M out of N system diagram

$$\phi_{adjusted} = \phi \cdot \frac{n}{m} \tag{4.14}$$

where $\phi_{adjusted}$ is the adjusted mass flow parameter, n is the number of compressors/recompressors and m is the active number of compressors/recompressors. The number of active recompressors is independent of the number of active compressors, nonetheless, there is no point in adjusting one number to account for reduced mass flow without adjusting the other. Three configurations are defined, where the number of active recompressors is chosen so as to increase the operational range of the cycle and first-law efficiency, given the number of active compressors. Table 4.3 summarises the number of operational compressors and recompressors for both the literature and proposed cycle at the different configurations.

Table 4.3: M out of N configurations

Config.	Literature		Proposed	
	Comp	Recomp	Comp	Recomp
I	3	3	3	3
II	2	3	2	2
III	1	2	-	-

4.6 LTR & HTR

The heat transfer problem is solved in the recuperators through Gnielinski's correlation and pressure drop is solved for through Petukhov's correlation and Dostal's expression for inlet and exit manifold pressure drop. The thermal resistance associated to the metal between streams in the PCHE is disregarded as it's magnitude is negligible in comparison to the convective terms. Thus the global heat transfer coefficient is given by:

$$\frac{1}{U} = \frac{1}{h_{cold}} + \frac{1}{h_{hot}} \tag{4.15}$$

where U is the global heat transfer coefficient and h_{cold} and h_{hot} are the convection heat transfer coefficients for the cold and hot side of the recuperators respectively. Given a channel width of $2a$ and a channel depth of b, the following expression are used to assess the cross

sectional area of the channels, it's perimeter and hydraulic diameter:

$$A = \frac{\pi ab}{2} \tag{4.16}$$

$$P = 2a + \frac{\pi}{2}\left(\frac{a+b}{2}\right) \tag{4.17}$$

$$D_h = \frac{8\pi ab}{8a + \pi(a+b)} \tag{4.18}$$

with the above expressions describing the area as the area of a half ellipse and the perimeter using the approximation of a half circle with a radius the average between a and b. For one hot and cold pair of channels, the heat exchange area is assessed through:

$$A_{channel,pair} = L \cdot \left[2a + \frac{\pi}{2}\left(\frac{a+b}{2}\right)\right] \tag{4.19}$$

where $A_{channel,pair}$ is the heat exchange area for one pair of hot and cold channels in the PCHE. Therefore, the total heat exchange area is therefore:

$$A_{LTR/HTR} = N_{channel,pairs} \cdot L \cdot \left[2a + \frac{\pi}{2}\left(\frac{a+b}{2}\right)\right] \tag{4.20}$$

where $A_{LTR/HTR}$ is the heat exchange area of the recuperator and $N_{channel,pairs}$ is the number of channel pairs.

In order to account for the changes in s-CO_2's specific heat, both recuperators are discretized linearly into smaller recuperators along their length so the specific heat is approximately constant in the sub-heat exchangers, allowing for the use of the $Q = UA\Delta T_{lm}$ model for counter current heat exchangers. The HTR is discretized into four sub-heat exchangers, whilst the LTR is discretized into twenty sub-heat exchangers.

On each sub-heat exchanger, pressure drop and heat transfer is assessed through the following procedure: Given the temperature and pressure at the recuperator inlet, the s-CO_2's density ρ, dynamic viscocity μ, conductivity k, specific heat c_p and Prandtl number Pr. The velocity of the s-CO_2 is assessed as a function of mass flow, channel cross sectional area, number of channel pairs and density.

$$v = \frac{\dot{m}}{\rho \cdot N_{channel,pairs} \cdot A} \tag{4.21}$$

where v is the velocity of the s-CO_2 in one of the PCHE channels. This velocity is then used to evaluate the Reynolds number Re_{D_h}, which in turn is used to assess both the friction form factor f through Petukhov's correlation and the Nusselt number Nu through Gnielinski's. With the Nusselt number, the convection heat transfer coefficient is obtained. These are then used to express the heat transfer and pressure drop set of equations, coupled to the other sub-heat exchangers. This system of equations is then solved for iteratively by the EES program.

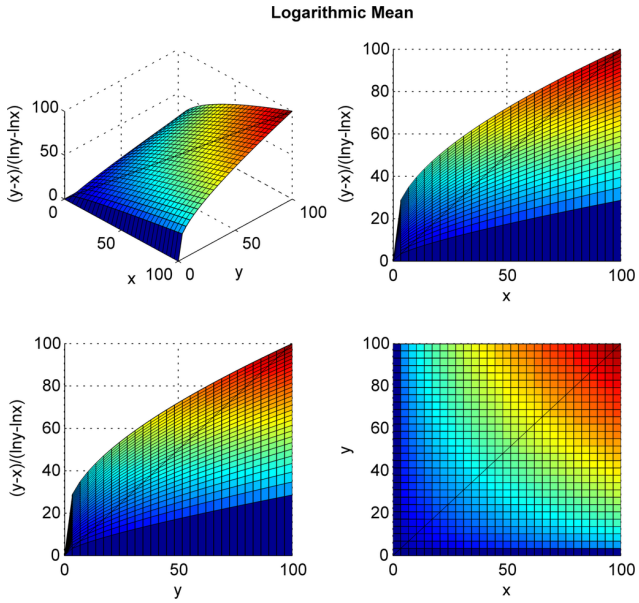

Figure 4.9: Logarithmic mean difference [39]

EES uses the Newton-Raphson method. When using said numerical method to solve for logarithmic mean temperature differences, the program often diverges due to the logarithmic mean function being ill-defined at the middle (see Fig. 4.9). The workaround implemented in this work is to pre-solve the cycle using arithmetic temperature differences, and to then use those results as the guess values for a second run of the EES program with logarithmic temperature differences. As the recuperators are sub-divided, the difference between temperature difference in one side and the other of the sub-heat exchangers is small enough for this method to function.

4.7 Cooler & PHX

Both the Primary Heat Exchanger and the Cooler are modelled through a simplified approach. The exit temperature for both components is fixed, as is the pressure drop. Pressure drop through the PHX is proportional to the pressure drop at the hot side of the HTR, and the ratio between heat transfer in the HTR and the PHX. Likewise, pressure drop in the Cooler is proportional to the pressure drop at the cold side of the LTR and the ratio between heat transfer in the LTR and the Cooler.

$$\Delta P_{PHX} = \Delta P_{HTR,hot} \cdot \frac{Q_{PHX}}{Q_{HTR}} \tag{4.22}$$

$$\Delta P_{Cooler} = \Delta P_{LTR,cold} \cdot \frac{Q_{Cooler}}{Q_{LTR}} \tag{4.23}$$

where ΔP_{PHX} is the pressure drop through the PHX, ΔP_{Cooler} is the pressure drop through the Cooler, $\Delta P_{HTR,hot}$ is the pressure drop through the hot side of the HTR and $\Delta P_{LTR,cold}$ is the pressure drop through the cold side of the LTR.

This approximation chooses the recuperator stream with the closest conditions to those found in the Cooler and PHX. For the Cooler, the low pressure stream of the LTR is the most akin as it shares a similar pressure and the LTR outlet proceeds to the Cooler. Analogously, the high pressure HTR stream shares a similar pressure to the PHX and the HTR outlet goes into the PHX.

4.7.1 Cooler

The exit temperature from the cooler, T_1 is variable. The working fluid always leaves the cooler at ambient temperature plus a pinch point of 15 [K]. Said pinch point was chosen as a value representative of forced air cooling systems.

$$T_1 = T_{ambient} + p \tag{4.24}$$

where T_1 is the cycle low temperature at the Cooler's outlet, $T_{ambient}$ is the dry-bulb temperature and p is the aforementioned pinch point.

4.7.2 PHX

The PHX outlet temperature for s-CO_2, T_7 is set to the design TIT of 650 [°C]. Therefore the mass flow of molten salts is such that the heat supplied equals that absorbed by the s-CO_2.

$$\dot{m}(h_{out} - h_{in}) = \dot{m}_{salt}(h_{in,salt} - h_{out,salt}) \tag{4.25}$$

$$\dot{m}(h_7 - h_6) = \dot{m}_{salt}(h_{in,salt} - h_{out,salt}) \tag{4.26}$$

where $\dot{m}_{salt}$ is the molten salts mass flow, $h_{in,salt}$ and $h_{out,salt}$ are the enthalpies of the molten salts at the inlet and outlet of the PHX respectively. The temperature at which the salts enter and exit the PHX are fixed at 700 and 550 [°C] respectively. These temperatures are chosen so as to enable a TIT of 650 [°C] and to ensure the salts won't freeze.

4.8 Exergy accounting

The following balance is the cornerstone for exergy accounting in the present work:

$$\Psi_{in} = \Psi_{out} + \Psi_{dest} \tag{4.27}$$

where Ψ_{in} is the physical exergy that enters the component, Ψ_{out} the physical exergy that exits the component and Ψ_{dest} is the physical exergy destroyed in the component. This expression takes different forms depending on the cycle component. The formula for $\Psi_{destroyed}$ for each component is presented along the following diagrams.

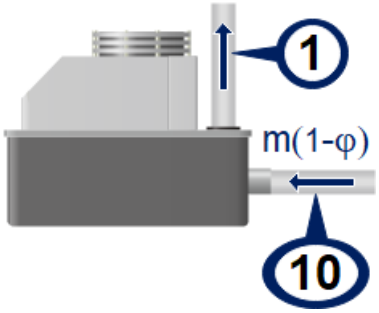

$$\dot{m}(1-\varphi)\psi_{10} = \dot{m}(1-\varphi)\psi_1 + \Psi_{dest,Cooler} \tag{4.28}$$

$$\Psi_{dest,Cooler} = \dot{m}(1-\varphi)\big(\psi_{10} - \psi_1\big) \tag{4.29}$$

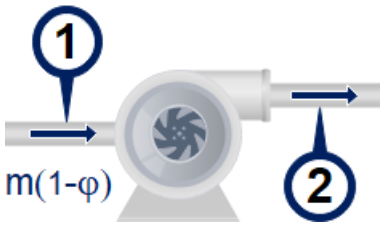

$$\dot{m}(1-\varphi)\psi_1 + \dot{W}_{comp} = \dot{m}(1-\varphi)\psi_2 + \Psi_{dest,comp} \tag{4.30}$$

$$\Psi_{dest,comp} = \dot{W}_{comp} - \dot{m}(1-\varphi)\big(\psi_2 - \psi_1\big) \tag{4.31}$$

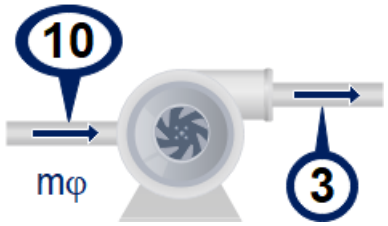

$$\dot{m}\varphi\psi_{10} + \dot{W}_{recomp} = \dot{m}\varphi\psi_3 + \Psi_{dest,recomp} \tag{4.32}$$

$$\Psi_{dest,recomp} = \dot{W}_{recomp} - \dot{m}\varphi\big(\psi_3 - \psi_{10}\big) \tag{4.33}$$

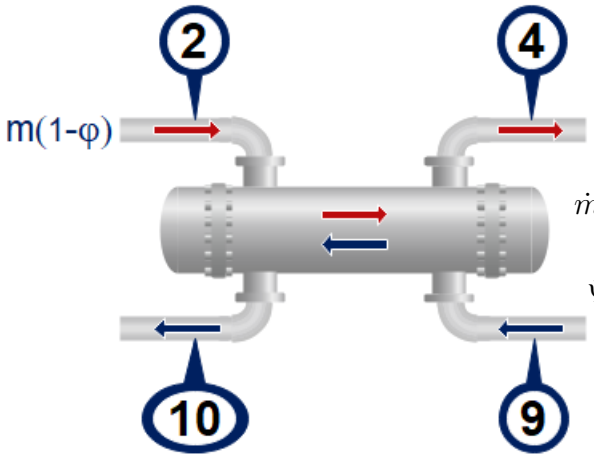

$$\dot{m}\big((1-\varphi)\psi_2 + \psi_9\big) = \dot{m}\big((1-\varphi)\psi_4 + \psi_{10}\big) + \Psi_{dest,LTR} \tag{4.34}$$

$$\Psi_{dest,LTR} = \dot{m}\big((1-\varphi)(\psi_2 - \psi_4) - (\psi_9 - \psi_{10})\big) \tag{4.35}$$

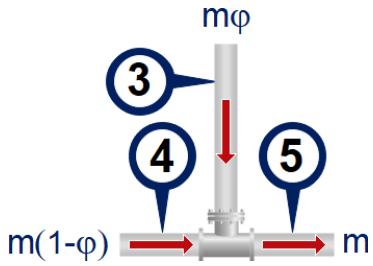

$$\dot{m}\big((1-\varphi)\psi_4 + \varphi\psi_3\big) = \dot{m}\psi_5 + \Psi_{dest,Mix} \tag{4.36}$$

$$\Psi_{dest,Mix} = \dot{m}\big((1-\varphi)\psi_4 + \varphi\psi_3 - \psi_5\big) \tag{4.37}$$

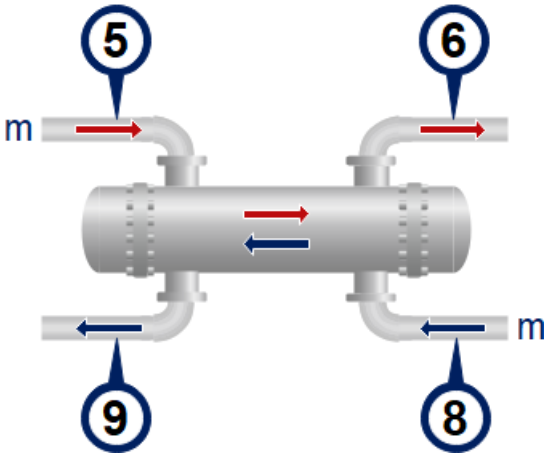

$$\dot{m}\big((\psi_5 + \psi_8\big) = \dot{m}\big(\psi_6 + \psi_9\big) + \Psi_{dest,HTR} \tag{4.38}$$

$$\Psi_{dest,HTR} = \dot{m}\big((\psi_5 - \psi_6) - (\psi_8 - \psi_9)\big) \tag{4.39}$$

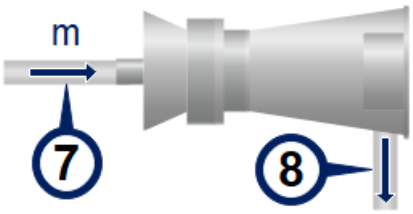

$$\dot{m}\psi_7 = \dot{W}_{turb} + \dot{m}\psi_8 + \Psi_{dest,turb} \tag{4.40}$$

$$\Psi_{dest,turb} = \dot{m}\big(\psi_7 - \psi_8\big) - \dot{W}_{turb} \tag{4.41}$$

For molten salts, the appraisal of physical exergy requires the assessment of enthalpy and entropy at the Dead State, where they are no longer molten but in solid state. Specific enthalpy and entropy for solid salts can be estimated through:

$$h - h_0 = c_{p,liquid} \cdot (T - T_{fusion}) + \Delta h_{fusion} + c_{p,solid} \cdot (T_{fusion} - T_0) \tag{4.42}$$

$$s - s_0 = c_{p,liquid} \cdot ln\left(\frac{T}{T_{fusion}}\right) + \left(\frac{\Delta h_{fusion}}{T_{fusion}}\right) + c_{p,solid} \cdot ln\left(\frac{T_{fusion}}{T_0}\right) \tag{4.43}$$

where $c_{p,liquid}$ and $c_{p,solid}$ are the specific heats of the salts in liquid and molten state respectively, T_{fusion} is the fusion temperature of the salts and Δh_{fusion} is the specific enthalpy of fusion. As the appraisal of the salts physical exergy isn't the objective, but the assessment of the exergy supplied by the salts, the expression can be rewritten in terms of the enthalpy and entropy difference. Therefore exergy destruction in the PHX is evaluated through:

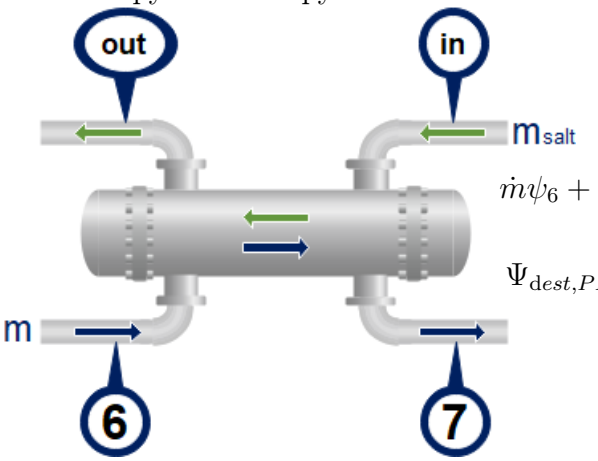

$$\dot{m}\psi_6 + \dot{m}_{salt}\psi_{salt,in} = \dot{m}\psi_7 + \dot{m}_{salt}\psi_{salt,out} + \Psi_{dest,PHX} \tag{4.44}$$

$$\Psi_{dest,PHX} = \dot{m}_{salt}(\Delta h_{salt} - T_0 \cdot \Delta s_{salt}) - \dot{m}(\psi_7 - \psi_6) \tag{4.45}$$

4.9 SNL comparison

The SNL test loop data is used in order to benchmark the results of the EES code and to assess the capability of the cycle model to properly describe the operation of a s-CO_2 RCBC. Only nominal operation is considered for comparison purposes in the present work due to the lack of off-design experimental data available in literature to date. The cycle information presented in [13] and [18] is fed to the EES code in order to model a digital version of the SNL test loop.

The results from the EES code are used to calculate parameters such as cycle efficiency, cycle input heat, cycle rejected heat, turbomachinery power consumption/generation, heat load in the recuperators and pressure drop through the recuperators. These parameters are then contrasted with those reported by Sandia.

4.10 Dispatch matrix

A dispatch matrix is a matrix describing in a simplified way how the power plant output varies throughout the year on a monthly and hour of the day basis. For example, the dispatch matrix for a power plant that provides the base load of the energy matrix (nuclear power plant for example) would consist of a matrix of ones, denoting how the power output does not vary with time. On the other hand, a peaking power plant may have all values coinciding with times between 1 am and 9 am filled with zeros, and have values of 1 during the time windows that match peak electricity demand (8 to 10 pm).

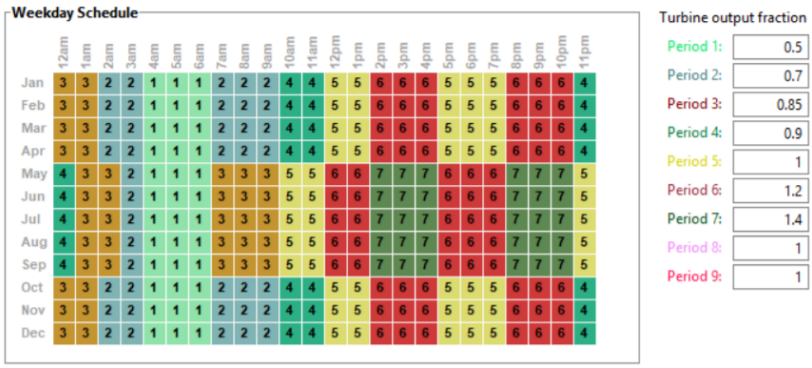

Figure 4.10: Demand following dispatch matrix [40]

The dispatch matrix used in this thesis corresponds to one developed by Bravo [40], shown in Fig. 4.10. It is a demand following dispatch matrix. In reality, there are two dispatch curves in this matrix, one for the months of May through September and the other for the remaining months. This matrix can be represented as the two load curves shown below in Fig 4.11 (when normalised by the maximum power output).

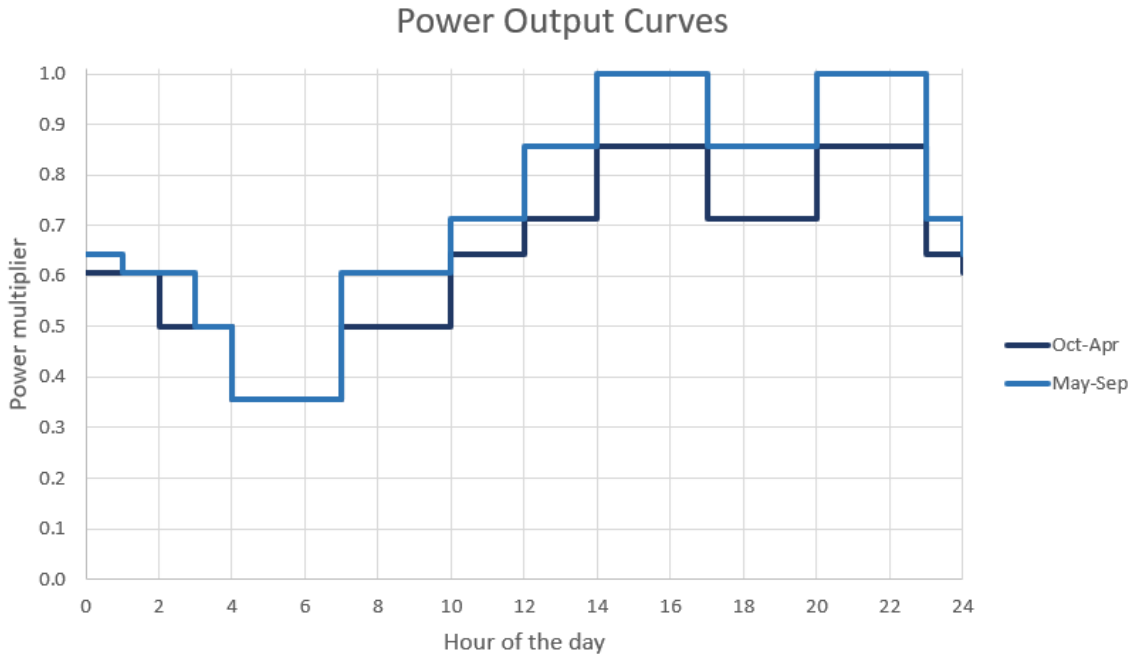

Figure 4.11: Power multiplier curves

4.11 Annual simulation

An annual simulation using the meteorological data from Crucero and the dispatch curves of Fig. 4.11 is carried out in order to gauge the effective efficiency of both the literature and the proposed cycle.

A simplified model is used to couple the solar field to the power block where molten salt mass flow data from SAM is supplied to a energy storage EES code, and that module provides the input heat required by the power block as a function of grid operator demand and ambient temperature. The heat supplied to the power block is expressed as a mass of molten salts and the storage of thermal energy is solved through the equivalent hot molten salt storage problem.

No dispatch strategy is implemented, the EES code follows the dispatch matrix whenever it can and in the case it cannot produce the demanded energy output it doesn't supply power to the grid. SAM preset values for CSP power plants are used. In order to secure the heat supply for the power block, a solar multiple of 4 is used along with a TES system with 12 hours of capacity. Due to the lack of information regarding the thermophysical properties of the mixture proposed by Mohan, the Solar salt properties are used instead as an approximation for said thermophysical properties.

4.11.1 Seasonal efficiencies

In order to quantify the performance of the cycles during the TMY both the seasonal first-law efficiencies and the seasonal second-law efficiencies of the cycles are obtained. The seasonal first-law efficiency is calculated through the following expression:

$$\eta_{season} = \frac{\sum_{i \in I} \eta_i \dot{W}_{net,i}}{\sum_{i \in I} \dot{W}_{net,i}} \tag{4.46}$$

where η_i is the cycle first-law efficiency at the hour i of the TMY and $\dot{W}_{net,i}$ is the net power output at hour i of the TMY.

Likewise the seasonal exergetic efficiency is calculated through the following expression:

$$\eta_{season,ex} = \frac{\sum_{i \in I} \eta_{ex,i} \dot{W}_{net,i}}{\sum_{i \in I} \dot{W}_{net,i}} \tag{4.47}$$

where η_i is the cycle second-law efficiency at the hour i of the TMY.

Chapter 5

Results & discussion

5.1 SNL test loop bench-marking

The following tables, Table 5.1 and Table 5.2 present specific cycle parameters chosen to assess how accurately the model proposed in the current work correlates to an actual s-CO_2 test loop. The first column declares the variable to contrast, the second column lists the magnitude reported in [18] or [13], the third column presents the results obtained from the EES model, the fourth column displays the percentage error and the fifth and last column states whether the second column magnitude was obtained directly from the aforementioned references, or if it was determined from the available information. If the last column says SNL, it means the magnitude was directly reported by the SNL, if it says Avg, it means it was averaged between the two turbines in the SNL test loop, finally, if the last column says Calc it means the magnitude was determined using the information reported in [18] and [13].

Figure 5.1: SNL RCBC testing platform [13]

Table 5.1: SNL comparison summary

Variable	SNL	EES	Err. [%]	Source
$\dot{Q}_{out}$ [kW]	455	498.4	9.538	SNL
$\dot{Q}_{in}$ [kW]	662	738.4	11.541	SNL
$\dot{Q}_{LTR}$ [kW]	515	542.7	5.379	SNL
$\dot{Q}_{HTR}$ [kW]	2202	2100	4.632	SNL
$\dot{W}_{comp}$ [kW]	47.8	50.45	5.544	SNL
$\dot{W}_{recomp}$ [kW]	85.1	79.59	6.475	SNL
$\dot{W}_{turb}$ [kW]	331.1	370	11.749	SNL
$\dot{W}_{net}$ [kW]	198.2	240	21.090	Calc
ΔP_{comp} [bar]	64.22	63.58	0.997	SNL
ΔP_{recomp} [bar]	62.89	61.96	1.479	SNL
ΔP_{turb} [bar]	52.95	58.18	9.877	Avg
ΔP_{LTR_C} [bar]	0.79	0.08972	88.643	Calc
ΔP_{LTR_H} [bar]	3.03	0.5643	81.376	Calc
ΔP_{HTR_C} [bar]	0.86	0.2516	70.744	Calc
ΔP_{HTR_H} [bar]	0.88	0.6989	20.580	Calc
PR_{comp} [-]	1.84	1.827	0.707	SNL
PR_{recomp} [-]	1.81	1.796	0.773	SNL
$PR_{turbine}$ [-]	1.64	1.736	6.144	Calc
η_{comp} [%]	67.3	66.36	1.397	SNL
η_{recomp} [%]	70.2	69.78	0.598	SNL
η_{turb} [%]	84.7	84.77	0.083	Avg
η_{cycle} [%]	29.9	32.5	8.552	Calc

where ΔP_{comp}, ΔP_{recomp} and ΔP_{turb} are the pressure rise/drop through the compressor, recompressor and turbine respectively, ΔP_{LTR_C}, ΔP_{LTR_H}, ΔP_{HTR_C} and ΔP_{HTR_H} are the pressure drops through the recuperator's LTR cold, LTR hot, HTR cold and HTR hot streams respectively, and finally, PR_{comp}, PR_{recomp} and PR_{turb} are the pressure ratios of the compressor, recompressor and turbine respectively.

Table 5.1 exhibits large percentage errors with the highest ones corresponding to the assessment of pressure drop through the recuperators. Following this errors is the cycle net power output with 21 percent. An important error of 11.7 percent is present in the turbine power output estimate and the cycle first-law efficiency is overestimated by 8.55 %.

As the model underestimates pressure drop through the test loop, it overestimates the pressure drop through the turbine. In a Brayton cycle, the first-law efficiency depends strongly on turbine power output, turbine power output in turn depends strongly on the enthalpy drop through the turbine and this enthalpy drop depends on the pressure differential perceived by the turbine. Therefore, the error in cycle net power output, turbine power output and cycle first-law efficiency all stem from the underestimation of pressure drop through the recuperators.

The following hypothesis is tested through Table 5.2: Can the errors encountered in Table

5.1 be explained by the incapability of the model to accurately account for pressure drop in the SNL test loop recuperators? In Table 5.2 the friction form losses coefficient f was scaled by a factor in order to match the data presented in [13]. Thus the error associated to the assessment of pressure drop in the recuperators is manually removed, and the performance of the model is isolated from this shortcoming.

Table 5.2: SNL comparison summary II

Variable	SNL	EES	Err. [%]	Source
$\dot{Q}_{out}$ [kW]	455	497	9.231	SNL
$\dot{Q}_{in}$ [kW]	662	699	5.589	SNL
$\dot{Q}_{LTR}$ [kW]	515	529.5	2.816	SNL
$\dot{Q}_{HTR}$ [kW]	2202	2154	2.180	SNL
$\dot{W}_{comp}$ [kW]	47.8	50.45	5.544	SNL
$\dot{W}_{recomp}$ [kW]	85.1	79.65	6.404	SNL
$\dot{W}_{turb}$ [kW]	331.1	332.1	0.302	SNL
$\dot{W}_{net}$ [kW]	198.2	202	1.917	Calc
ΔP_{comp} [bar]	64.22	63.58	0.997	SNL
ΔP_{recomp} [bar]	62.89	62.18	1.129	SNL
ΔP_{turb} [bar]	52.95	52.96	0.019	Avg
ΔP_{LTR_C} [bar]	0.79	0.79	0.000	Calc
ΔP_{LTR_H} [bar]	3.03	3.03	0.000	Calc
ΔP_{HTR_C} [bar]	0.86	0.86	0.000	Calc
ΔP_{HTR_H} [bar]	0.88	0.88	0.000	Calc
PR_{comp} [-]	1.84	1.827	0.707	SNL
PR_{recomp} [-]	1.81	1.799	0.608	SNL
$PR_{turbine}$ [-]	1.64	1.636	0.030	Calc
η_{comp} [%]	67.3	66.36	1.397	SNL
η_{recomp} [%]	70.2	69.77	0.613	SNL
η_{turb} [%]	84.7	84.81	0.130	Avg
η_{cycle} [%]	29.9	28.9	3.472	Calc

The percentage errors diminished considerably, with the previous errors of 21.090, 11.749 and 8.552 % now at 1.917, 0.302 and 3.472 %. This proves the hypothesis.

Besides the Petukhov correlation [29], the Blasius correlation [38] and both empirical correlation cited in [37] where implemented, nevertheless, the error percentages where greater. One possible explanation is that relative surface roughness in PCHEs plays an important role in pressure drop and the tested correlations did not account for said effects. As shown in Fig. 5.2, the friction factor has an important dependence on relative roughness. Whilst surface roughness in a PCHE might not be substantial ($\varepsilon \sim 1{\times}10^{-6}$ [m] [41]) considering the small hydraulic diameter of PCHEs, the relative roughness might contribute significantly towards the friction factor.

On the other hand, the data provided by Sandia is experimental data and as such it is subject to all the inconveniences that it's nature entails. Fig. 5.1 shows all the piping and bends in the piping that are not considered in the model, nor declared in [18] or [13]. Therefore

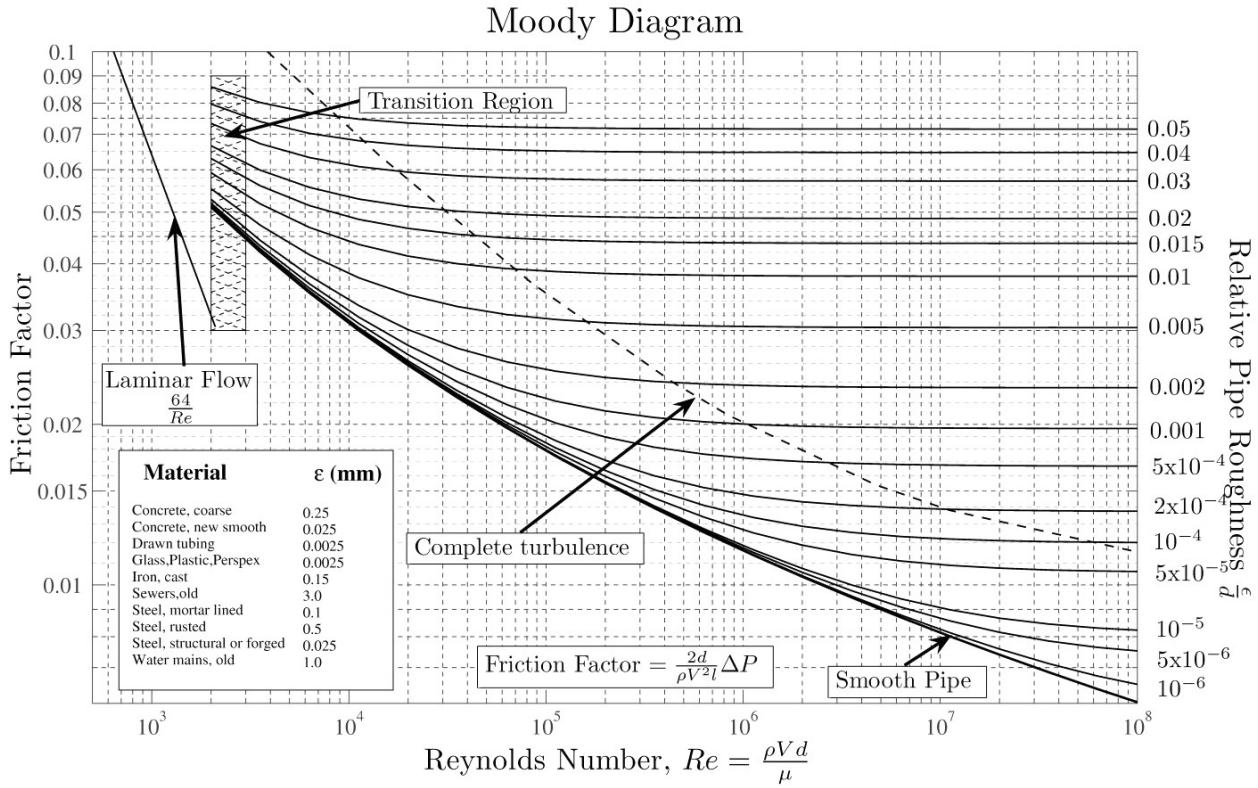

Figure 5.2: Moody diagram [42]

a possible source of error are form losses due to piping and piping bends. Another possible explanation are instrumentation issues. In particular, the pressure drop through the hot side of the LTR stands out with a magnitude of 3.03 [bar], this is considerable and whether such a pressure drop is due to piping or instrumentation issues is outside of the author's knowledge. In Test facilities [13] Clementoni states that leaks are an important problem on the SNL test loop. Mass loss throughout the test loop further hinder the capability of the model to accurately describe the operation of the cycle.

5.2 Cycle design

The power cycle designed provides a net power output of 25 [MW] with a s-CO_2 mass flow of 255 [kgs^{-1}] and 224.6 [kgs^{-1}] for molten salts in the PHX at the design ambient temperature of 20.8 [°C]. Table 5.3 presents the pressures, temperatures, enthalpies and entropies for the s-CO_2 at each point of the cycle, as numbered in Fig. 4.4. The cycle is designed so the compressor's outlet pressure is such that after the LTR pressure drop, the compressor and recompressor streams meet at the mix chamber with the same pressure of 200.227 [bar]. This pressure in turn is designed so the pressure drop in the HTR and PHX result in a pressure at the turbine's inlet of 200 [bar] (200.020 [bar] to be precise). The magnitude of the works and heat flows in the cycle is presented in graphic format in Fig. 5.3. Table 5.4 lists the main dimensions and parameters that make up the power cycle.

Table 5.3: Cycle pressure, temperature, enthalpy and entropy under design conditions

State	Pressure [bar]	Temperature [°C]	Enthalpy [$kJkg^{-1}$]	Entropy [$kJkg^{-1}K^{-1}$]
1	90.000	35.80	-202.928	-1.407
2	200.277	58.89	-185.118	-1.401
3	200.254	134.25	-10.676	-0.9248
4	200.227	129.94	-18.509	-0.9441
5	200.227	131.22	-16.156	-0.9383
6	200.100	486.59	449.974	-0.09712
7	200.020	650.00	653.311	0.1453
8	90.789	544.29	530.044	0.1565
9	90.352	145.01	63.910	-0.6244
10	90.100	65.15	-52.716	-0.9362

Figure 5.3: Work and Heat under design conditions

Table 5.4: Cycle dimensions and parameters under design conditions

Variable	Unit	Magnitude
D_{comp}	[m]	0.2245
D_{recomp}	[m]	0.2027
D_{turb}	[m]	0.4637
$N_{comp,design}$	[revmin^{-1}]	15760
$N_{recomp,design}$	[revmin^{-1}]	26817
$N_{turb,design}$	[revmin^{-1}]	15760
$\eta_{comp,design}$	[-]	0.89
$\eta_{recomp,design}$	[-]	0.89
$\eta_{turb,design}$	[-]	0.93
ΔP_{comp}	[bar]	110.3
ΔP_{recomp}	[bar]	110.2
ΔP_{turb}	[bar]	109.2
A_{LTR}	[m^2]	3393
A_{HTR}	[m^2]	2962
$N_{channelpairs,LTR}$	[-]	550000
$N_{channelpairs,HTR}$	[-]	600000
L_{LTR}	[m]	1.5
L_{HTR}	[m]	1.2
a_{LTR}	[mm]	0.8
b_{LTR}	[mm]	0.8
a_{HTR}	[mm]	0.8
b_{HTR}	[mm]	0.8
$D_{h,LTR}$	[mm]	0.9776
$D_{h,HTR}$	[mm]	0.9776
ΔP_{LTR_C}	[bar]	0.05013
ΔP_{LTR_H}	[bar]	0.2523
ΔP_{HTR_C}	[bar]	0.1265
ΔP_{HTR_H}	[bar]	0.4366
ΔP_{Cooler}	[bar]	0.1
ΔP_{PHX}	[bar]	0.08
P_{high}	[bar]	200
P_{low}	[bar]	90
T_{high}	[°C]	650
T_{low}	[°C]	35.8
$\dot{Q}_{LTR}$	[MW]	29.740
$\dot{Q}_{HTR}$	[MW]	118.864
$\dot{Q}_{in}$	[MW]	51.851
$\dot{Q}_{out}$	[MW]	26.813
$\dot{W}_{comp}$	[MW]	3.179
$\dot{W}_{recomp}$	[MW]	3.216
$\dot{W}_{turb}$	[MW]	31.433
ϕ	[-]	0.3
$\dot{m}$	[kgs^{-1}]	255
$\dot{m}_{salt}$	[kgs^{-1}]	224.6
$\dot{W}_{net}$	[MW]	25
η_{cycle}	[-]	0.483

5.3 Literature cycle

5.3.1 Operational range

The following figures present the operational range of the literature cycle under different M out of N operation regimes as shaded regions. The x-coordinate corresponds to ambient temperature (in [°C]) and the y-coordinate corresponds to the percentage of the design net power output (25 [MW]) the power plant is operating at.

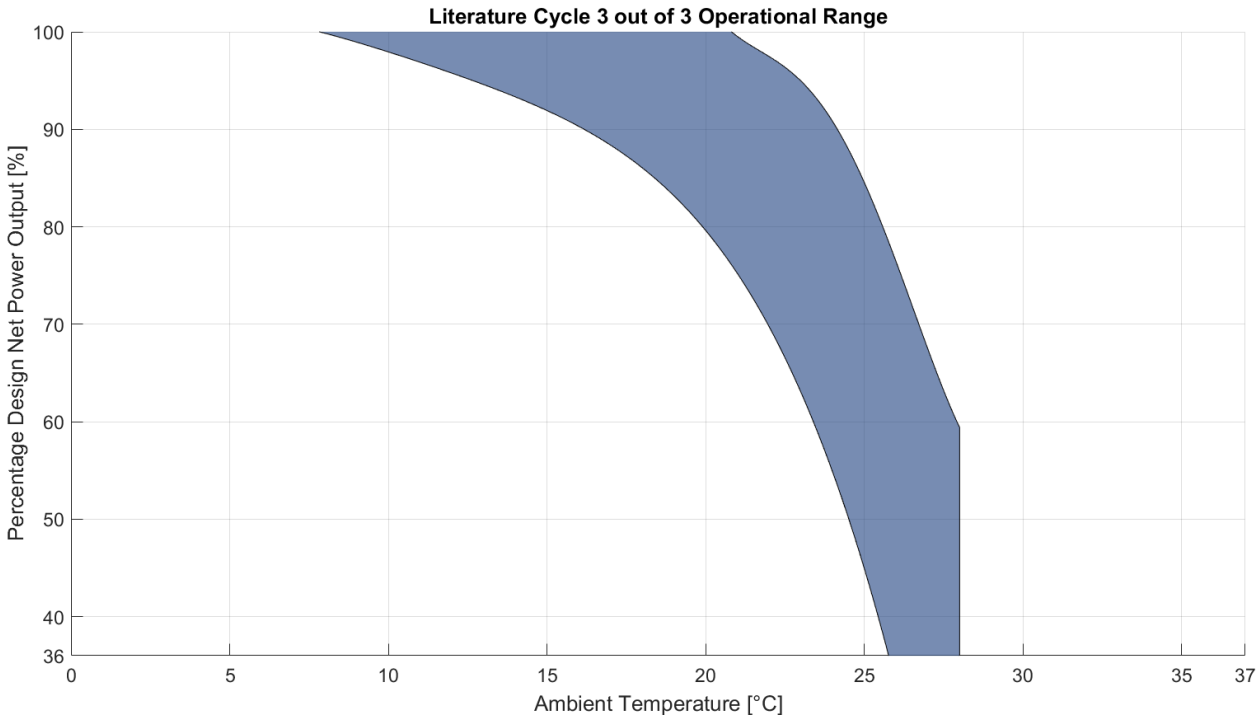

Figure 5.4: Operational range for the literature cycle with 3 out of 3 compressors functioning

As seen in Fig. 5.4, the operational range for the literature cycle is highly restricted. Out of the whole domain of interest (0 - 37 [°C] and 25 - 9 [MW]) the literature cycle can only operate on a thin crescent. The operational range is determined by three curves. The curve that dictates the bottom-left end of the operational domain corresponds to the compressors undergoing surge.

As power output is modulated through a decrease in working fluid mass flow, the compressors rapidly undergo surge due to the proximity of the design operational conditions to the surge line (as can be seen in Fig. 3.6). As ambient temperature increases beyond the design point, the working fluid's specific volume increases, therefore the decrease in mass flow required to turn-down power output is partially offset by the increase in specific volumetric flow, delaying the onset of surge in the compressors and extending the operational range downwards. On the contrary, as ambient temperature drops the decrease in volumetric flow causes the compressor to undergo surge even sooner. Even when operating with the design mass flow of 255 [kgs^{-1}] the change in s-CO_2 density is so stark that the literature cycle can't operate at ambient temperatures below 7 [°C].

The right-hand side of the operational domain is clearly defined by two different lines. The bottom one, at an ambient temperature of 28 [°C] corresponds to the limit at which flow in the compressors becomes supersonic. At higher ambient temperatures, turbine pressure differential must be higher in order to achieve the same mass flow rate. This higher pressure differential can be achieved to certain extent by spinning the compressors faster, but only so much as eventually compressor rotor tip speed will reach Mach 1 with all the undesirable consequences it brings about.

The final edge of the operational domain, the top-right, corresponds to a new phenomena (to the author's knowledge). In order to operate on the top right corner the compressor needs to spin faster whilst the turbine needs to spin slower. As these components share a shaft on the literature cycle there is in a sense a blockage due to the shaft's mechanical integrity. Henceforth this phenomena shall be referred to as shaft-blockage. It should be noted that shaft-blockage has nothing to do with choking or supersonic flow regimes.

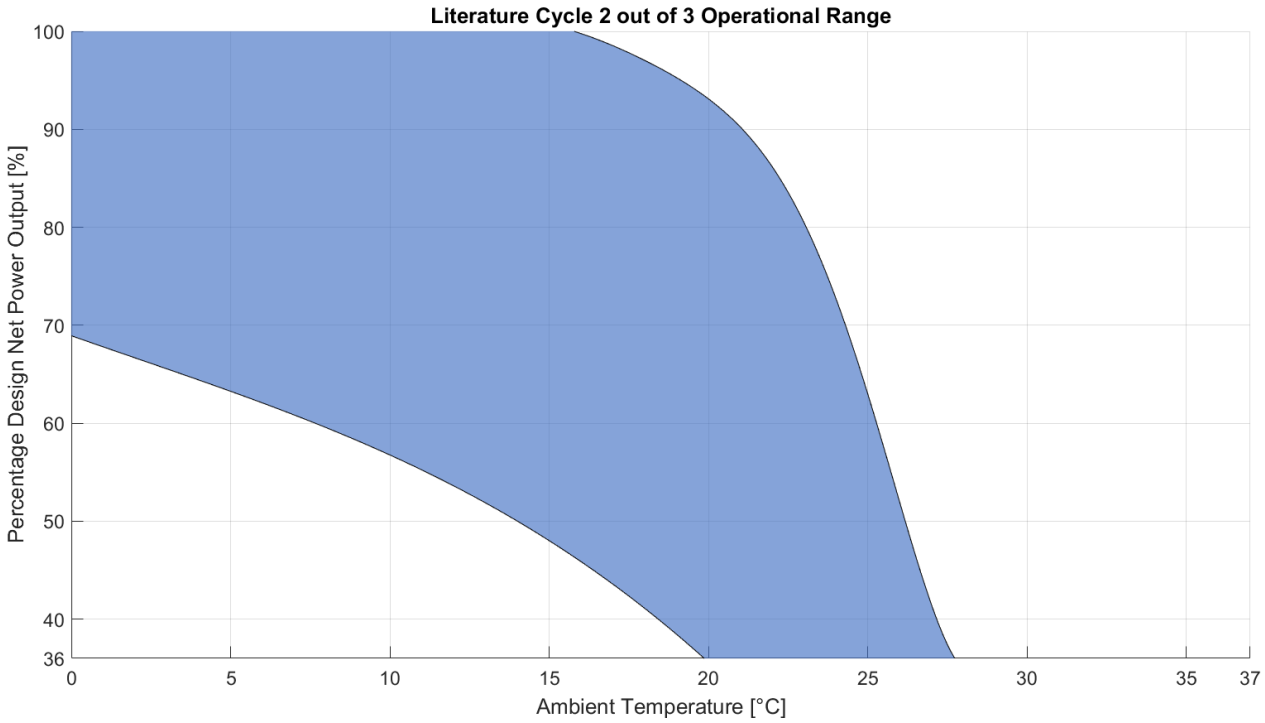

Figure 5.5: Operational range for the literature cycle with 2 out of 3 compressors functioning

When the literature cycle operates with two out of it's three compressors (and three out of the three recompressors) the operational domain widens and shifts towards the lower left-hand side corner, as seen in Fig. 5.5. The surge limitation persists yet distributing the mass flow between less compressors delays the onset of surge and enables the cycle to operate at an ambient temperature of 0 [°C].

The right-hand side edge of the operational domain corresponds to the previously mentioned shaft-blockage phenomena. The increased mass flow the compressors perceive when one of them is turned off decreases the pressure rise through them. In order to provide the pressure differential required by the turbine a decrease in volumetric flow, due to a decrease in ambient temperature is required. Therefore, the shaft-blockage curve shifts to the left

when compared to the previous case.

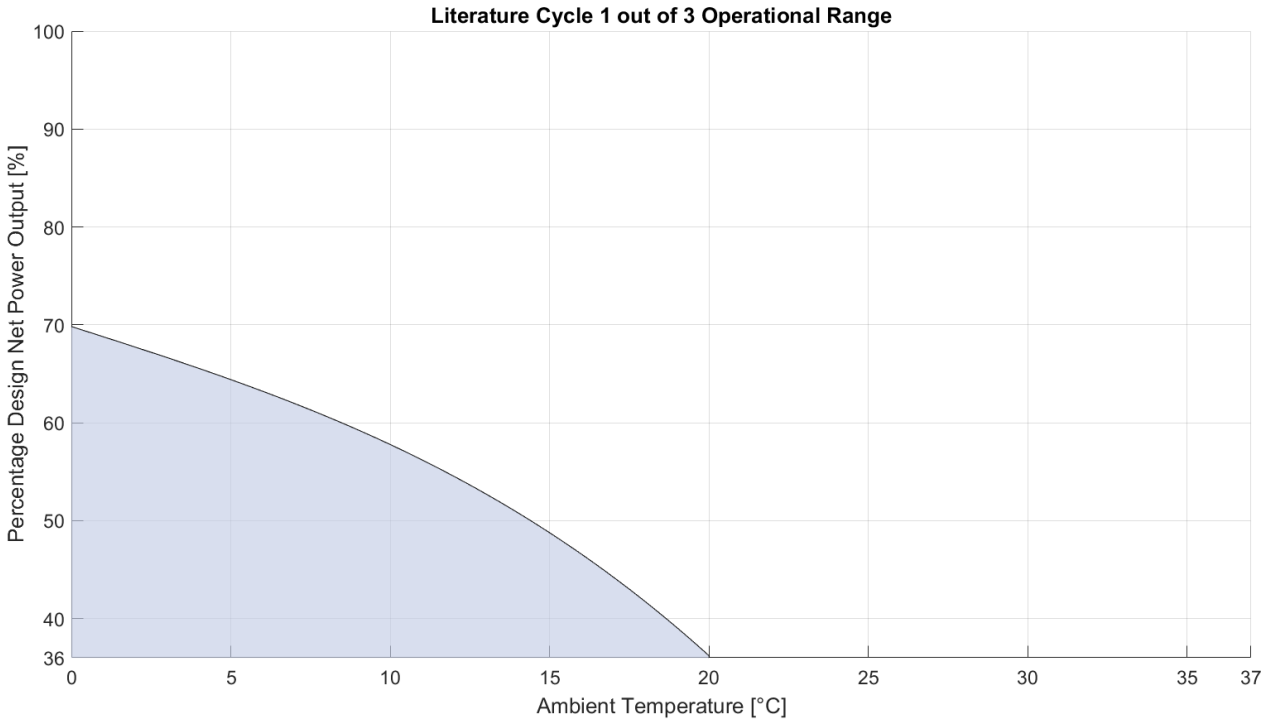

Figure 5.6: Operational range for the literature cycle with 1 out of 3 compressors functioning

The surge limitation persist for the one out of three compressors scenario. However as our domain of interest does not encompass power outputs smaller than 9 [MW] it disappears as a domain edge for the last scenario, as seen in Fig. 5.5. The upper-right curve corresponds to the shaft-blockage phenomena, in a manner analogous to that examined in the previous configuration.

When the three operational ranges are superposed, an extended operational range is formed. Fig. 5.7 showcases the overlap of the previous domains. The extended range is substantially larger than that available to the literature cycle if the M out of N system wasn't implemented. Regardless, the literature cycle can't operate at ambient temperatures above 28 [°C]. There is a slight overlap between the third and second configuration, thus the operational domain is continuous, however, the need to change between operating regimes on such a narrow band is challenging.

Finally, the previous figures testify to how limited the operational range of the literature cycle is. Previous works did not check if the cycle was able to operate outside of the design conditions and thus many results are built on unfeasible operational conditions (sonic flow, surge, shaft-blockage).

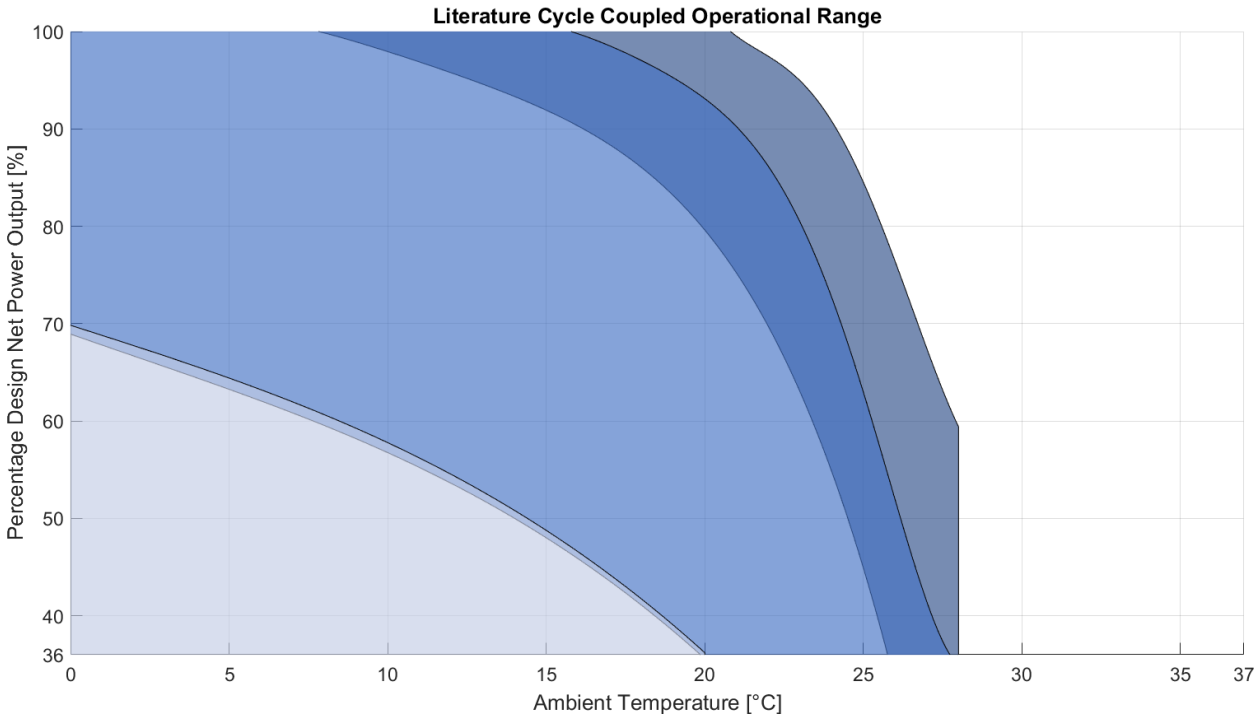

Figure 5.7: Coupled operational range for the literature cycle

5.3.2 Cycle first-law efficiency

Combining the three previous configurations, the coupled first-law efficiency of the literature cycle was assessed. Fig. 5.8 shows an isometric view of the three distinct surfaces that comprise the combined operational range of the literature cycle. Cycle first-law efficiency has it's maximum of 48.3 % at design conditions, under off-design conditions it goes as low as 28 %, as seen in the bottom left corner of Fig. 5.15.

The contour plot of Fig. 5.10 shows how the first-law efficiency decreases slowly as ambient temperature decreases and faster as power output is reduced (reduced mass flow rate). The discontinuities between the surfaces seen in Fig. 5.8 imply a continuous change in the power block's net power output would require a discrete change in cycle supplied heat when crossing between configurations. By the same token, when crossing the border between configurations at a constant mass flow rate there is a discontinuous jump in net power output. This brings about important control ramifications.

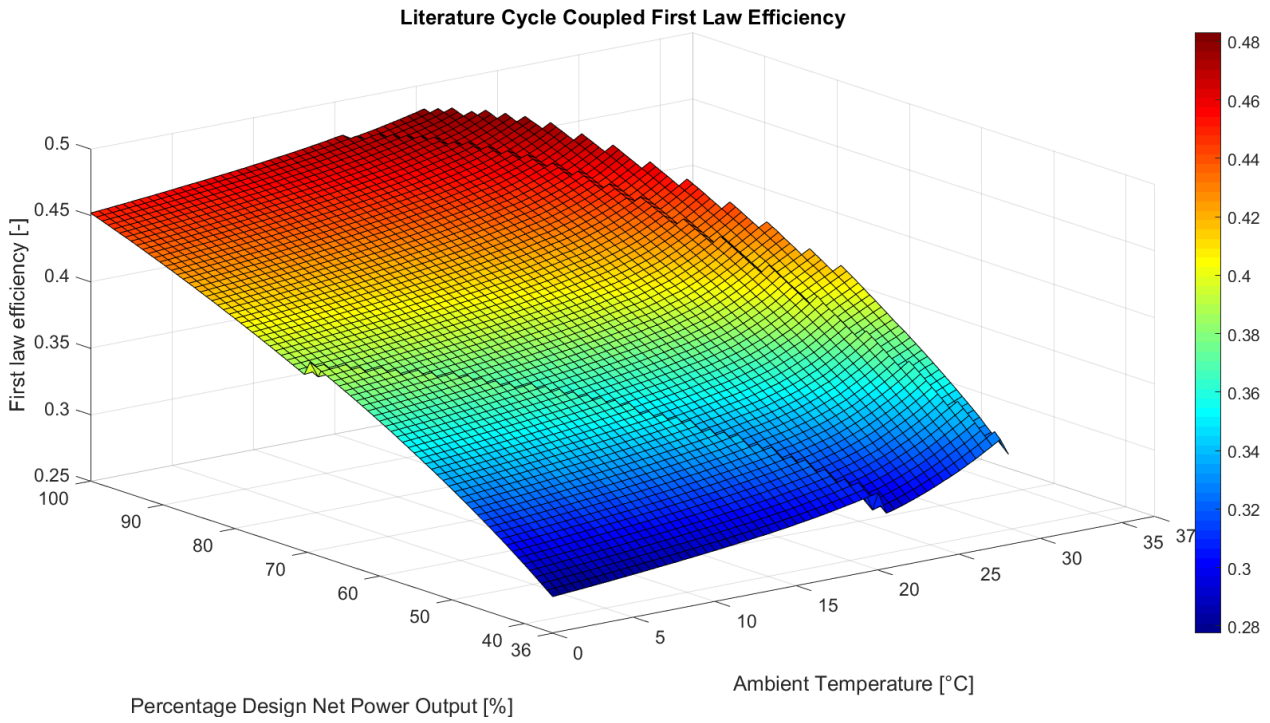

Figure 5.8: Isometric view of literature cycle efficiency as a function of percentage design power output and ambient temperature

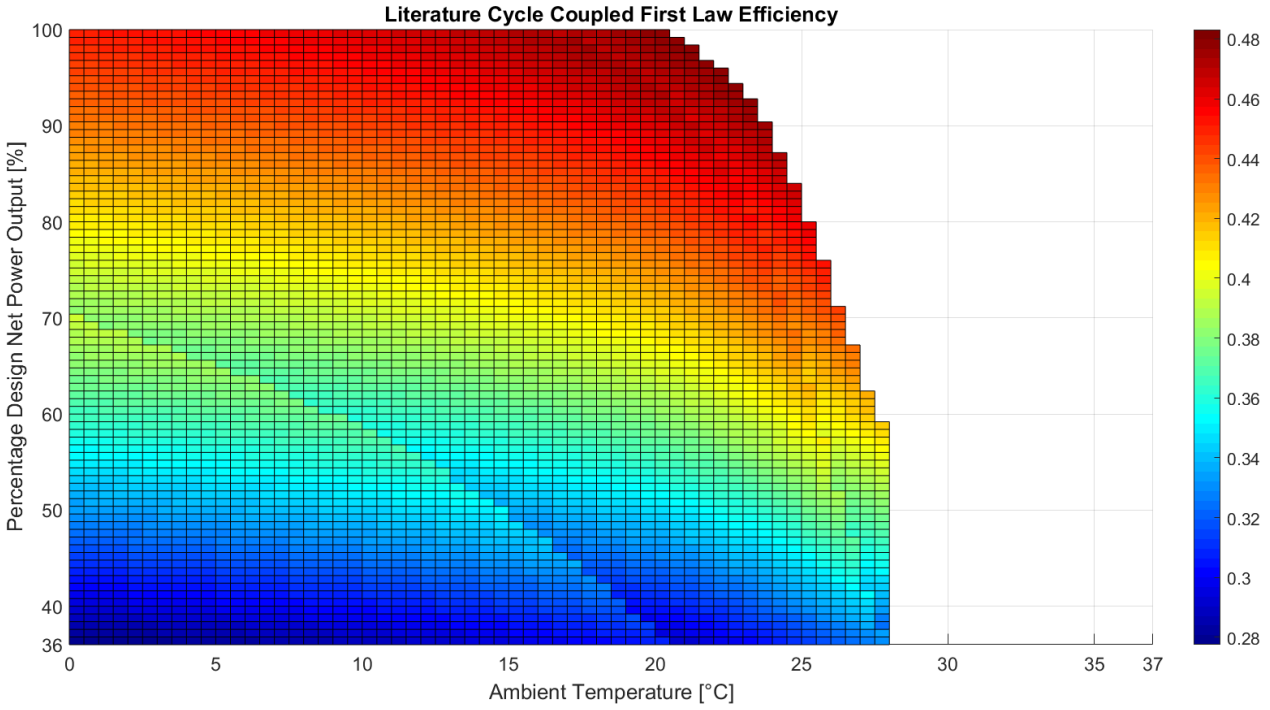

Figure 5.9: Top-down view of literature cycle efficiency as a function of percentage design power output and ambient temperature

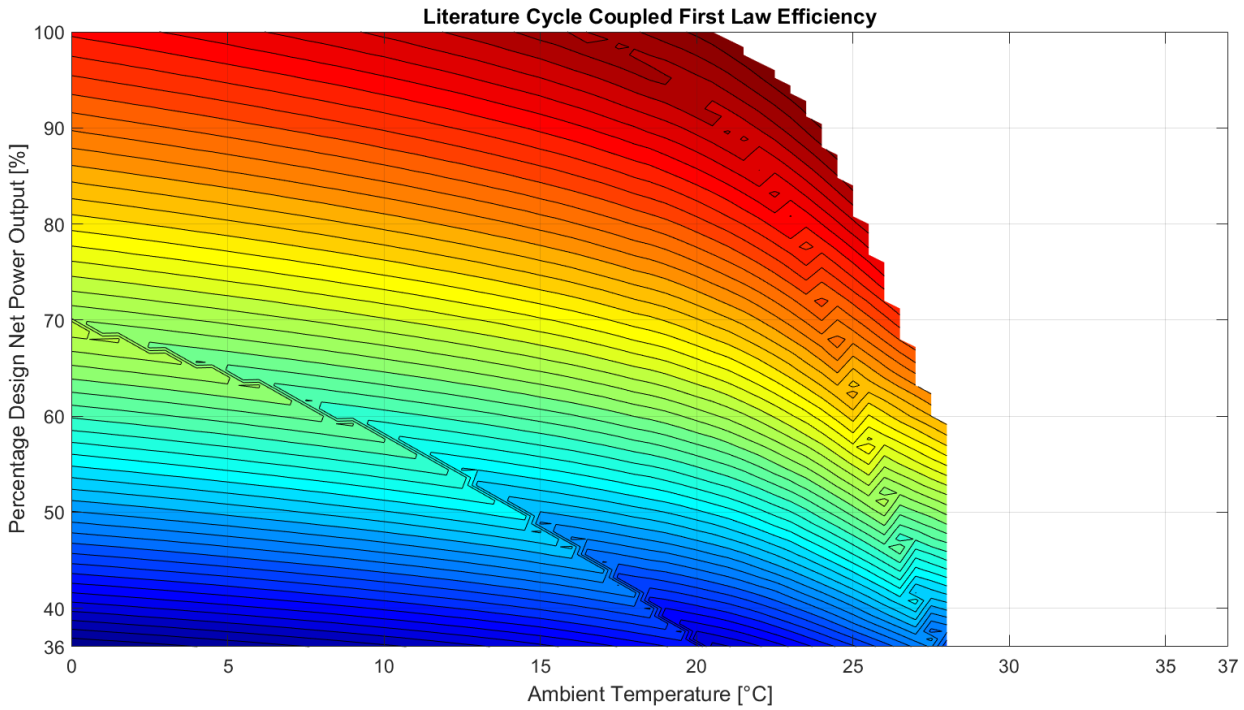

Figure 5.10: Contour representation of literature cycle efficiency as a function of percentage design power output and ambient temperature

5.4 Proposed cycle

5.4.1 Operational range

The following figures present the operational range of the proposed cycle under different M out of N operation regimes as shaded regions.

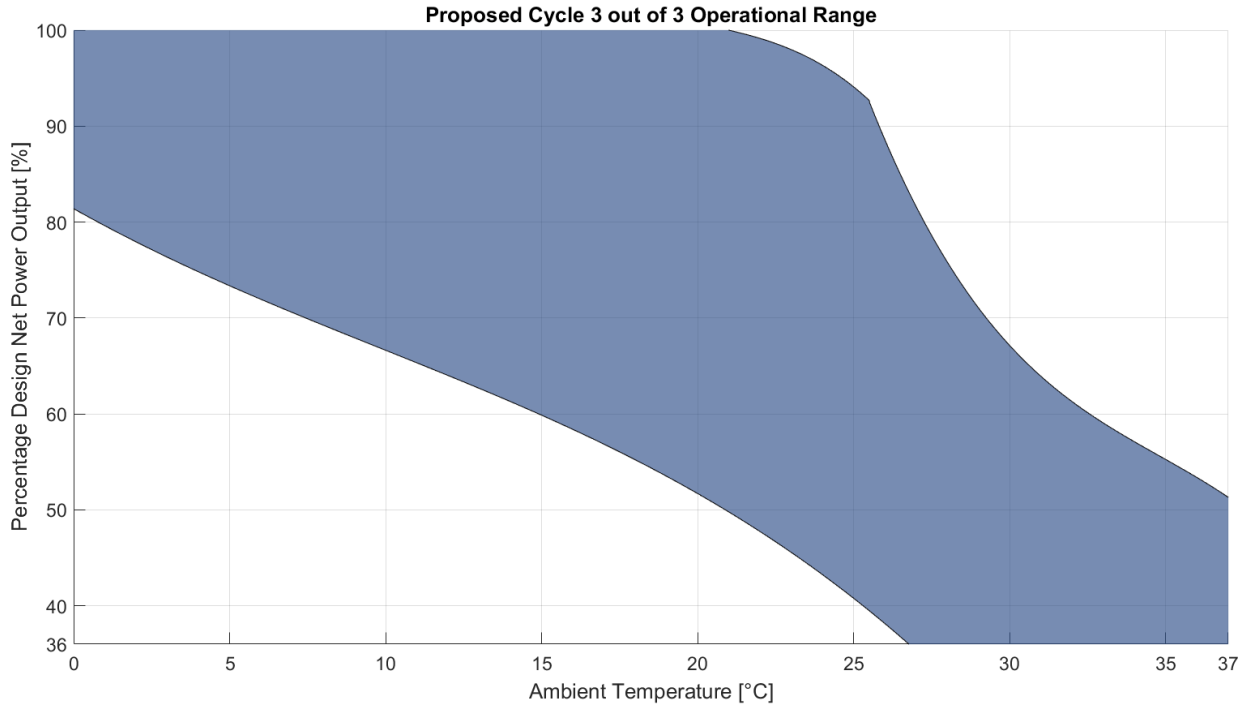

Figure 5.11: Operational range for the proposed cycle with 3 out of 3 compressors functioning

Figure 5.11 presents the wide domain in which the proposed cycle can operate with three out of it's three compressors on. The edge of the operational range is comprised of three curves, one to the bottom left-hand side and the other two at the right end of the operational range. When compared with the range available to the literature cycle, the greater flexibility a third shaft grants to the cycle is evident.

As with Fig. 5.4, the bottom left edge corresponds to the compressors undergoing surge. As neither the compressor nor the recompressor share a shaft with the turbine, they can adjust their shaft speeds and delay the onset of surge.

The right hand side has a short curve at the top where the limiting factor is mass flow. At the maximum mass flow of 255 [kgs^{-1}], as ambient temperature increases the cycle's net power output decreases. At higher ambient temperatures the operational range is delimited by the onset of supersonic flow. As before, with greater ambient temperatures the pressure differential required to sustain a certain mass flow rate increase, eventually this greater speeds make the compressors enter a supersonic flow regime.

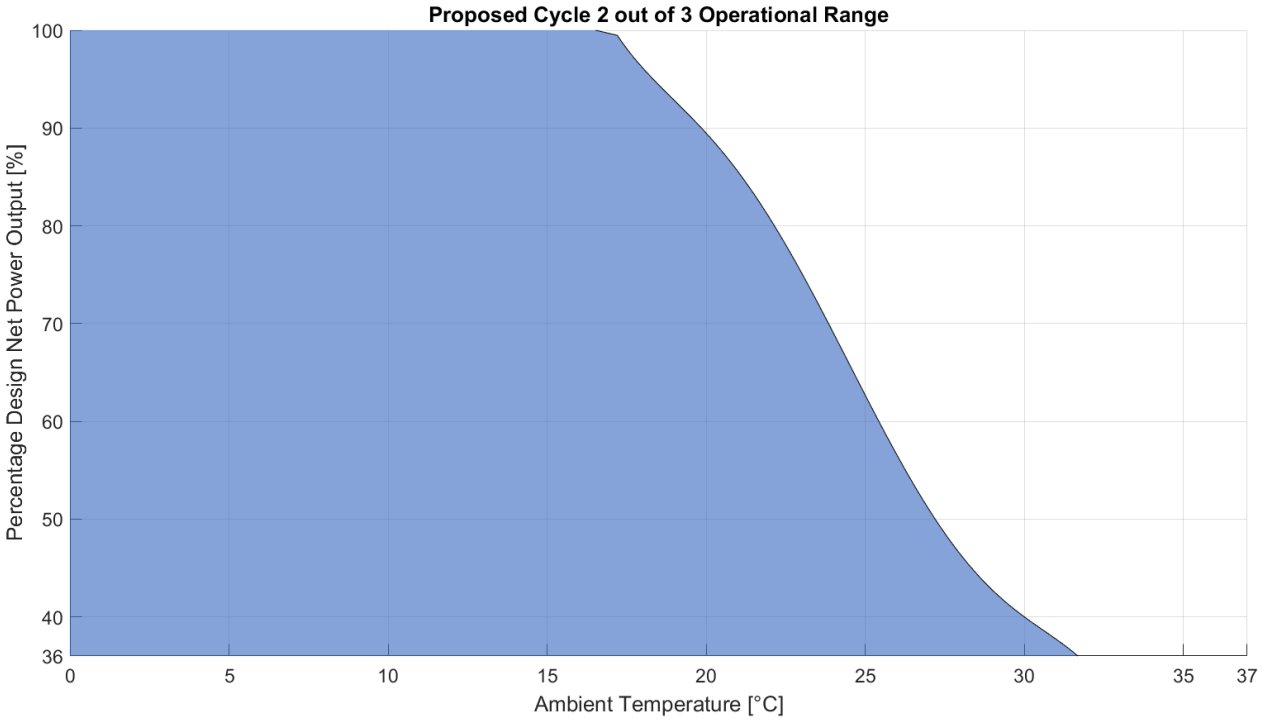

Figure 5.12: Operational range for the proposed cycle with 2 out of 3 compressors functioning

Figure 5.12 presents a similar situation to Fig. 5.6, the operational range exceeds the domain of interest on the left side of the graph. The edge of the operational domain to the right is composed by an extremely short curve up top, associated to the maximum mass flow constraint and a long curve representing the onset of supersonic flow. Analogously to Fig. 5.5, with one of the compressors off the other two receive a greater mass flow. This reduces the pressure rise and in order to sustain the required mass flow through the turbine, the compressor must spin faster, giving rise to supersonic flow. Therefore the right-hand limit of the operational range shifts to the left.

Due to the extensive range of the proposed cycle under a two out of three configuration, there is no need to study the one out of three configuration.

Superposing both operational ranges results is the coupled operational range for the proposed cycle as seen in Fig. 5.13. The proposed cycle is able to provide power with an ambient temperature of 37 [°C], albeit at little more than 50 % of the design net power output. The overlap between the operational regions is significant.

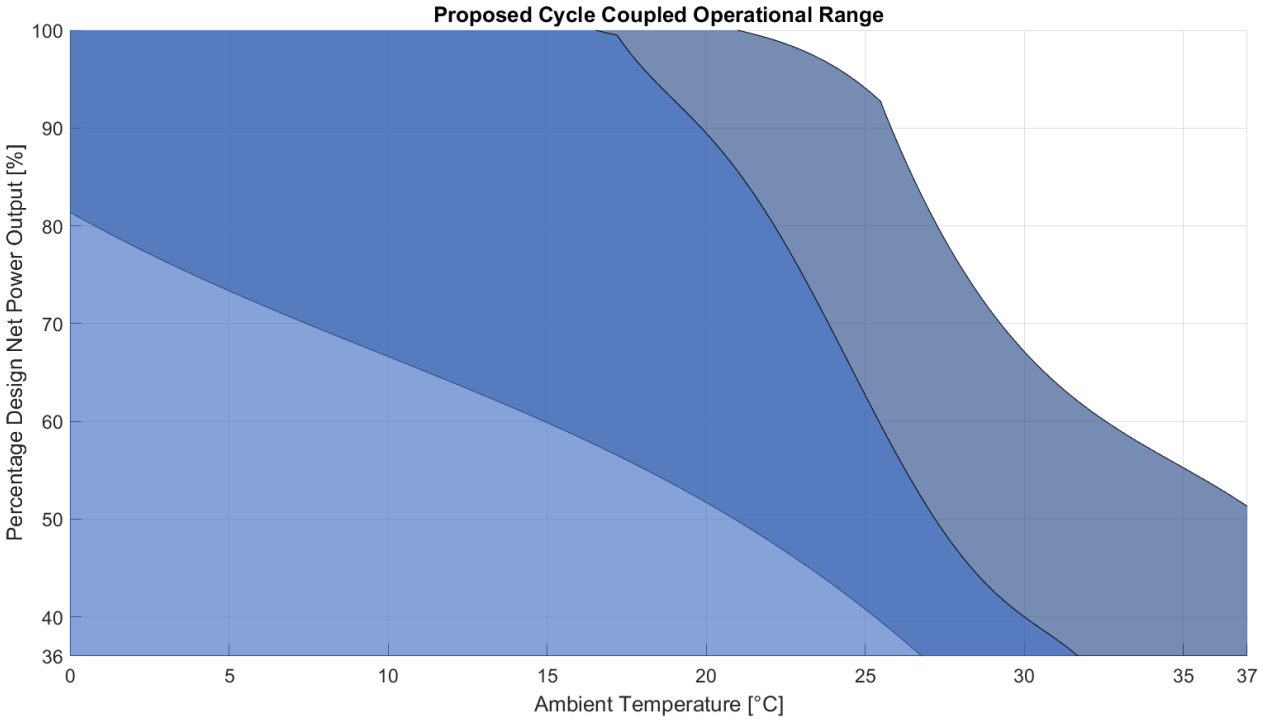

Figure 5.13: Coupled operational range for the proposed cycle

5.4.2 Cycle first-law efficiency

Figure 5.14 presents the isometric view of the combined surfaces that make up the combined operational range of the proposed cycle.

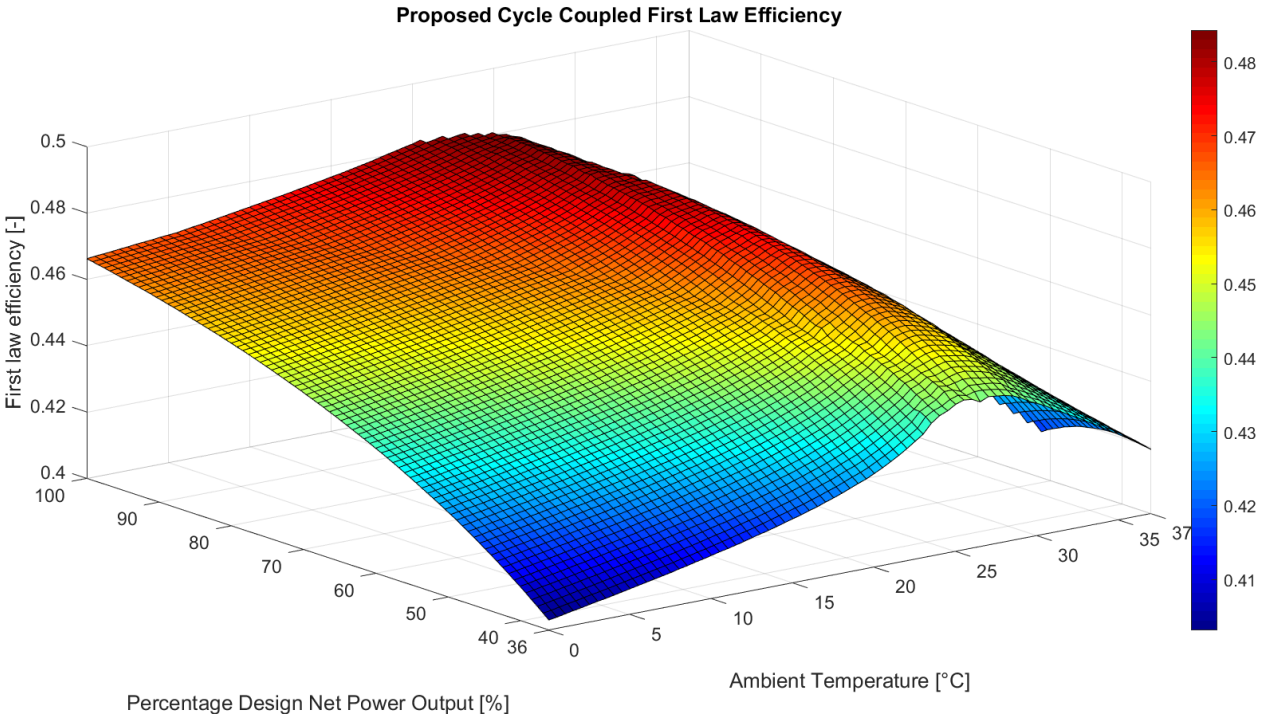

Figure 5.14: Isometric view of proposed cycle efficiency as a function of percentage design power output and ambient temperature

The proposed cycle's lowest first-law efficiency is above 40%. When compared to the literature cycle's 28 % the proposed cycle far exceeds it in terms of performance.

Unlike the discontinuities found in the coupled efficiency of the literature cycle, the transition between configurations in the proposed cycle is smooth, eliminating the aforementioned control complications.

Figure 5.16 presents how cycle first-law efficiency varies strongly with net power output, but it varies slower when the ambient temperature is close to 27 [°C]. As with the literature cycle, the first-law efficiency varies less with respect to ambient temperature, as ambient temperature decreases.

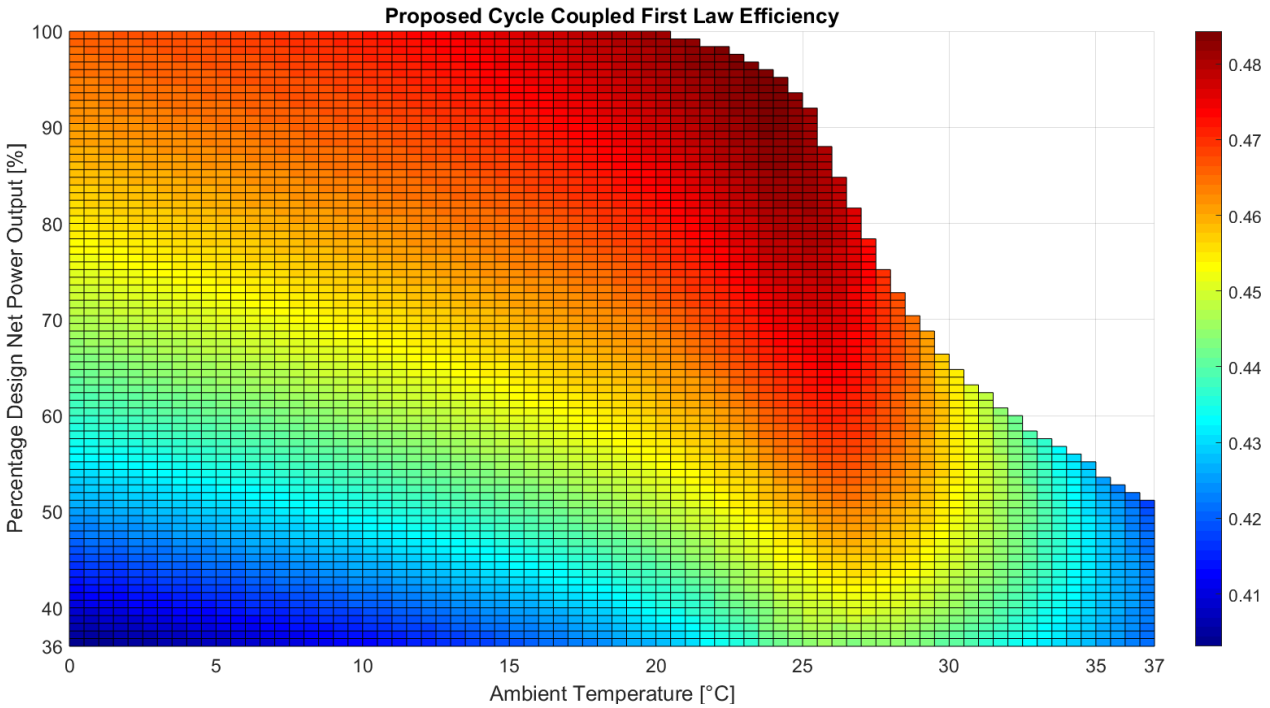

Figure 5.15: Top-down view of proposed cycle efficiency as a function of percentage design power output and ambient temperature

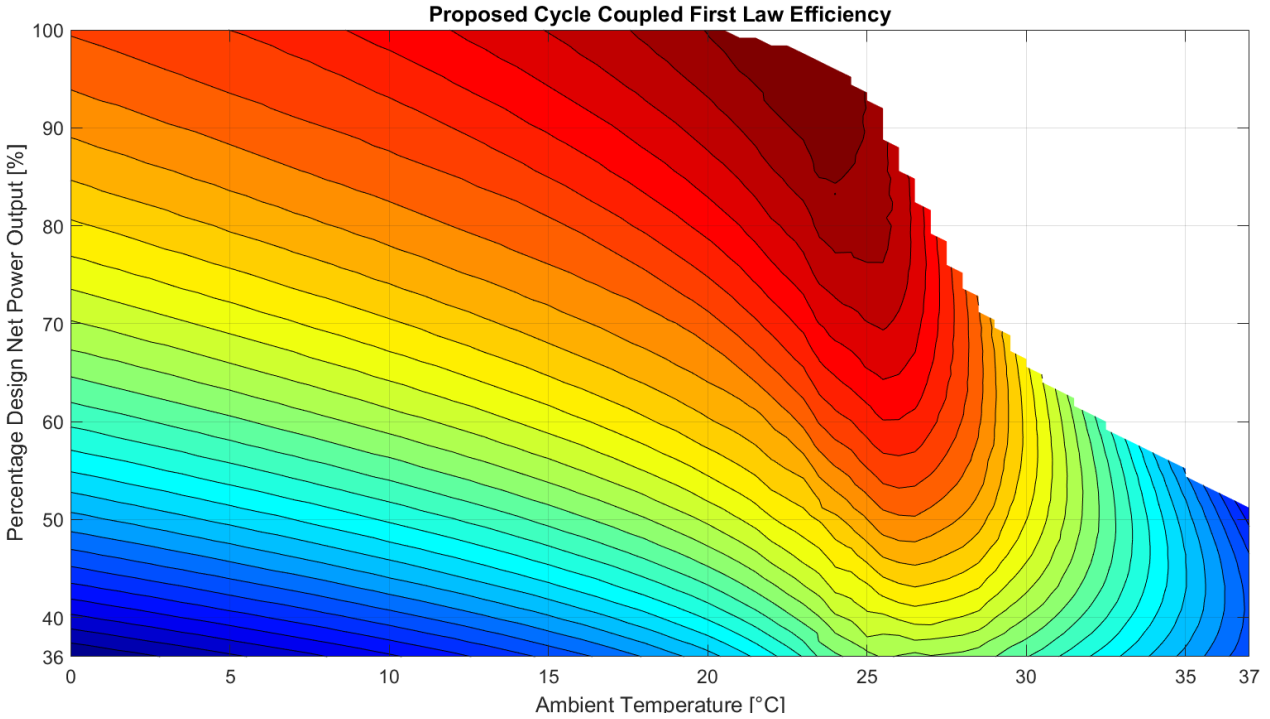

Figure 5.16: Contour representation of proposed cycle efficiency as a function of percentage design power output and ambient temperature

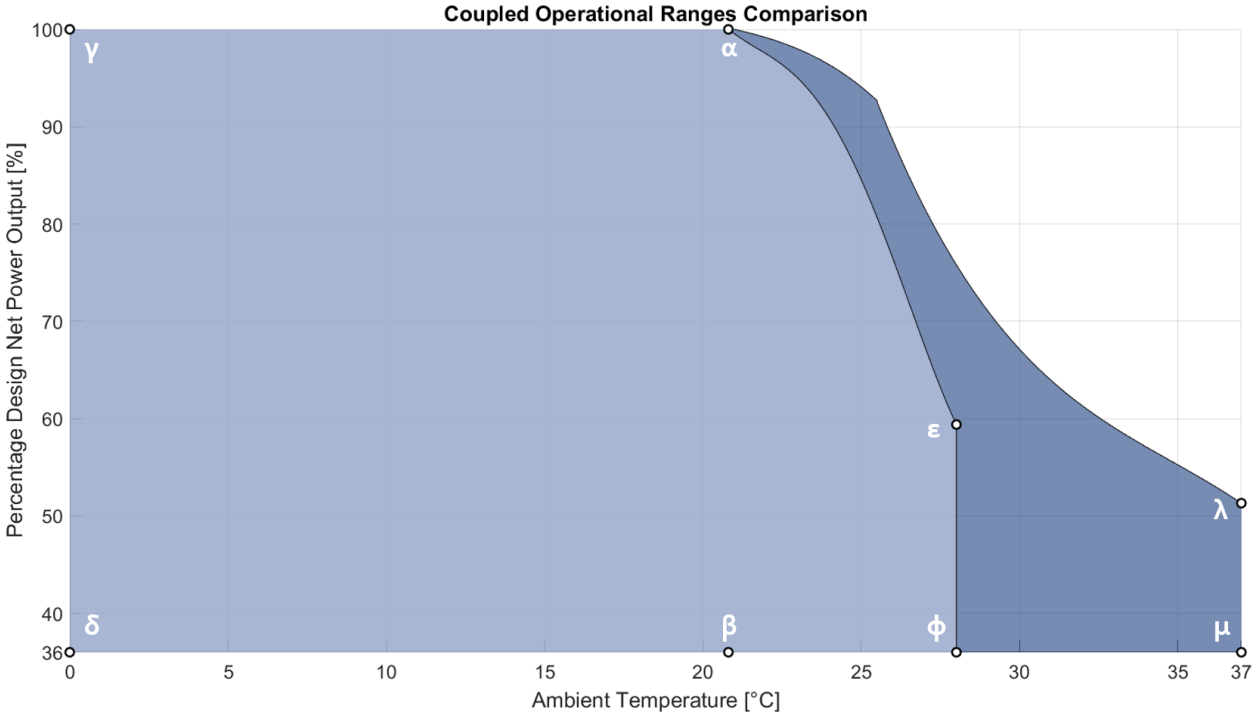

Figure 5.17: Coupled operational ranges comparison & key points

Figure 5.17 shows the combined operational range of the literature and proposed cycle. Certain points are signalled and named with Greek letters, these key points are chosen to further examine the performance of both the literature and the proposed cycle.

5.5 Exergetic analysis

The following section analyses the performance of the cycle by component, at the key points shown in Fig.5.17. The nominal state T-s diagram is plotted along with the CO_2 saturation bell in order to better appraise how changes in ambient temperature and cycle net power output alter the cycle's performance, through the T-s diagram.

The irreversibilities in the cycle are quantified through the assessment of exergy destruction. These are presented in Figures 5.29, 5.30 and 5.31.

5.5.1 T-s diagrams

Figure 5.18 presents the T-s diagram of the cycle under nominal operational conditions, this is identical for both the literature and the proposed cycle. The coolest point in the cycle is very near the critical point, but since the LTR exit (where the flow is split) is further to the right the effects of the critical point aren't as dire. Due to how the model discretises the recuperators, the HTR part of the diagram does not have as much points as the LTR, explaining the sharp straight segments found in that section of the diagram. Likewise, after the flow is split there is only the coordinate corresponding to the Cooler's outlet, causing the straight line at the bottom-left part of the graph.

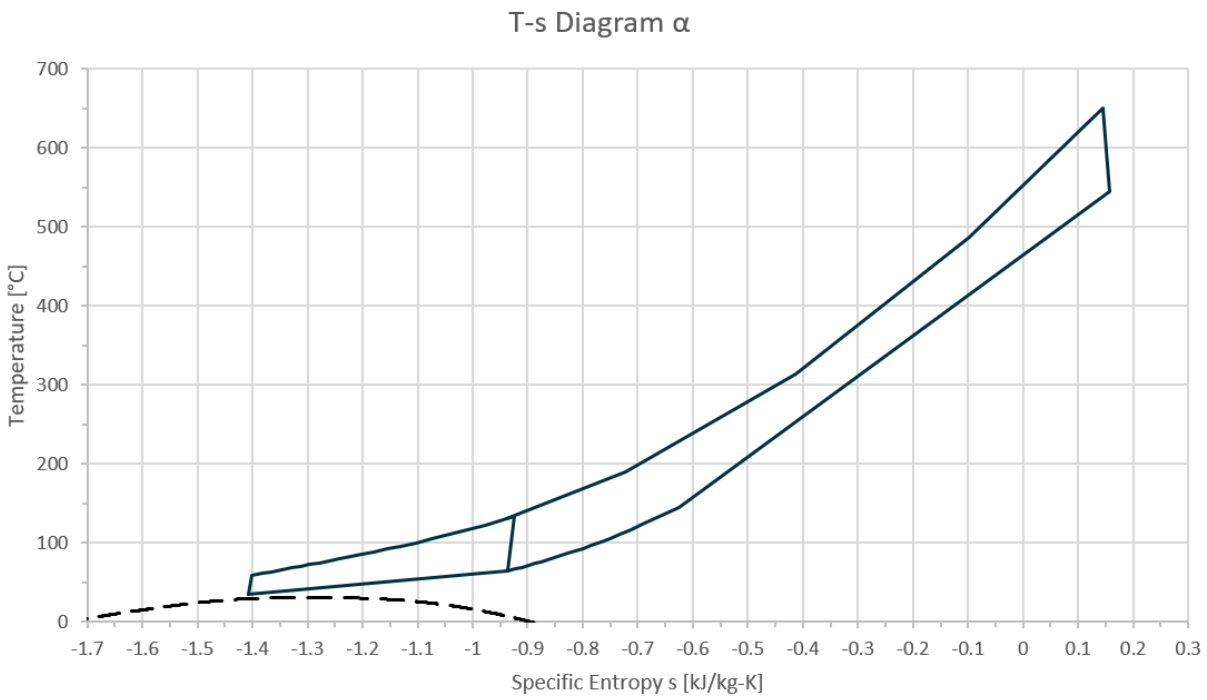

Figure 5.18: Cycle T-s diagram at α with CO_2 saturation bell

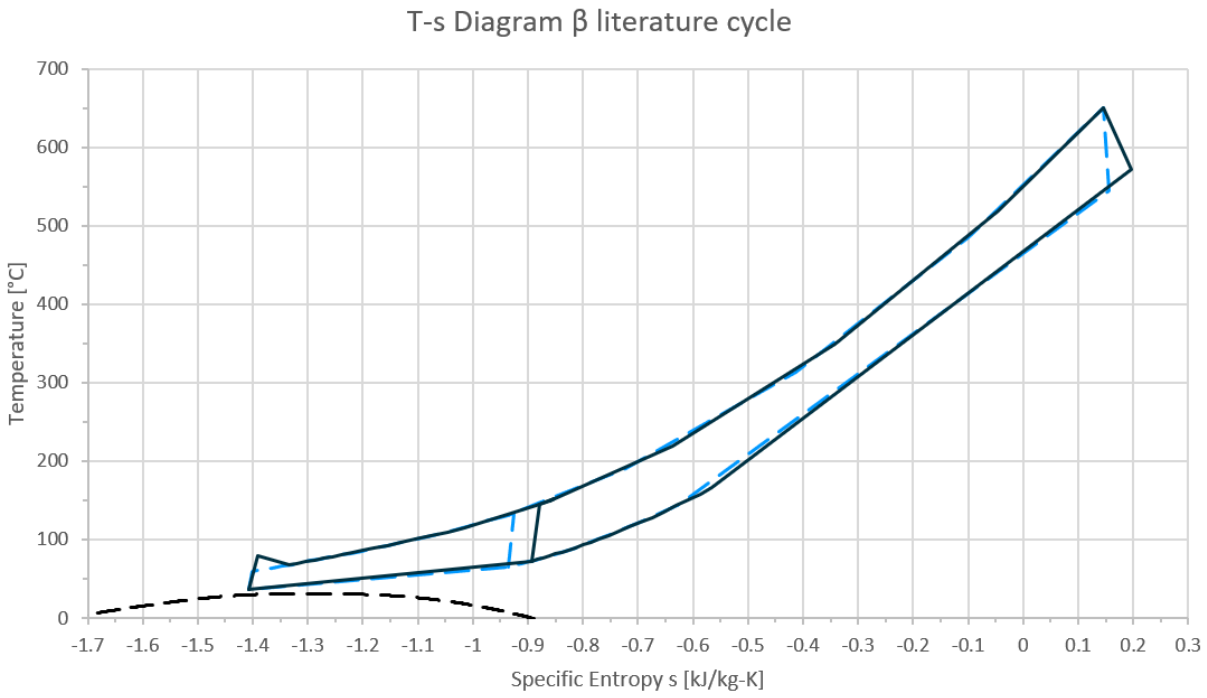

Figure 5.19: Literature cycle T-s diagram at β with CO_2 saturation bell

At the key point β, with an ambient temperature equal to the design ambient temperature, and a power output of 9 [MW] the literature cycle undergoes three important changes (T-s diagram wise). There is an appreciable reduction in the efficiency of the turbine, as can be seen by the slope of the expansion curve. The splitting of the flow takes place at a slightly higher temperature (which shifts it to the right along the specific entropy axis). Due to the reduced mass flow and the inability of the compressor to adjust its speed independent of turbine speed, the compressor's outlet pressure increases and the throttling valve then brings this pressure down resulting in the bump seen in Fig. 5.19.

The proposed cycle on the other hand sees three changes in it's T-s diagram. The first change is a decrease in temperature at the splitting point, shifting this line towards the left. The second change is the decrease in cycle high pressure as seen by the down-shifting of the top curve in the diagram. This is thanks to the control strategy implemented for the proposed cycle, which makes use of the three-shaft layout to modulate net power output with a decrease in cycle high pressure. Therefore unlike in the previous plot, there is no need for the throttling valves after either the compressors or the recompressors. This reduction in cycle high pressure in turn reduces the differential pressure through the turbine, reducing the enthalpy drop and thus the turbine's power output. The third and final change in the diagram is a decrease in temperature difference between streams in the HTR. As previously mentioned, the discretisation used for the HTR is enough to solve the cycle appropriately but not fine enough to visually analyse the heat transfer problem in the HTR.

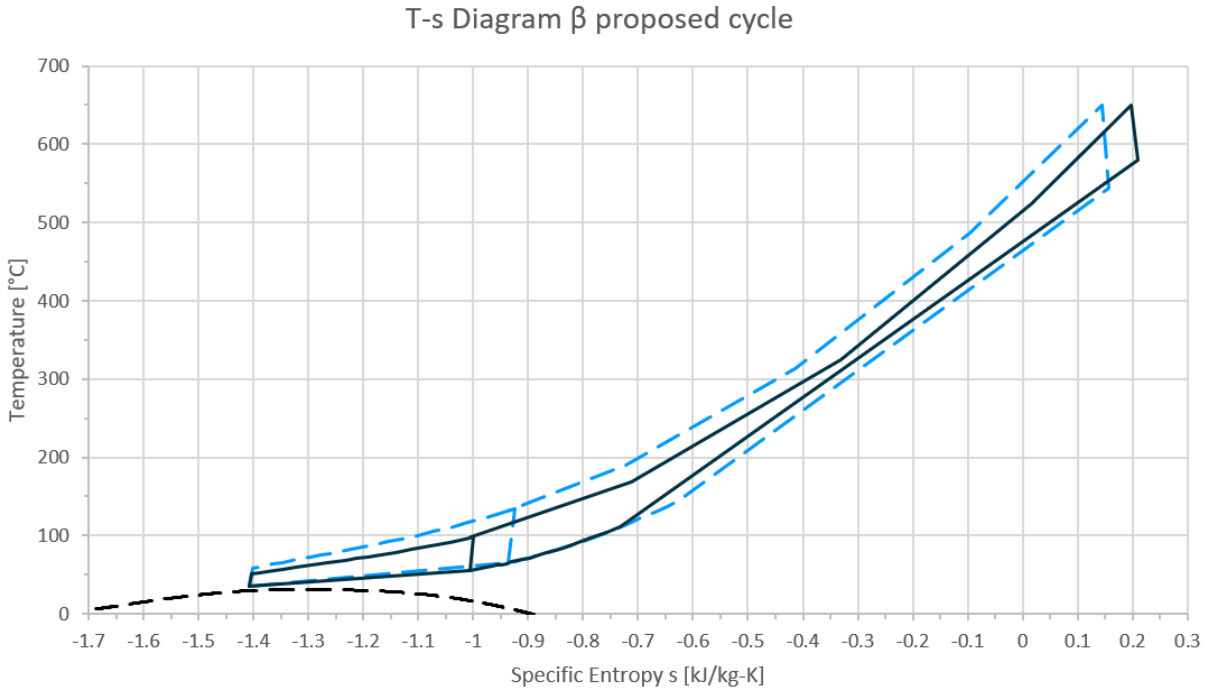

Figure 5.20: Proposed cycle T-s diagram at β with CO_2 saturation bell

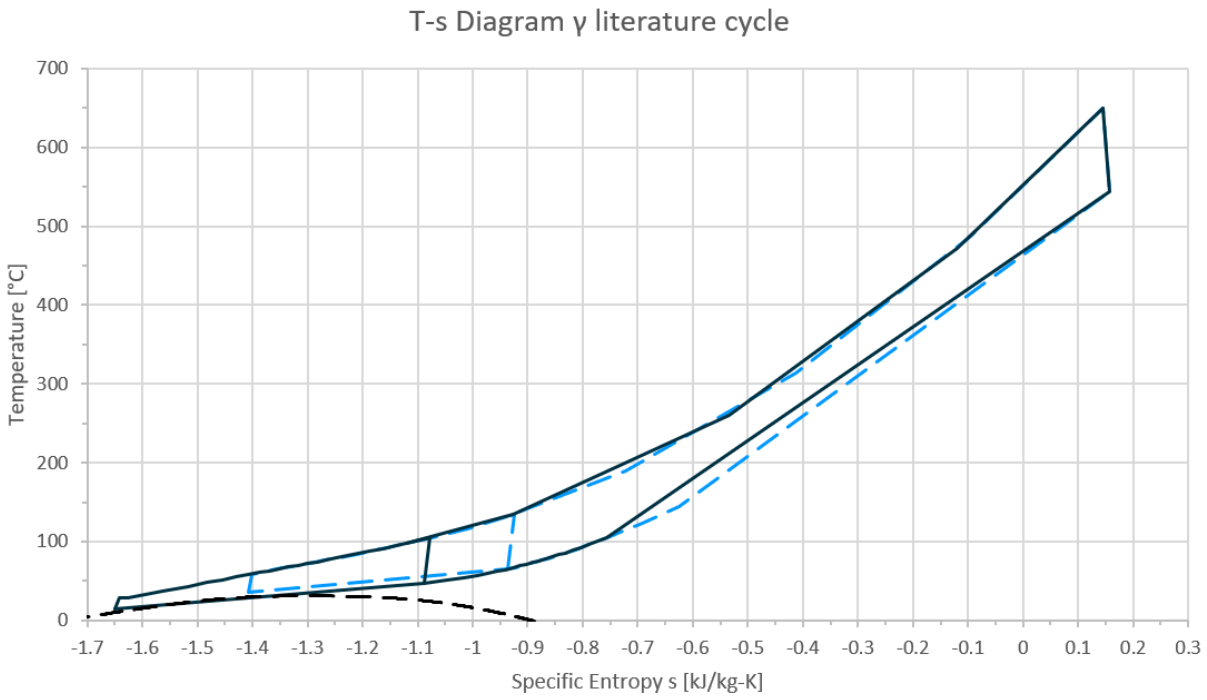

Figure 5.21: Literature cycle T-s diagram at γ with CO_2 saturation bell

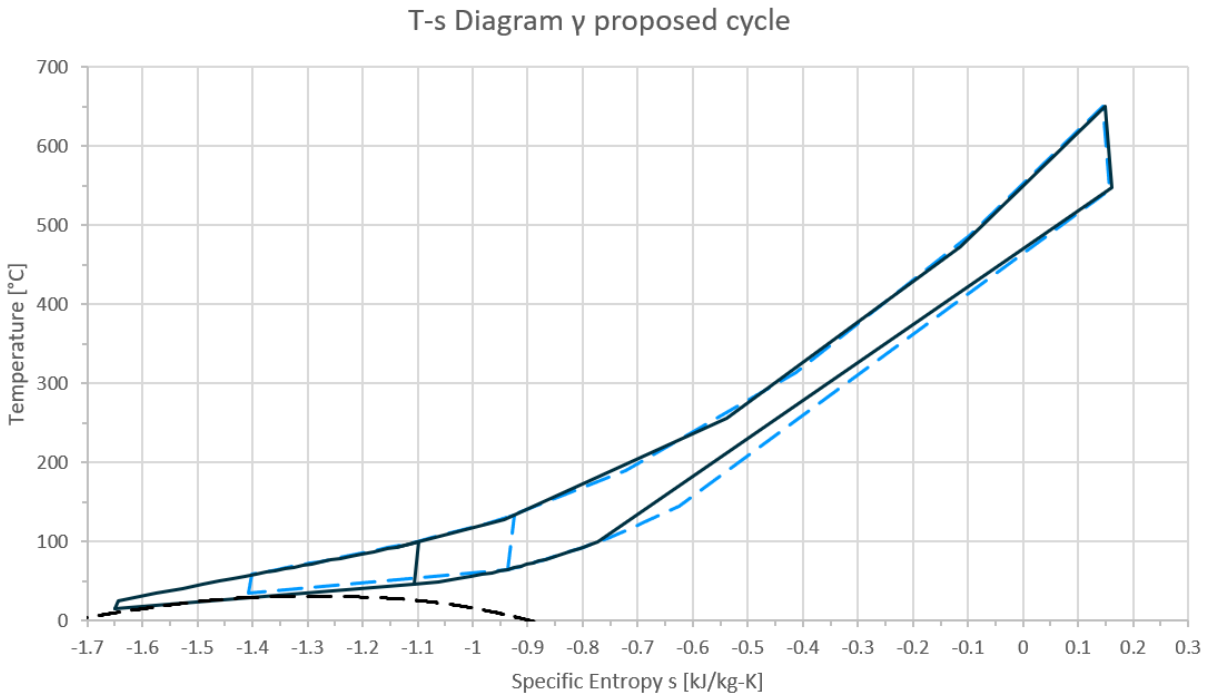

Figure 5.22: Proposed cycle T-s diagram at γ with CO_2 saturation bell

The γ key point evaluates the cycle at an ambient temperature of 0 [°C] and a power output of 25 [MW]. The literature cycle, shown in Fig. 5.21 undergoes three significant changes. As ambient temperature decreases, so does the temperature of the coolest point in the cycle, shifting the left end of the cycle to the left. This in turn shifts the splitting point towards the CO_2 critical point. No noticeable effect is seen on the T-s diagram of the latter point on the LTR heat transfer. The third change is analogous to what occurred in Fig. 5.19, with a very slight bump after the compressor signalling the action of the throttling valve.

The proposed cycle on the other hand sees two of the aforementioned three changes, with the exception being the valve bump after the compressor, thanks to the proposed cycle's ability to adjust the compressor speed independently from the turbine. The similarity between the T-s diagrams is in accordance with the similarity in first-law efficiencies, as both the literature and proposed cycle show efficiencies close to 46 % when operating at γ.

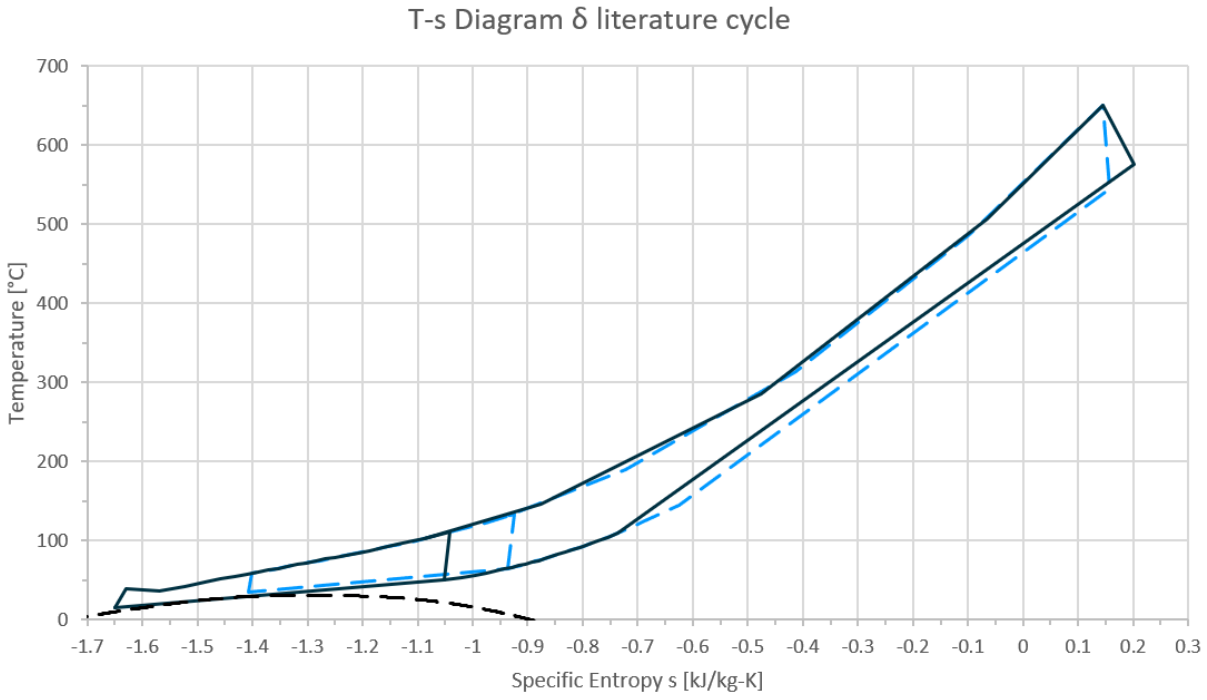

Figure 5.23: Literature cycle T-s diagram at δ with CO_2 saturation bell

At the key point δ the cycle operates at the same ambient temperature of 0 [°C] and at a power output of 9 [MW]. Fig. 5.23 showcase the four previously mentioned changes that happen to the literature's cycle T-s diagram. The cycle low temperature shifts downwards, so does the splitting temperature, there is a reduction in turbine efficiency and the throttling valve after the compressor is brought into action.

Similarly, in Fig. 5.24 cycle low temperature and splitting temperature decrease and like before, the cycle high pressure is reduced causing a decrease in enthalpy drop through the turbine. When inspecting the HTR section of the diagram, the decrease in stream temperature difference is so marked that it looks like the temperature difference becomes negative. This is, as was forewarned, due to the discretisation of the HTR not being fine enough to prevent the straight lines joining the data points from crossing each other. Further discretisation of the HTR is required in order to properly assess it's pinch point.

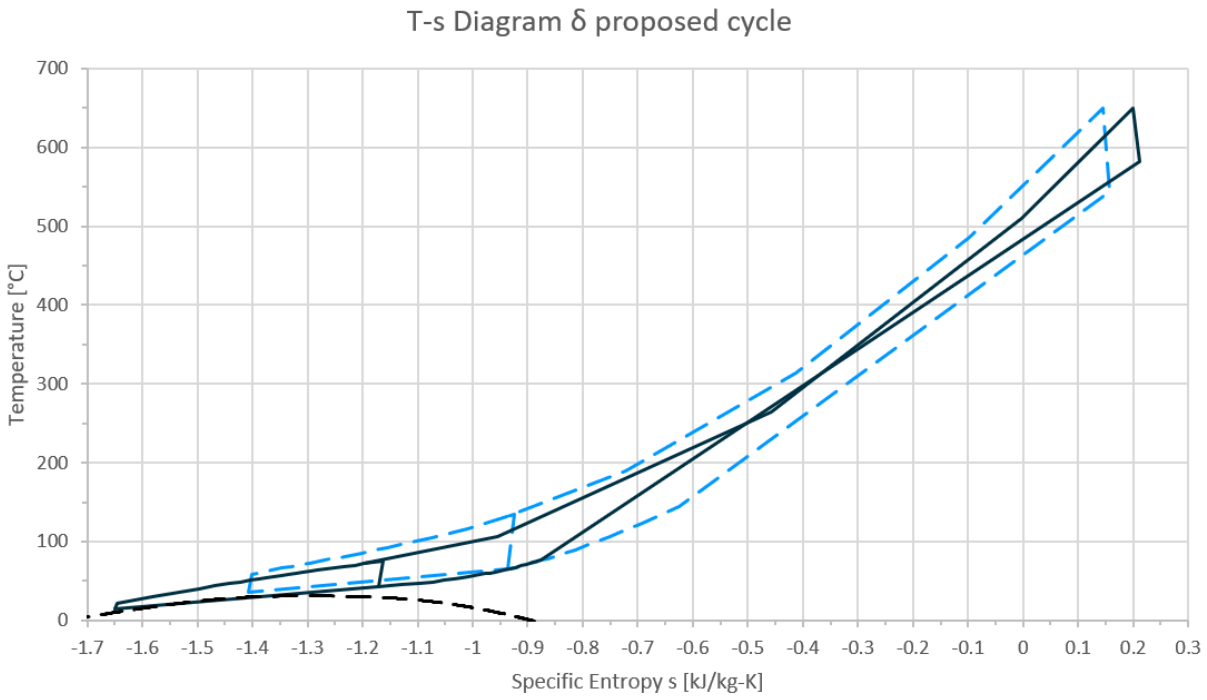

Figure 5.24: Proposed cycle T-s diagram at δ with CO_2 saturation bell

The following for T-s diagrams are the high ambient temperature limits of the operational ranges for both the literature and the proposed cycle. Key points ε and ϕ correspond to the proposed cycle's operation and λ and μ to the literature cycle's operation.

The ε key point corresponds to an ambient temperature of 28 [°C] and a power output of 14.8 [MW]. Three changes to the T-s diagram can be seen in Fig. 5.25, the first being the increase in cycle low temperature. This shifts the bottom part of the T-s diagram, as well as the splitting point towards the right. The compression of the work fluid takes place towards the right of the critical point, signalling the compression of a more gas-like and compressible supercritical fluid. The third change is a decrease in turbine efficiency, evidenced by the change in slope at the top-right part of the T-s diagram.

Figure 5.26 showcases the T-s diagram at key point ϕ, with ambient temperature at 28 [°C] and a power output at 9 [MW]. The differences between ε and ϕ are a further decrease in turbine efficiency and the curtailment of pressure at the compressor's outlet thanks to the throttling valve.

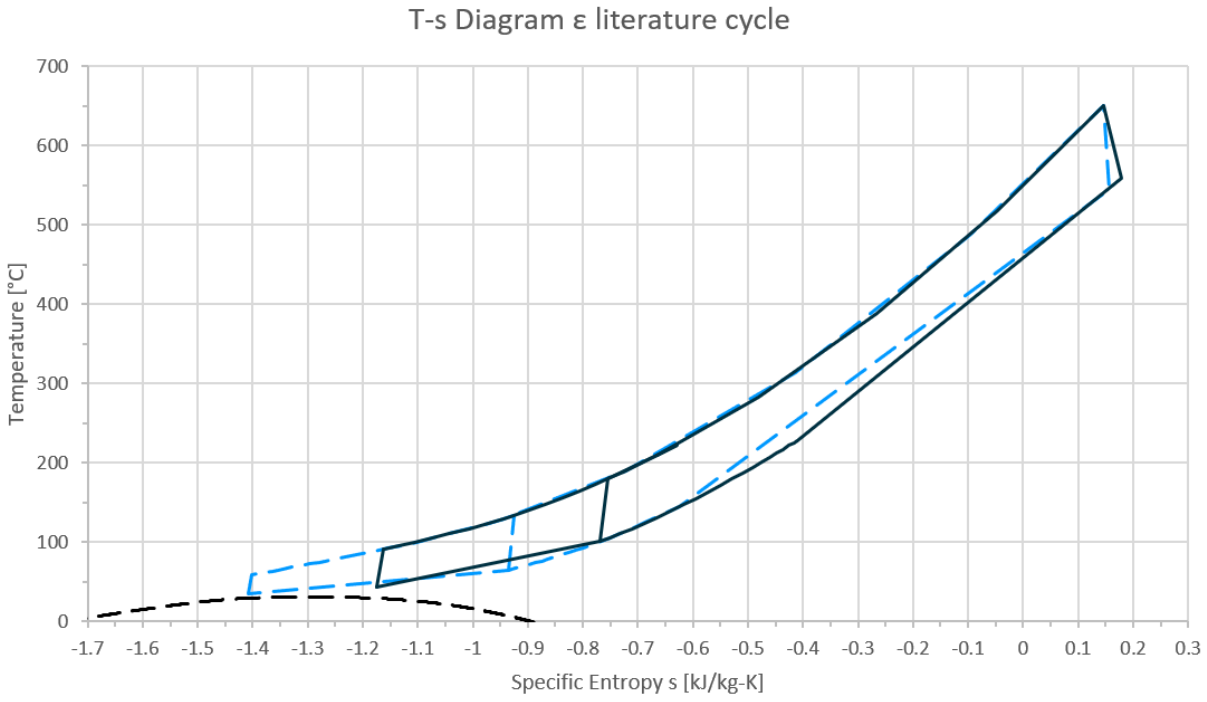

Figure 5.25: Literature cycle T-s diagram at ε with CO_2 saturation bell

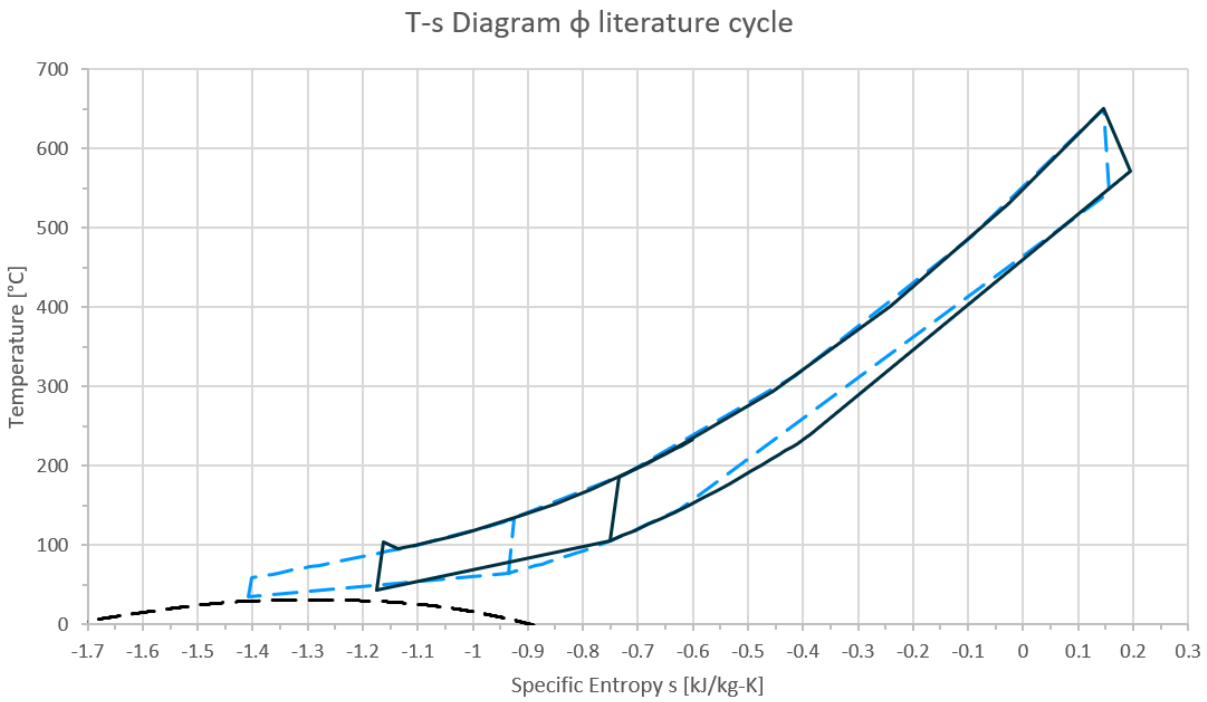

Figure 5.26: Literature cycle T-s diagram at ϕ with CO_2 saturation bell

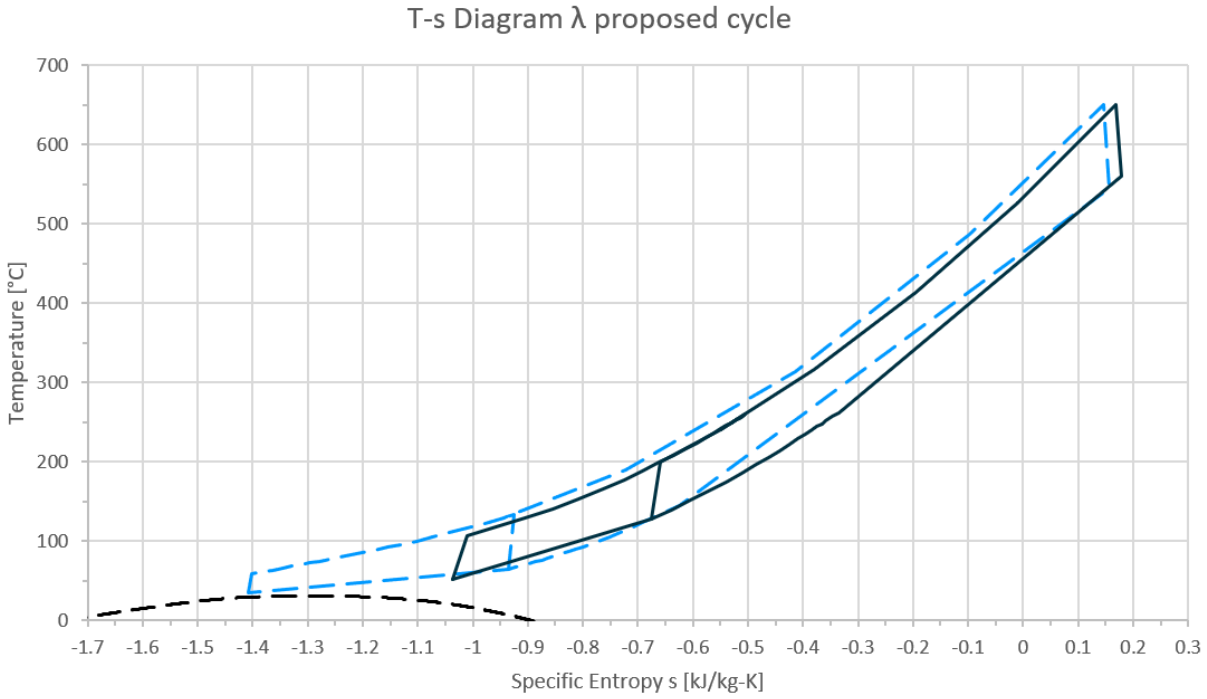

Figure 5.27: Proposed cycle T-s diagram at λ with CO_2 saturation bell

Both λ and μ, operating at 37 [°C] ambient temperature and 12.8 and 9 [MW] power outputs respectively experience the same three changes. The increase in ambient temperature shifts the bottom of the diagram and the splitting point towards the right. The third change is a reduction in cycle high pressure.

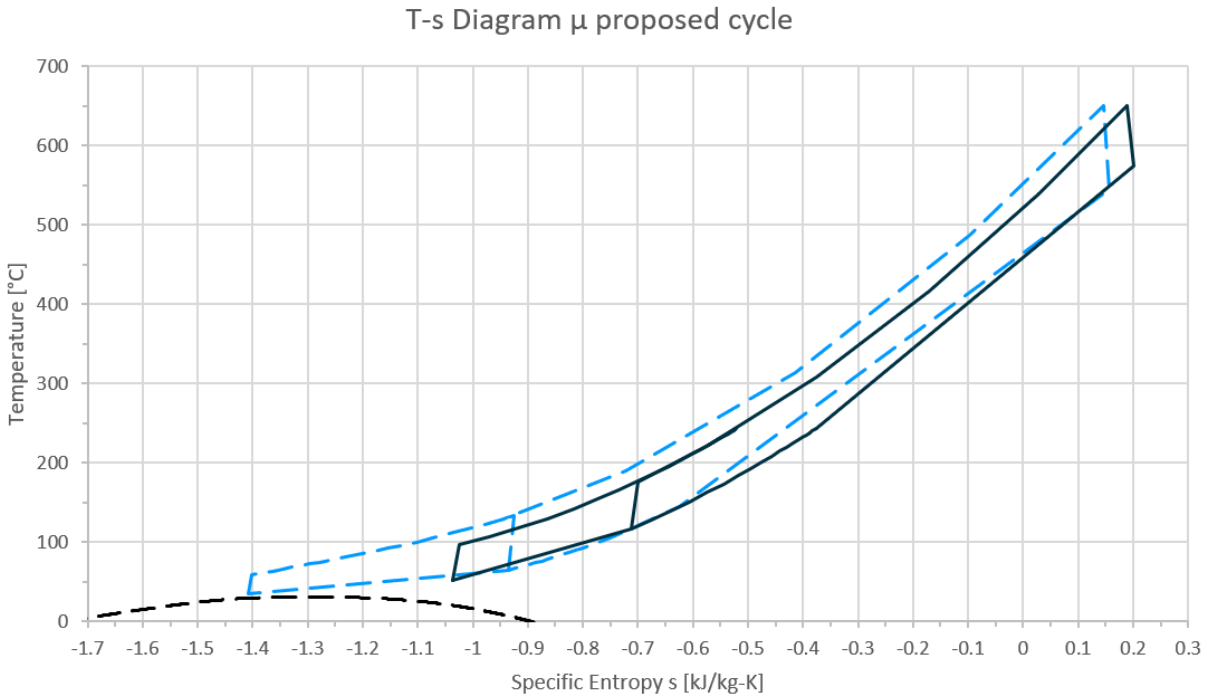

Figure 5.28: Proposed cycle T-s diagram at μ with CO_2 saturation bell

5.5.2 Exergy destruction

The destruction of physical exergy by component is carried out in order to quantify the magnitude of the irreversibilities generated during cycle off-design operation, providing insight into which mechanism is responsible for the decrease in cycle first-law efficiency.

Figure 5.29 showcases the destruction in physical exergy by cycle, component and key point. Figure 5.30 normalises the previous graph by the amount of net power generated, in order to better compare how the different scenarios differ. Figure 5.31 Presents the exergy destruction by component as a percentage of the total, providing further insight into the distribution of exergy destruction.

Total exergy destructed varies little with respect to net power output for the literature cycle, never dropping below 8500 [kW] whilst for the proposed cycle it goes as low as approximately 5000 [kW] for the β key point, as seen in Fig. 5.29. Total exergy destructed is always lower for the proposed cycle than for the literature cycle. Whilst exergy destructed increases with a decrease in net power output for the literature cycle ($\alpha \rightarrow \beta$, $\gamma \rightarrow \delta$ and $\varepsilon \rightarrow \phi$) the opposite is true for the proposed cycle ($\alpha \rightarrow \beta$, $\gamma \rightarrow \delta$ and $\lambda \rightarrow \mu$).

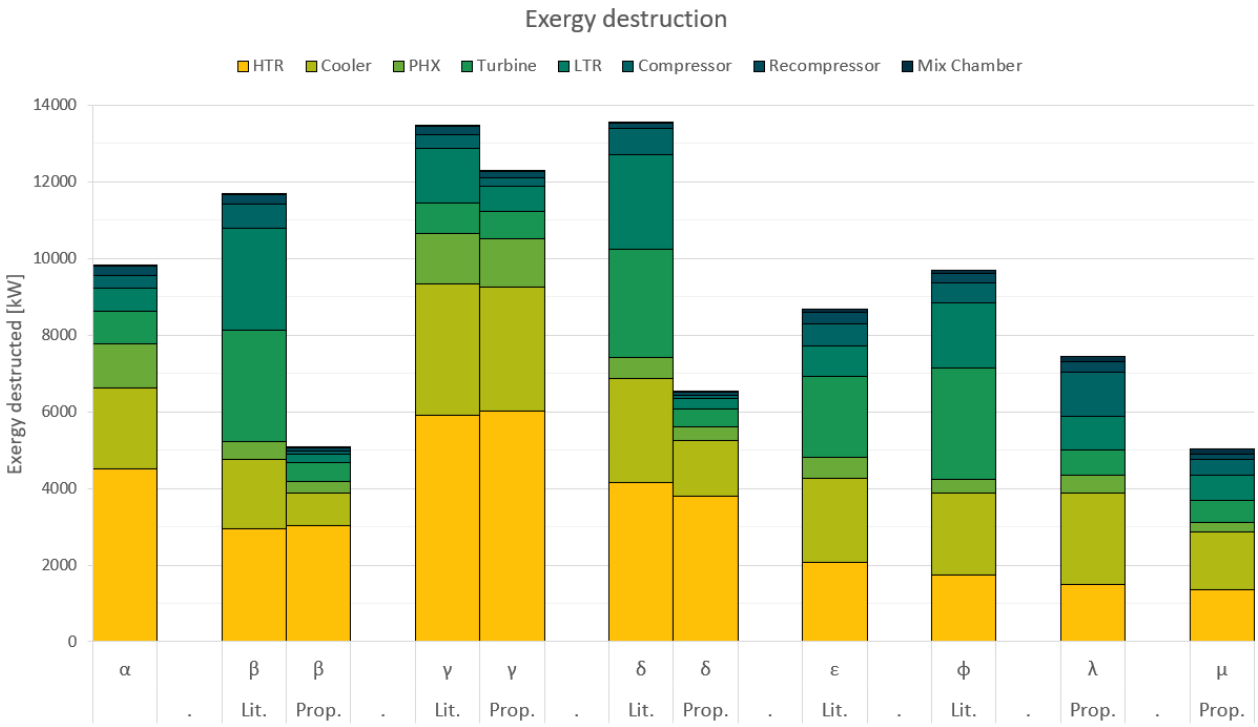

Figure 5.29: Exergy destruction

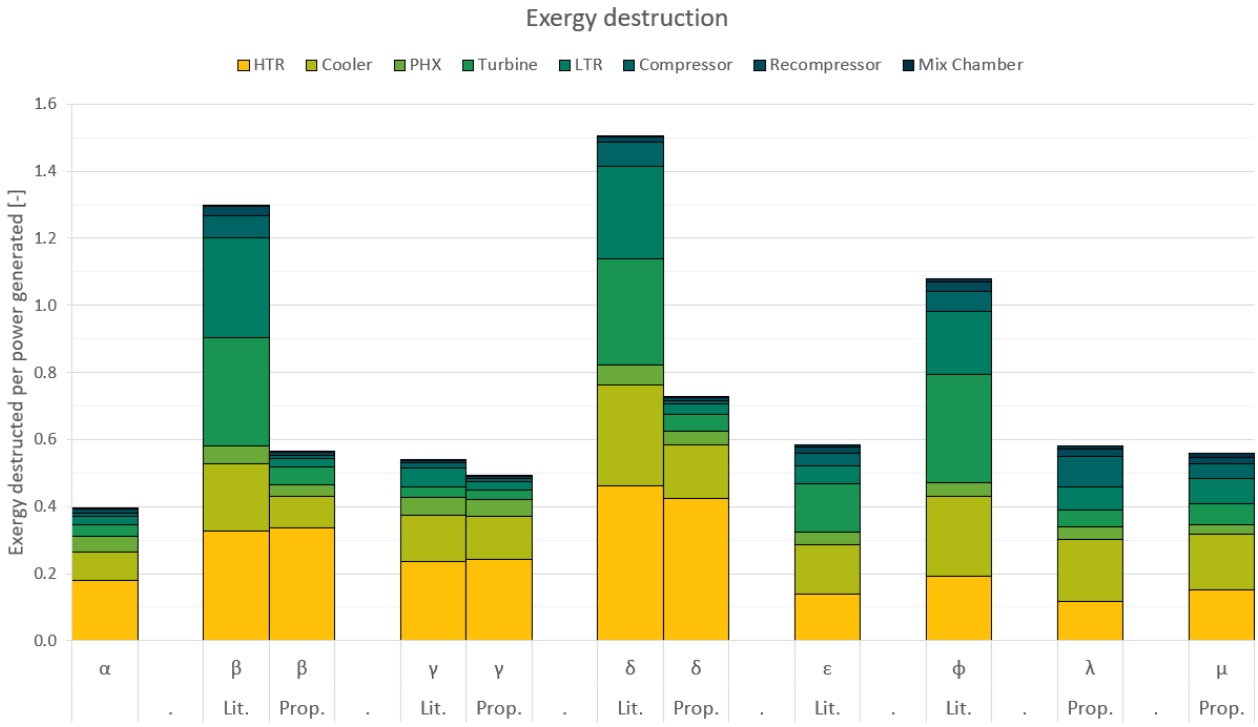

Figure 5.30: Exergy destruction per unit power generated

On a per unit power generate basis, α destroys the least amount of exergy. This makes sense as α corresponds to the design condition. α is followed by the proposed cycle and then the literature cycle with the scenarios where the literature cycle operates outputting 9 [MW] yielding the worst results.

The HTR is the component where most exergy is destructed under nominal operation. This holds true for most scenarios, with the exception of the turbine in ε and ϕ and the cooler at λ and μ. For the proposed cycle, the mix chamber makes a noticeable contribution, percentage-wise. This is more due to the total exergy destruction being smaller, than the mix chamber being an important source of irreversibilities. This can be corroborated by checking Figures 5.29 and 5.30.

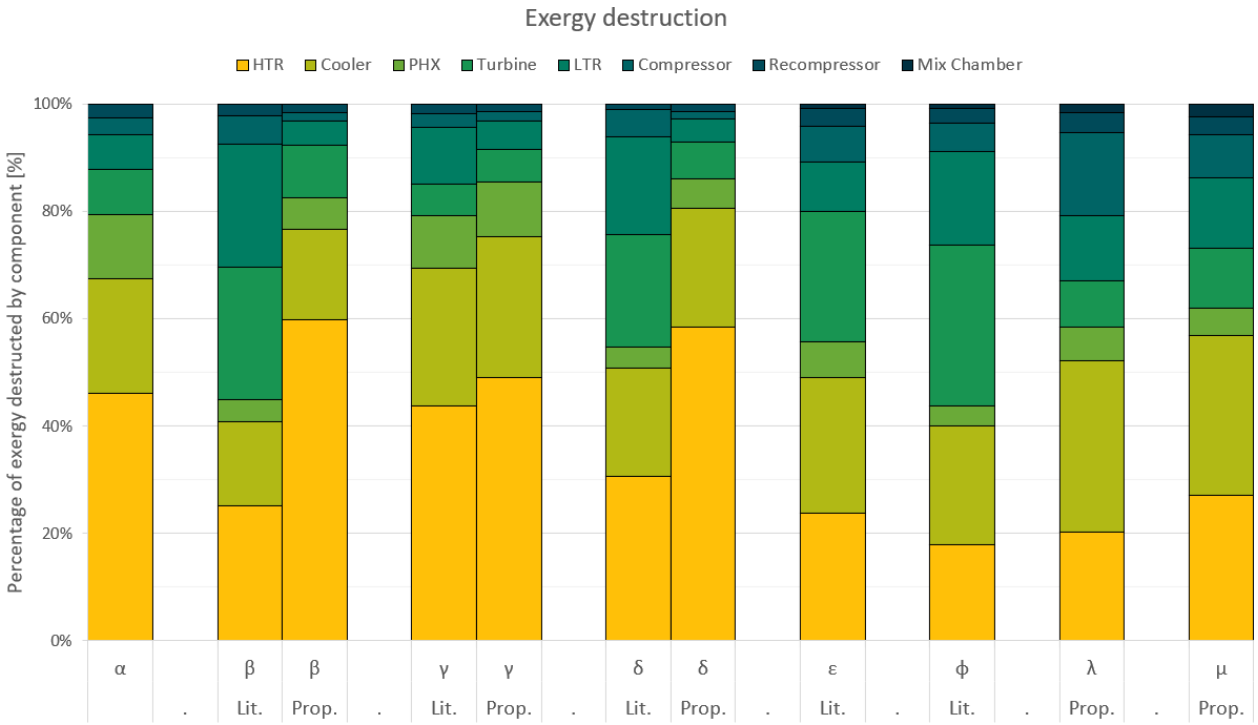

Figure 5.31: Percentage exergy destruction by component

5.6 Yearly simulation

Table 5.5: Yearly simulation summary

Metric	Literature	Proposed
Availability [%]	76.45	93.45
η_{season}[%]	29	39
$\eta_{ex,season}$[%]	48	65
% Time 3 out of 3	0.76	36.24
% Time 2 out of 3	49.93	57.20
% Time 1 out of 3	25.75	0.00
% Time unavailable	23.55	6.55

The results in Table 5.5 summarise the results of the yearly simulation for both cycles. It shows how the proposed cycle outshines the literature cycle when dispatch curves and shifting cycle low temperatures are considered. The proposed cycle has a very high availability, an availability of 93.45 % is a solid result when considering renewables. Nevertheless it must be stated that the solar multiple of 4 and 12 hours of storage considered is far from economically feasible.

The seasonal efficiencies describe how two cycles with the same design efficiency of 48.3 % can vary their effective efficiencies during a TMY substantially. Going from a 48.3% to 39% cycle first-law efficiency is not desirable, yet it is close to half the drop in efficiency experimented by the literature cycle. The literature cycle's first law efficiency decreased from 48.3% under nominal operation to 29% seasonal.

Regarding the exergetic seasonal efficiency: as the exergetic analysis was carried out from the molten salts perspective, all the irreversibilities present in the solar field are not being taken into consideration. This contributes to explain why these efficiencies where so high.

Chapter 6

Conclusions

The Petukhov's correlation, as well as other correlations proposed in the literature underestimate pressure drop through the SNL test loop. This is probably due to the experimental nature of the test loop. When the model is adjusted for the aforementioned error in pressure drop it describes the power cycle under nominal conditions accurately. Gnielinksi's correlation allows for an accurate description of the heat transfer problem in the s-CO_2 RCBC at cycle low pressures of 90 [bar].

The two-shafts configuration is not able to achieve the required flexibility when considering the off-design operation of the literature cycle, subject to the Crucero meteorological data and the dispatch curves. The operational range of the literature is highly limited. A novel phenomena denominated shaft-blockage reduces the operational range of the literature cycle. An M out of N system greatly extends the operational range of both the literature and proposed cycle by delaying the onset of surge in the compressors. Further work is required in order to extend the operational range of the cycle to higher ambient temperatures whilst generating the design net power output.

The shortcomings of the literature cycle's performance are reflected in the 20 point decrease between nominal and seasonal first-law efficiency. The three-shaft system of the proposed cycle is flexible and this can be appreciated through both the greater operational range as well as the greater seasonal first-law efficiency, which is 10 points greater than the literature one. The synergistic effects of decreasing cycle high pressure alongside with mass flow as a turn-down strategy is demonstrated and quantified. Like the literature cycle, the proposed cycle's operational range is also delimited by phenomena like surge and supersonic flow regimes.

The exergetic analysis finds the HTR component to be the greatest source of irreversibilities under design conditions. This evidences an improper HTR and LTR sizing. Further work is recommended on: the description of the Cooler and PHX at off-design conditions, the techno-economical feasibility of an M out of N system for s-CO_2 RCBC and the design and optimisation of a s-CO_2 RCBC with dispatch curves designed primarily to complement PV.

Bibliography

[1] CNE, "Installed capacity." http://energiaabierta.cl/visualizaciones/installed-capacity/?lang=en, 2019.

[2] London Metal Exchange, "Lithium at the LME." https://www.lme.com/Metals/Minor-metals/Lithium#tabIndex=0, 2019.

[3] Metalary, "Lithium price." https://www.metalary.com/lithium-price/, 2019.

[4] London Metal Exchange, "Copper." https://www.lme.com/Metals/Non-ferrous/Copper#tabIndex=0, 2019.

[5] Center for sustainable energy, "California primed to benefit from combining solar with energy storage." https://energycenter.org/thought-leadership/blog/california-primed-benefit-combining-solar-energy-storage.

[6] M. Mehos, C. Turchi, J. Vidal, M. Wagner, Z. Ma, C. Ho, W. Kolb, C. Andraka, Z. Ma, A. Kruizenga, and NREL, "Concentrating Solar Power Gen3 Demonstration Roadmap," *Nrel/Tp-5500-67464*, no. January, pp. 1–140, 2017.

[7] T. Wang, "Global benchmark capex for utility-scale solar PV 2010-2018." https://www.statista.com/statistics/971982/solar-pv-capex-worldwide-utility-scale/, 2019.

[8] T. Wang, "Global CSP installed cost 2010-2018." https://www.statista.com/statistics/799359/global-concentrated-solar-power-installation-cost-per-kilowatt/, 2019.

[9] REN21, *Renewables 2017 Global Status Report*. 2017.

[10] CSPplaza, "China to lead global CSP market by 2030." http://en.cspplaza.com/china-to-lead-global-concentrated-solar-power-market-by-2030, 2019.

[11] G. Angelino, "Carbon Dioxide Condensation Cycles For Power Production," 1968.

[12] Solargis, "Solar resource maps of World." https://solargis.com/maps-and-gis-data/download/world.

[13] E. M. Clementoni, T. Held, J. Pasch, and J. Moore, *Test facilities*. Elsevier Ltd, 2017.

[14] T. Feral and M. Saldaña, "Supercritical carbon dioxide technology for food and natural health products." http://canadianfoodbusiness.com/2014/12/17/supercritical-carbon-dioxide-technology/.

[15] NIST, "NIST web book." https://webbook.nist.gov/.

[16] J. Dyreby, "Modeling the Supercritical Carbon Dioxide Brayton Cycle with Recompression," pp. 1–165, 2014.

[17] G. E. Rochau, J. Pasch, G. Cannon, M. Carlson, D. Fleming, A. Kruizenga, R. Sharpe, and M. Wilson, "Supercritical CO2 Brayton Cycles," 2014.

[18] J. J. Pasch, T. M. Conboy, D. D. Fleming, and G. E. Rochau, "Supercritical CO2 recompression Brayton cycle : completed assembly description.," Tech. Rep. October, 2012.

[19] L. Irwin and Y. Le Moullec, "Turbines can use CO2 to cut CO2," vol. 356, no. 6340, 2017.

[20] F. Correa, "Modelación y optimización de ciclo Brayton de recompresión con dióxido de carbono supercrítico bajo condiciones variables," no. 1, pp. i–3, 2019.

[21] W. Seidel, "Model development and annual simulation of the supercritical carbon dioxide Brayton cycle for concentrating solar power applications," vol. Thesis, 2010.

[22] Heatric, "What is a Heatric Printed Circuit Heat Exchanger?." https://www.heatric.com/heat-exchangers/.

[23] B. Epp, "Molten salt storage 33 times cheaper than lithium-ion batteries," 2018.

[24] Inhabitat, "Commercializing Solar Power with Molten Salt," 2008.

[25] G. Mohan, M. Venkataraman, J. Gomez-Vidal, and J. Coventry, "Assessment of a novel ternary eutectic chloride salt for next generation high-temperature sensible heat storage," *Energy Conversion and Management*, vol. 167, no. April, pp. 156–164, 2018.

[26] A. Bejan, G. Tsatsaronis, and M. Moran, "Thermal Design and Optimization," 1995.

[27] Carstens and Nathan, "Control strategies for supercritical carbon dioxide power conversion systems," *Massachusetts Institute of Technology*, 2007.

[28] V. Gnielinski, "Neue Gleichungen für den Wärme- und den Stoffübergang in turbulent durchströmten Rohren und Kanälen," *Forschung im Ingenieurwesen*, vol. 41, no. 1, pp. 8–16, 1975.

[29] B. S. Petukhov, "Heat Transfer and Friction in Turbulent Pipe Flow with Variable Physical Properties," *Advances in Heat Transfer*, vol. 6, no. C, pp. 503–564, 1970.

[30] R. Fuller and K. Eisemann, "Supercritical CO2 Power Cycle Symposium Centrifugal Compressor Off-Design Performance for Super-Critical CO2," 2011.

[31] I. Jahn and J. Keep, "On the off-design performance of supercritical carbon dioxide power cycles," pp. 1–10, 2017.

[32] S. Wright and R. Radel, "Operation and analysis of a supercritical co2 brayton cycle," *Linguistics and Education*, vol. 37, no. September, pp. 63–72, 2017.

[33] A. Glassman, "Miscellaneous Losses," *Turbine Design and Application*, p. 390, 1972.

[34] B. G. F. Hiett, "Experiments concerning the aerodynamic performance of inward flow radial turbines," vol. 178, no. ii, pp. 28–42.

[35] Stodola, "Modelling of off-design multistage turbine pressures by stodola's ellipse."

[36] A. Kruizenga, M. Anderson, R. Fatima, M. Corradini, A. Towne, and D. Ranjan, "Heat transfer of supercritical carbon dioxide in printed circuit heat exchanger geometries," *2010 14th International Heat Transfer Conference, IHTC 14*, vol. 4, no. September, pp. 653–661, 2010.

[37] Y. Jiang, E. Liese, S. E. Zitney, and D. Bhattacharyya, "Design and dynamic modeling of printed circuit heat exchangers for supercritical carbon dioxide Brayton power cycles," *Applied Energy*, vol. 231, no. September, pp. 1019–1032, 2018.

[38] Blasius H., "Das Aehnlichkeitsgesetz bei Reibungsvorgängen in Flüssigkeiten," *Mitteilungen über Forschungsarbeiten auf dem Gebiete des Ingenieurwesens*, vol. 131, pp. 1–41, 1913.

[39] Wikipedia, "Logarithmic Mean." https://en.wikipedia.org/wiki/Logarithmic_mean.

[40] C. Bravo, "Optimización de parámetros de diseño de una planta solar de concentración para generación eléctrica considerando distintos escenarios de despacho," 2018.

[41] S. K. Mylavarapu, X. Sun, R. N. Christensen, R. R. Unocic, R. E. Glosup, and M. W. Patterson, "Fabrication and design aspects of high-temperature compact diffusion bonded heat exchangers," *Nuclear Engineering and Design*, vol. 249, pp. 49–56, 2012.

[42] S. Beck and R. Collins, "Moody Diagram," 2008.